UNIVERSITY OF LATVIA

INVESTIGATION OF ELECTROMAGNETICALLY DRIVEN FLOWS FOR DEGASSING PROCESS OPTIMIZATION IN LIQUID METAL

Reinis Baranovskis

Advisor: Dr. phys. Ilmārs Grants

Submitted for the degree of Doctor of Physics
Subfield of Mechanics of Fluids and Gases

Riga 2022

ABSTRACT

This thesis's motivation is improving one of aluminum's manufacturing steps - degassing. The excess dissolved gasses, such as hydrogen, are removed from molten aluminum during this stage. Currently, the most common way is to inject inert gas into the melt, and the gas absorbs dissolved hydrogen and leaves the metal through its free surface via bubbling. Existing methods need mechanical contact with the hot and chemically aggressive aluminum, leading to higher maintenance costs and heat losses. Here a novel contactless degassing method is researched. It uses electromagnetic forces to drive the flow, which disperses the injected inert gas bubbles. In this work, bubble dispersion by turbulent flow is studied experimentally in GaInSn and aluminum models. Bubble size reduction has been directly observed in liquid metal (GaInSn) and correlated with flow conditions. Velocity and pressure measurements are used to characterize fluid dynamics taking place in liquid metal. Power measurements describe electromagnetic performance and limitations of permanent magnet machines. These experimental results are further used to validate numerical MHD models developed parallel to this work. An experimentally validated numerical model calculates turbulence characteristics which can be used to express bubble size according to an empirical relation for bubble size in isotropic turbulence. Based on it, a method for predicting bubble refinement is proposed. This approach predicts bubble size in a proposed industrial aluminum prototype. Results show that refining bubbles in liquid metal with the electromagnetically created flow is possible. The impact in the aluminum industry covers 2500 aluminum smelting plants holding around 25 000 degassing units.

Keywords: Aluminum degassing, bubble collapse, dissolved hydrogen, metal stirring

ANOTĀCIJA

Doktora darba pētījuma motivācija ir nepieciešamība uzlabot vienu no alumīnija ražošanas posmiem: degazāciju. Degazācija ir alumīnijā izšķīdušo gāzu koncentrācijas samazināšana, kas galvenokārt nozīmē atbrīvošanos no šķidrajā alumīnijā izšķīdušā ūdeņraža. Industrijā visizplatītākais degazācijas risinājums ir inertas gāzes ievadīšana izkausētā alumīnijā, ar kuras palīdzību tiek piesaistīts izšķīdušais ūdeņradis, un tas kopā ar gāzes burbuļiem tiek izvadīts prom no metāla caur tā brīvo virsmu. Procesa efektivitātes uzlabošanai industrijā veic burbuļu sašķelšanu - visbiežāk mehāniski, ar alumīnijā iemērktu rotoru. Lai izvairītos no siltuma zudumiem un strauja detaļu nolietojuma, ko rada tiešais kontakts ar karsto un agresīvo vidi, darbā tiek pētīta jauna bezkontakta metode alumīnija degazēšanai, kurā turbulento plūsmu burbuļu sašķelšanai rada elektromagnētiskie spēki. Šķidrajā metālā inducētā plūsmā tiek pētīta eksperimentāli, izmantojot GaInSn sakausējuma un alumīnija modeļus. Pirmo reizi ir tiešā veidā veikti burbuļu izmēra mērījumi šķidrā metālā (GaInSn) un noskaidrota to diametra korelācija ar plūsmas raksturlielumiem. Veiktie ātruma un spiediena mērījumi raksturo radītās plūsmas dinamiku šķidrā metāla tilpumā. Jaudas mērījumi raksturo elektromagnētiskās mijiedarbības efektivitāti un ierobežojumus plūsmas intensitātei, ko spēj radīt rotējošie pastāvīgie magnēti. Iegūtie eksperimentālie rezultāti papildus tiek izmantoti, lai validētu skaitliskos modeļus, kas ir izstrādāti paralēli šim darbam. Izmantojot eksperimentāli pārbaudītus skaitliskos modeļus ir iespējams aprēķināt turbulences raksturlielumus šķidrā metāla plūsmā. Šajā darbā tiek aprakstīta metode, kurā skaitlisko modeļu rezultāti tiek izmantoti analītiskiem aprēķiniem, ar kuriem var paredzēt burbuļa izmērus izotropiskā turbulentā plūsmā. Balstoties uz šo metodi, tiek paredzēts sagaidāmo burbuļu izmērs alumīnija degazācijas prototipa iekārtā. Uzlabojot metalurgiem tik "ikdienišķu" ražošanas posmu, ietekme būtu mērāma vairāk nekā 2500 alumīnija pārkausēšanas rūpnīcās visā pasaulē, kurās kopsummā ir ap 25 000 degazēšanas iekārtu, potenciāli samazinot patērētās inertās gāzes daudzumu, patērēto enerģiju un negatīvo ietekmi uz vidi kopumā.

Atslēgvārdi: alumīnija degazācija, burbuļu sagraušana, izšķīdis ūdeņradis, metāla maisīšana,

SYMBOLS AND ABBREVIATIONS

Symbool	Unit	Descirption
MHD	-	Magnetohydrodynamics
EM	-	Electromagnetic
UDV	-	Ultrasound Doppler Velocimetry
AC	-	Alternating current
TKE	-	Turbulence kinetic energy
Re	-	Reynolds number
Re_m	-	Magnetic Reynolds number
Ha	-	Hartmann number
N	-	Stuart number
Pe	-	Péclet number
Ω_D	-	Dimensionless frequency
We	-	Weber number
Eo	-	Eötvös number
Mo	-	Morton number
Fr	-	Froude number
t	s	Time
f	Hz	Frequency
ω	rad/s	Angular frequency
η	$Pa \cdot s$	Dynamic viscosity
ν	m^2/s	Kinematic viscosity
ρ	kg/m^3	Density
p	Pa	Pressure
$\mathbf{g}$	m^2/s	Gravitational acceleration
$\mathbf{f}$	N/m^3	Force density
$\mathbf{u}$	m/s	Flow velocity
$\mathbf{E}$	V/m	Electric field intensity
$\mathbf{B}$	T	Magnetic field induction
$\mathbf{J}$	A/m^2	Current density
$\mathbf{A}$	$V \cdot s/m$	Magnetic vector potential
P	W	Power
P_H	W	Hydraulic power
ρ_q	C/m^3	Charge density
ρ_e	C/m^3	Total charge density (free + bounded charges)
τ_e	s	Charge relaxation time

Symbool	Unit	Descirption
m	kg	Mass
l	m	Characteristic length
r	m	Radius
σ	S/m	Electric conductivity
δ	m	Skin depth
Φ	V	Scalar electrostatic potential
μ_0	H/m	Permeability of free space
ϵ_0	F/m	Permittivity of free space
ε	m^2/s^3 or W/kg	TKE dissipation rate
K	$-$	Equilibrium constant
c_{H_2}	$cm^3/100g$	Hydrogen solubility
c_p	$J/kg \cdot K$	Specific heat capacity
γ	N/m	Surface tensions
λ_c	m	Capillary length
τ_m	s	Characteristic mixing time

Contents

List of Tables

List of Figures

1. INTRODUCTION

1.1. Motivation

Although aluminum is the world's second most used metal, some of its manufacturing steps have not been improved for decades. My thesis focuses on improving one of aluminum's manufacturing steps called ”degassing”. In a metallurgical environment, molten metal contains dissolved gases that cause mechanical defects like porosity that lead to worse mechanical properties [1]. To solve that, the concentration of dissolved gases must be reduced below a critical level before the molten metal is crystallized. The most common way is to inject inert gas in the melt, which absorbs dissolved hydrogen and leaves the metal through its free surface. Existing methods [13] need mechanical contact with the metal to disperse the gas into smaller bubbles and accelerate the degassing process. The contact with the hot and chemically aggressive aluminum leads to higher maintenance costs.

In my thesis, I propose to investigate a new contactless degassing method that uses an electromagnetic stirring system to create a suitable flow for the degassing process. The challenging task here is to ensure a high enough velocity difference between the gas inlet and flow while maintaining a flow type with minimal surface deformation. Solving these challenges requires extensive numerical and experimental modeling, which I aim to combine in this work. By improving such a vital step of aluminum manufacturing, the scope of impact would cover 2500 aluminum smelting plants holding around 25 000 degassing units, thus potentially seeing improvements in energy consumption, reduction in inert gas consumption, and an overall increase in efficiency.

1.2. Aluminum production and degassing

Aluminum production begins with extracting bauxite from the ground. From there, bauxite is refined to extract alumina (Al_2O_3) by the Bayer process. Alumina then goes through an energy-intensive electrolysis process in Hall–Héroult cells, where primary aluminum is produced.

Aluminum in pure form is seldom used; instead, aluminum alloys make aluminum products all around us. Any specific alloy is made in a casthouse where numerous substeps can be distinguished, including degassing. Aluminum is melted in a melting furnace by electric heating or, most commonly, by gas burners. The latter case is a significant source of hydrogen pollution because water vapor is one of the combustion products (how water pollutes aluminum is discussed in subsection 4.2.5). After the melting, the aluminum is transferred to a holding furnace where it is settled, and alloying elements are added, creating the desired alloy. Lastly, aluminum is transferred to a casting line where aluminum is firstly degassed. This is the step which our proposed technology would improve. After the degassing, the aluminum is filtered (last line of defense) just before it is cast by one of many processes (continuous rod or sheet casting, foundry ingot casting, billet, and slab casting). After the casting step, thermal processing is applied depending on the aluminum product. If aluminum is recycled (about 1/3 is), the steps of mining bauxite and alumina reduction are skipped, but the processes described in the casthouse remain. This means the degassing process is necessary regardless of the aluminum production process.

In industrial processes, aluminum inevitably dissolves hydrogen from water vapor in the environment. Adverse effects of dissolved hydrogen in various alloys are fundamentally explained in these papers [1, 14]. Aluminum collects hydrogen from water vapor and air in storage and processing. Naturally, the process is drastically faster when aluminum is molten and its surface is agitated. Thus the most critical phase where the melt can be contaminated by hydrogen is the melting of aluminum by gas, where one of the combustion products is water.

Hydrogen content is measured in rather odd units of $\frac{\mathrm{cm}^3}{100\ \mathrm{g}}$. Above all, the dissolved hydrogen causes porosity even in trace amounts, leading to worse mechanical properties as shown in figures 1.1. The threshold where dissolved hydrogen causes significant porosity depends on the alloy and which manufacturing technique is being used. It is in range of 0.1 to 0.4 $\frac{\mathrm{cm}^3}{100\ \mathrm{g}}$ (see Fig. 1.1a). Converted to mass fraction values, the thresholds are tiny, and in the range of $8.5 \cdot 10^{-5}$ to $3.5 \cdot 10^{-4}$, however, the porosity depends on volume fraction, which is in order of 10^{-2}. Graph in 1.1b clearly illustrates that porosity in order of 1 % dramatically decreases tensile strength.

Therefore, a reduction of hydrogen content (or simply degassing) is a necessary step before manufacturing the final aluminum product. There are multiple degassing methods, the four most common are listed down below and explained in detail in subsection 3.1:

1. Gas purging with a rotary gas injector [13] where a rotating impeller achieves gas injection and stirring.

2. Ultrasound degassing which uses mechanical waves that create pressure oscillations in metal.

3. Vacuum degassing where pressure on the free surface is reduced to accelerate gas removal.

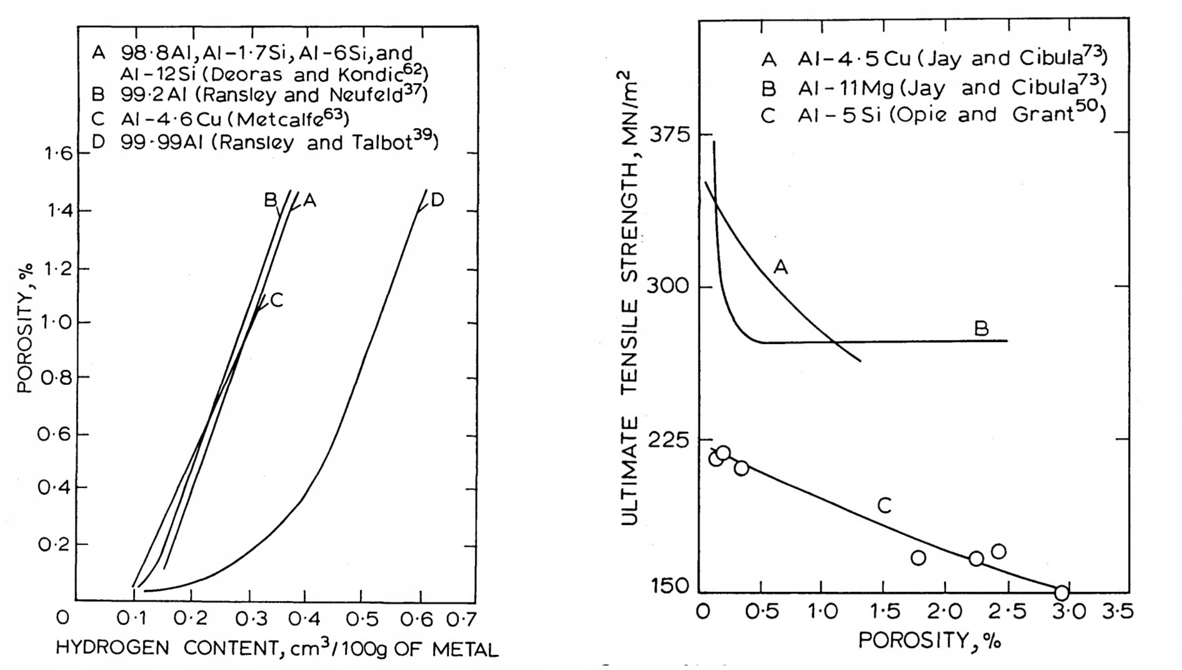

(a) **Porosity vs. hydrogen**

(b) **Tensile strength vs. porosity**

Figure 1.1: **Effects of dissolved hydrogen on porosity and mechanical properties in sand cast aluminum and aluminum alloy bars** [1]

4. Chemical degassing where substances are added to the melt, thus reacting with aluminum and producing gases that then remove hydrogen similar to the gas purging method.

1.3. Objectives of work

Aim of the work is to develop a novel degassing system using electromagnetically driven melt flow.

Objectives are:

- Perform literature analysis to understand the criteria for bubble collapse and the measuring methods for quantifying the degassing results.

- Develop a low-temperature experimental setup to test bubble dispersion by electromagnetically created flow using GaInSn alloy, as it allows flow measurements for different degassing configurations. Use this setup to validate degassing potential of these configurations.

- Develop medium-scale aluminum experiments on bubble dispersion and demonstrate bubble refinement by the electromagnetically driven flow.

- Obtain experimental results for MHD numerical model validation. Develop a method that uses numerical model findings to predict bubble size in electromagnetically stirred aluminum.
- Predict industrial degassing unit operating parameters based on experimental findings.

1.4. Outline

To understand the degassing process, we shall first describe the fundamental physics behind it in section 2, which includes the formation, stability, and dynamics of gas bubbles in the liquid. Extra focus is put on specifying physical processes in the existing degassing methods and outlining the governing equations used for numerical calculations.

In section 3, the literature analysis is presented, focusing on the various degassing methods, the latest advances in them, and the newest research to put the proposed method in the context of the present situation in industry and research. The last subsection introduces permanent magnet machines and how they compare to other electromagnetic methods for metal transport.

Section 4 introduces the experimental setup used to model degassing process on a laboratory scale and thoroughly explains measured parameters, their importance, and techniques used to obtain the results.

Result analysis and discussion are presented in section 5, where the results of each measuring technique are shown together with the dimensionless analysis as part of the technology scaling process. The last section, section 6, summarizes obtained results, highlights the advantages and limitations of the proposed technology, and hypothesizes potential uses in the light alloy manufacturing industry.

2. THEORETICAL BACKGROUND

Bubble breakup in liquid metal by electromagnetic forces is a multiphysics problem incorporating multiple continuum mechanics branches. In this section, the established theory of the main aspects is discussed. Firstly, in Sec. 2.1, it is summarized how the gas solubility in metal establishes a need for degassing by introducing the sources of contamination, thus explaining hydrogen presence in aluminum. Secondly, since most degassing methods rely on inert gas injection, in Sec. 2.2, gas bubble stability in liquid metals is analyzed to understand the necessary criteria for bubble breakup. Thirdly, as scientific literature uses many dimensionless numbers to characterize the system and compare various models, the most often used are discussed in subsection 2.3. The value range of these parameters for this study is highlighted. Lastly, governing electromagnetism and fluid mechanics equations are outlined in Sec. 2.4. They form the foundation of equations that numerical methods use to solve the studied problem. Additionally, the main dimensionless groups characterizing electromagnetic stirring are defined there.

2.1. Gas solubility in metal

In physical chemistry, Henry's law states that the amount of dissolved gas in a liquid is proportional to its partial pressure above the liquid. Hydrogen, oxygen, and nitrogen are often of interest in metallurgy. Even though these gases are diatomic in atmospheric conditions, in liquid metals, they exist in an atomic form which means they undergo disassociation. For example, when hydrogen dissolves in metal, it disassociates according to Eq. (2.1) with equilibrium constant shown in Eq. (2.2).

$$H_2 \text{ (g)} \Longleftrightarrow 2H \text{ (solution)} \tag{2.1}$$

$$K_{H_2} = \frac{c_{H_2}^2}{p_{H_2}} \tag{2.2}$$

where K_{H_2} is the equilibrium constant and p_{H_2} is the partial pressure of hydrogen above melt in diatomic form, and solubility c_{H_2} is defined as weight percent.

From there, Sieverts' law [15] shown in (2.3) is obtained, and it states that solubility c_{H_2} of diatomic gas in metal is proportional to the square root of the partial pressure of the gas in thermodynamic equilibrium.

$$c_{H_2} = \sqrt{K_{H_2} \cdot p_{H_2}} \tag{2.3}$$

Hydrogen solubility in molten aluminum is low, so solubility measurements differ by source. In normal pressure above the melting point, it is in the range of 0.88 to 1.03 $\frac{\text{cm}^3}{100\text{ g}}$ [16]. However, when aluminum solidifies, maximum dissolved hydrogen concentration drops by an order of magnitude and is under 0.05 $\frac{\text{cm}^3}{100\text{ g}}$ [9]. This difference in solubility explains the formation of excess hydrogen in the form of pores if aluminum is not degassed beforehand and contains hydrogen above maximum solubility in liquid form.

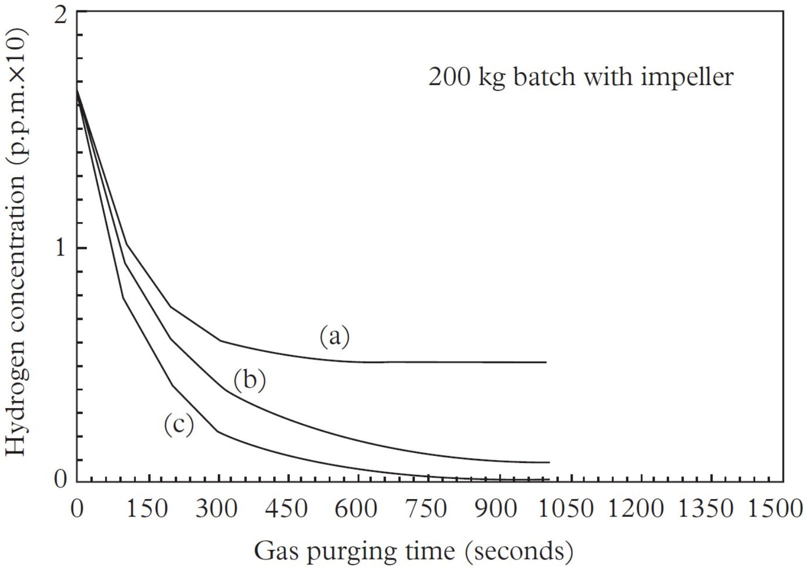

Figure 2.1: **Calculated curves for hydrogen removal: (a) the surface is completely exposed to air; (b) lid is closed; (c) closed lid and inert gas is blown on the surface** [2]

Empirically it has been shown that there is a notable difference in whether the degassing process is done with no lid, with a lid, or with a lid and argon atmosphere (see Fig. 2.1). Even in the time scale of tens of minutes, the agitated surface of aluminum can be polluted so quickly that degassing can not be done down to the lowest hydrogen concentration. These results can be understood better when hydrogen contamination sources are identified.

In the case of aluminum metallurgy, such sources are multiple. Firstly, hydrogen is in the atmosphere with a concentration of $5.5 \cdot 10^{-7}$ (relative volume part). Secondly, there is water vapor in the air. And thirdly, most often, aluminum is melted using gas torches, and water (vapor) is one of the combustion byproducts. When water is present, the following reactions with aluminum take place:

$$
\begin{aligned}
&2Al + 6H_2O \rightarrow 2Al(OH)_3 + 3H_2\\
&2Al + 4H_2O \rightarrow 2AlO(OH) + 3H_2\\
&2Al + 3H_2O \rightarrow Al_2O_3 + 3H_2
\end{aligned}
$$

In all these reactions, hydrogen is produced, which is the primary source of hydrogen contamination in aluminum production. Aluminum and water reactions are even studied in the context of hydrogen production [17]. These reactions are exothermic and thermodynamically favorable, even at room temperature. The fact that we do not observe them in normal conditions is due to the aluminum oxide Al_2O_3 layer that protects aluminum when it is in solid form. This protective layer is the reason why the free surface should be protruded as little as possible.

2.2. Stability of gas bubbles in liquid metal

In equilibrium, forces are in balance, ergo, the pressure inside the gas bubble p_{in} is composed of external pressure p_{out} (hydrostatic) and pressure caused by surface tension γ acting on the bubble with radius r (see Fig. 2.2). Eq. (2.4) shows that if we decrease bubble size, the pressure inside the bubble increases.

$$p_{in} = p_{out} + \frac{2\gamma}{r} \tag{2.4}$$

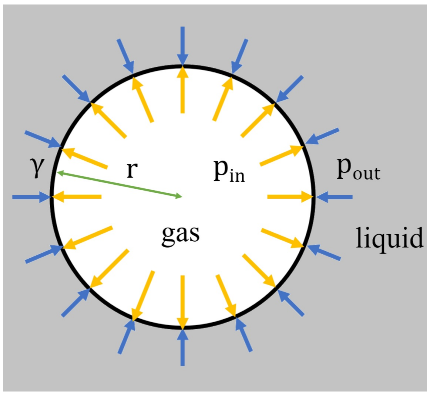

Figure 2.2: **Pressure of a gas bubble in a liquid**

Since gases are always less dense than any liquid, there is always Archimedes force which will drive the bubble to the top of the liquid (opposite the direction of the free fall acceleration g). Neglecting drag forces of metal flow and assuming laminar flow, we can estimate a characteristic rise time for gas bubbles. We can calculate terminal velocity v by balancing Archimedes's force and Stoke's drag force with expression (2.5).

$$v = \frac{2}{9}\frac{\rho g r^2}{\mu} \tag{2.5}$$

where ρ is the density of liquid, μ is the dynamic viscosity of liquid. Gas density here is ignored for simplicity.

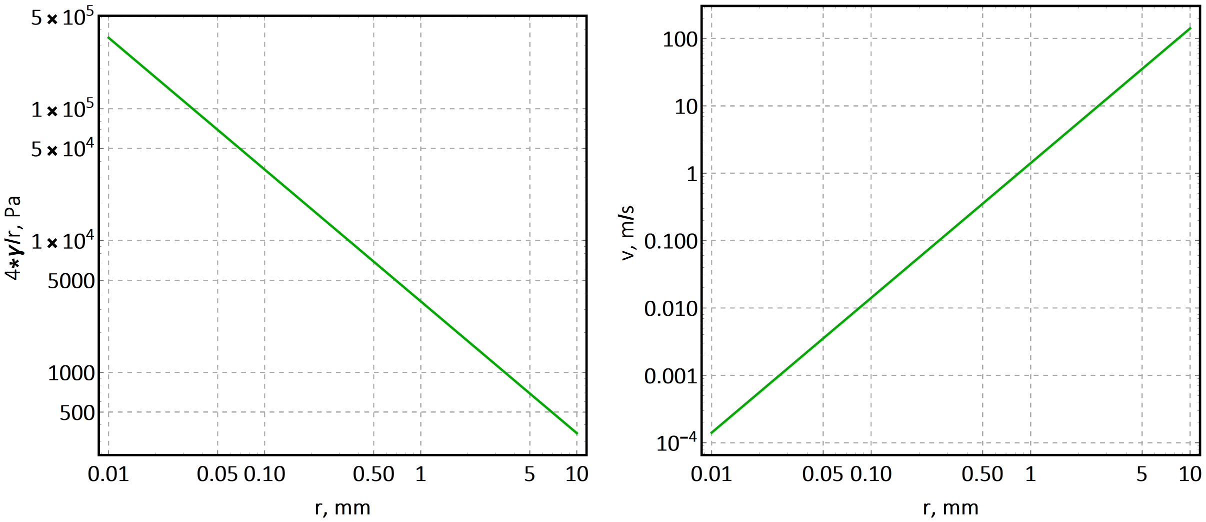

(a) **Surface tension pressure** *(b)* **Terminal velocity of the bubble**

Figure 2.3: **Bubble parameters in liquid aluminum as a function of bubble size; liquid aluminum parameters at 1000 K are used here:** $\rho = 2350\ kg/m^3$**,** $\mu = 3.7 \cdot 10^{-3} Pa \cdot s$**,** $\gamma = 0.865\ N/m$ [3]

Added pressure in a bubble caused by surface tension as a function of the bubble's radius is illustrated in Fig. 2.3a, and bubble rising terminal velocity as a function of radius is shown in Fig. 2.3b. The characteristic depth of a degassing unit is around 0.1..1.0 m. To achieve a rising time of more than a second, the bubble size should be smaller than a 1 mm radius. It is important to note here that the terminal velocity calculations in Fig. 2.3b are estimates for order of magnitude rather than exact predictions. They assume a solid spherical shape, laminar flow, and no external flow. The latter aspect is of high importance here since we can create an intensive recirculating flow that, in the right conditions, can collect and trap bubbles in the melt for far longer than the rise time in case of no flow.

Only two sources of forces can disintegrate a stable gas bubble in fluid - a dynamic pressure change or viscous stresses exerted on the liquid and gas interface. An example of bubble disintegration by viscous stresses is bubble elongation and breakup by shear flow right after gas injection in the fluid. Experiments of flow between parallel plates [4] show that bubbles can be stretched to extreme ratios as shown in Fig. 2.4. However, these observations are made at high viscosity, meaning the Reynolds number is low, which is not the case in our experiments or other degassing techniques.

The remaining bubble collapse mechanism creates a pressure difference on the liquid-gas interface. In the case of a turbulent flow, the pressure changes come from the dynamic pressure of the liquid flow, which chaotically varies in time. The fundamental mechanism of bubble breakup is complicated. According to a highly cited article by Hinze [5] there are two sources of forces in flow, three types of deformation, and six main types of flows

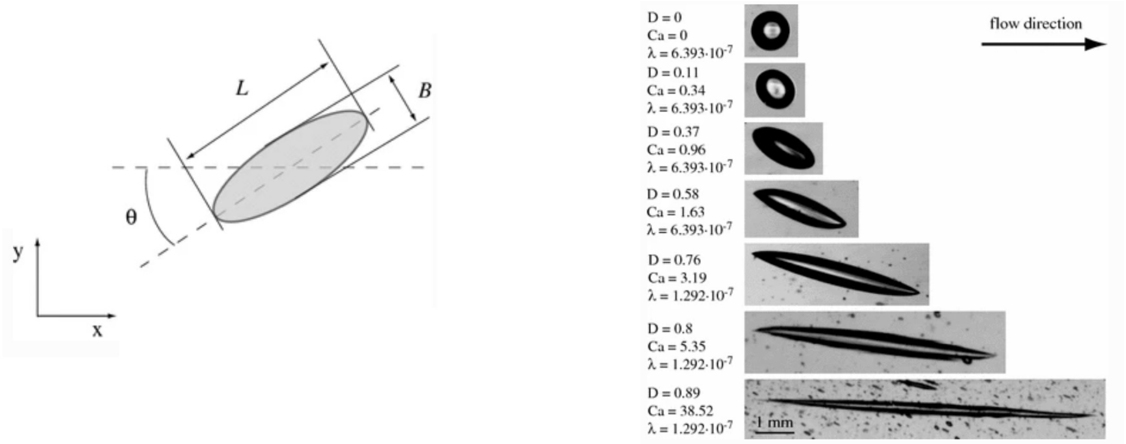

(a) **Deformed bubble**

(b) **Maximum steady-state deformation**

Figure 2.4: **Maximum steady-state bubble deformation D = (L−B)/(L+B) and orientation at different Capillary numbers** [4]

around a globule. It is proposed to use two dimensionless numbers to characterize the conditions of the flow. The first one is Weber number (2.6) which represents the ratio of drag force to surface tension force. To calculate Weber's number, fluids' density, velocity, and surface tension γ has to be known and a length scale l defined.

$$We = \frac{\rho v^2 l}{\gamma} \tag{2.6}$$

Yet Weber's number does not include viscosity for either of the mediums. To account for the effects of viscosity, Hinze introduces a second dimensionless group shown in E. (2.7). Where additionally, the dynamic viscosity of dispersed fluid comes into play. One can experimentally find critical Weber numbers for various viscosity ratios. In our case, viscosity ratio between dispersed medium μ_d to continuous medium μ_c is 10^{-2} and corresponding value of viscosity group is in range $Vi = 10^{-3}..10^{-2}$.

$$Vi = \frac{\mu_d}{\sqrt{\rho_d \gamma D}} \tag{2.7}$$

Knowing the viscosity ratio of fluids in question, we can find the critical Weber number (2.8) when the bubble is statistically likely to break up. According to Fig. 2.5 the critical Weber number for hyperbolic flow is around 2. However, we still face two problems finding specific criteria for bubble breakup conditions. The first one is seen in Fig. 2.5 in the curve of a Couette flow which tells us that at specific viscosity ratios, regardless of Weber number, a breakup does not happen (for example, a drop in air stream in Couette flow might experience rapid spinning but no disintegration). This highlights the fact that not all flow types are equal in the context of bubble breakup.

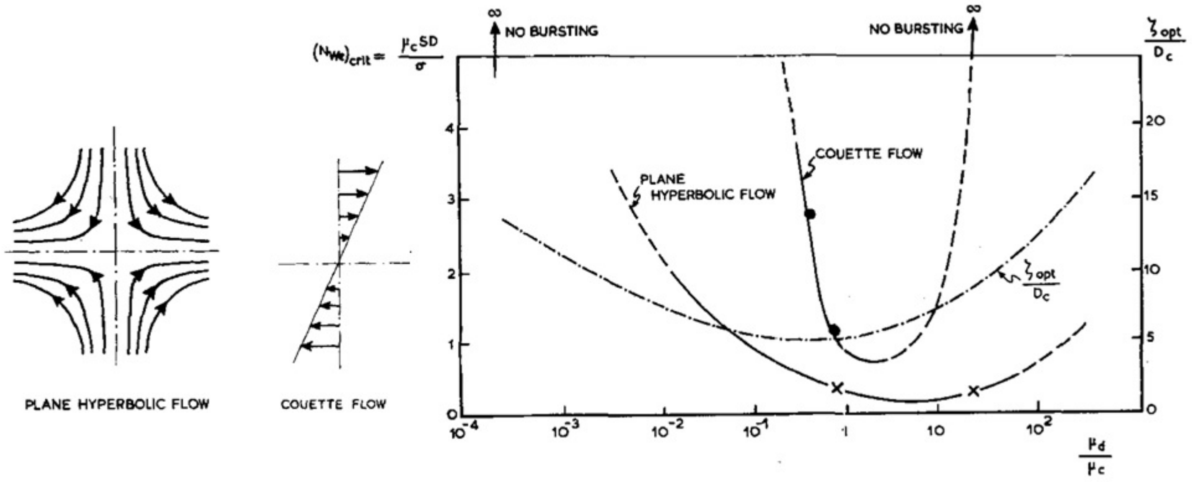

Figure 2.5: **Critical Weber number as a function of viscosity ratio for hyperbolic flow and Couette flow** [5]

When we know our target Weber number and try to achieve it, a second challenge appears when we examine velocity term $\bar{v}$ in (2.8).

$$We_{critical} = \frac{\rho \bar{v}^2 D_{max}}{\gamma} \tag{2.8}$$

It is defined as the average value across the flow field of the squares of velocity differences over a distance equal to D_{max} ! This becomes even more problematic when the bubble size is comparable to the boundary layer thickness. Therefore the author expresses velocity (2.9) in terms of energy input by assuming isotropic homogeneous turbulence.

$$\bar{v}^2 = C_1(\epsilon D_{max})^{2/3} \tag{2.9}$$

where ϵ is the turbulence kinetic energy (TKE) dissipation rate, a fundamental parameter indicative of the strength of turbulence measured in W/kg. With more assumptions like small Vi, experimentally found constants, and accounting for the statistical nature of bubble breakup, maximum bubble size can be expressed as Eq. (2.10):

$$D_{max95} = 0.725 \left(\frac{\gamma}{\rho_c} \right)^{3/5} (\epsilon)^{-2/5} \tag{2.10}$$

Two following interpretations of this result can be expressed.

1. Two key material properties - surface tension and density of continuous phase - form a ratio. Adjusting this allows us to interpret the results of water models and predict how these findings will change with the density and viscosity of liquid metal.

2. Increasing turbulence dissipation rate will refine the bubbles.

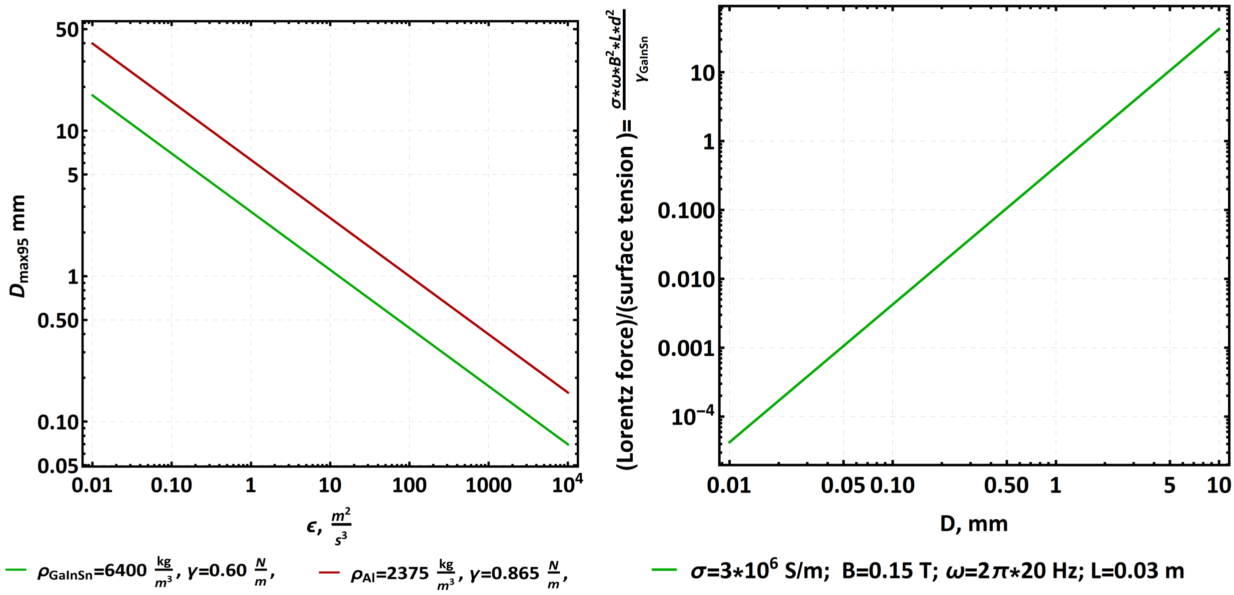

(a) **Maximum bubble size**

(b) **Pressure ratio**

Figure 2.6: **Maximum bubble size depending on TKE dissipation rate and order of magnitude estimate of EM to surface tension pressures**

Expression (2.10) is plotted against the TKE dissipation rate in Fig. 2.6a and it shows that increasing turbulence dissipation rate decreases maximum bubble size. Also, we can conclude that reaching fixed bubble size requires larger ϵ in the case of aluminum due to lower density and higher surface tension.

Empirically, gas purging studies have shown that for the best degassing efficiency the bubble sizes should be refined to size around $2-3$ mm [9]. To reach this size according to 2.6a we must achieve $\epsilon = 10\ W/kg$ in aluminum and at least $\epsilon = 1\ W/kg$ in GaInSn. Analysis of mechanically stirred water and bubble injection in relevant size [6] show that Reynolds number of at least $2 \cdot 10^4$ is necessary for bubble breakup to take place. Usually, bubbles are elongated and split into two or more daughter bubbles (as seen in Fig. 2.7). If the Reynolds number is higher or if the mother bubble is larger, the probability of multiple daughter bubbles increases, as shown in Fig. 2.8.

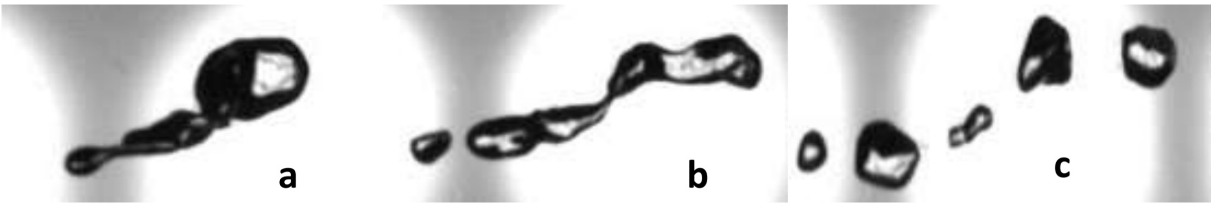

Figure 2.7: **Elongation prior breakup at Re=23850 for a 3.5 mm bubble [6]**

In conventional degassing processes, no electromagnetic forces interact with liquid metal. In this study, bubble movement will be in the presence of a magnetic field which can affect the shape, trajectory, and rising time of bubbles [18]. Moreover, the literature

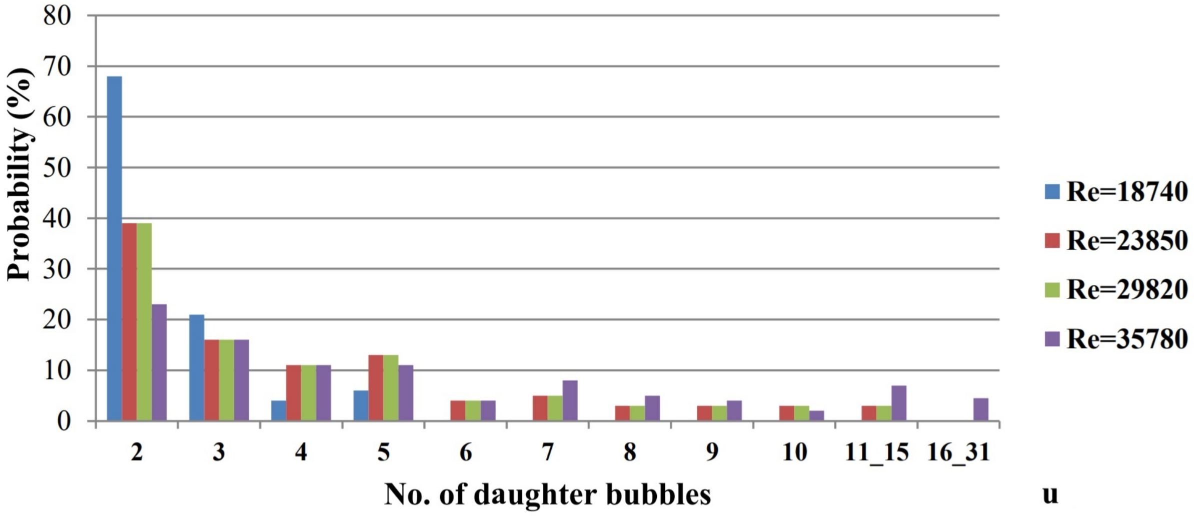

Figure 2.8: **Statistics of daughter bubble for mother bubble of size 3.5 mm** [6]

on bubble breakup and corresponding results mainly covers non-conducting fluids. Thus, we must introduce dimensionless criteria to quantify electromagnetic effects on bubble dynamics. We can analyze the ratio of electromagnetic forces and capillary forces. The order of magnitude of electromagnetic forces per unit area can be expressed as Eq. (2.11) and for pressure caused by surface tension as Eq. (2.12), where j is the induced current, B is the magnetic field induction, d is the diameter of the bubble, σ the electrical conductivity of the metal, B_0 is the amplitude of the alternating magnetic field and ω its frequency.

$$p_{EM} = \bar{f}_{EM} \cdot d = \vec{j} \times \vec{B} \cdot d \approx \frac{1}{2}\sigma\omega B_0^2 L \cdot d \tag{2.11}$$

$$p_{Laplace} = -\gamma \nabla \vec{n} \approx \frac{\gamma}{d} \tag{2.12}$$

Suppose we take the ratio of (2.11) to (2.12). In that case, we derive the formula (2.13), which characterizes a bubble's electromagnetic forces and surface tension forces and is plotted in Fig. 2.6b.

$$N_{EMtoLaplace} = \frac{\sigma\omega B_0^2 L \cdot d^2}{2\gamma} \tag{2.13}$$

A step-by-step derivation, and an alternative way of expressing the ratio of EM to surface tension forces are given in the attachment. Fig. 2.6b shows that EM forces dominate when $d > 5$ mm meaning that bubble shape could be affected by the presence of the magnetic field. However, the bubble target size of $1 - 4$ mm is below that; thus, we have to rely only on drag forces of turbulent flow to disperse the bubbles. To reiterate, EM forces in the studied setup will not break the gas bubbles in the metal.

2.3. Dimensionless numbers

In this subsection, we discuss the main dimensionless number groups which describe bubbles characteristics in fluids. Following dimensionless numbers are of interest to us: Reynolds number - Eq. (2.14); Eötvös number - Eq. (2.15); Morton number - Eq. (2.16); Froude number - Eq. (2.17) and Weber number Eq. (2.18). Here velocity is denoted with u, length scale is L, kinematic viscosity ν, density ρ, surface tension γ, dynamic viscosity μ. Subscript l characterizes quantities for liquid while b for the bubble.

$$Re = \frac{\text{Inertial forces}}{\text{Viscous forces}} = \frac{uL}{\nu} \tag{2.14}$$

$$Eo = \frac{\text{Buoyancy}}{\text{Surface tension force}} = \frac{g(\rho_l - \rho_b)L^2}{\gamma} \tag{2.15}$$

$$Mo = \frac{We^3}{Fr \cdot Re^4} = \frac{g\mu^4(\rho_l - \rho_b)}{\rho_l^2\gamma^3} \tag{2.16}$$

$$Fr = \frac{\text{Inertial forces}}{\text{Gravity force}} = \frac{u^2}{gL} \tag{2.17}$$

$$We = \frac{\text{Inertial forces}}{\text{Surface tension force}} = \frac{\rho_l u_c^2 L}{\gamma} \tag{2.18}$$

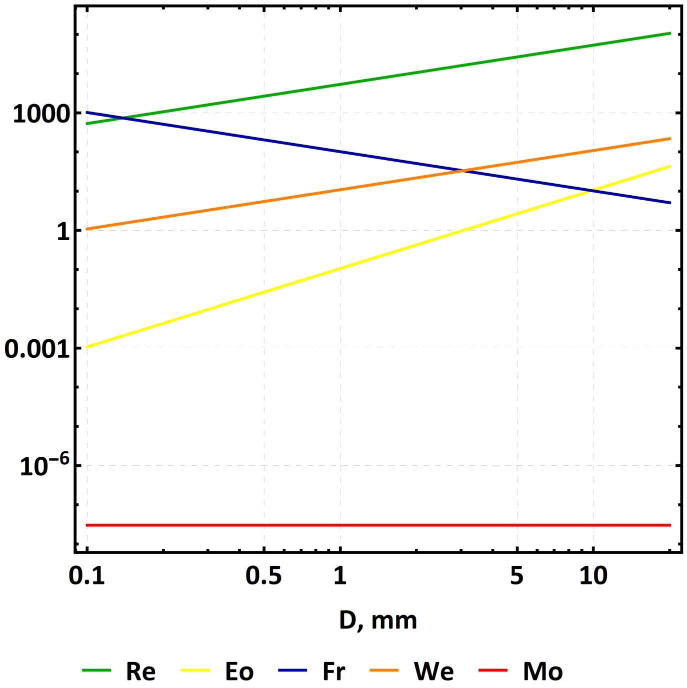

Figure 2.9: **Important dimensionless numbers as a function of bubble size; Constants and dimensions are taken to resemble the GaInSn laboratory experiment**

In Fig. 2.9 the aforementioned parameters are plotted as a function of bubble size. Reynolds number is larger than 10^3 across the length scale, so we expect to deal with a turbulent flow. Eötvös number reaches parity at around 4 mm. Froude number is expected to be considerably larger than unity - $Fr \gg 1$. This means that the inertial and centrifugal forces dominate, and the flow is supercritical (a flow whose velocity is faster than the wave velocity). Only Froude number decreases with the increase of bubble size, and Eötvös number is the one with the largest slope.

In Fig. 2.10, a Grace diagram is shown with the highlighted areas corresponding to experiments done within this thesis. According to it, we will see wobbling shapes which is reasonable since that is observed before the bubble collapse.

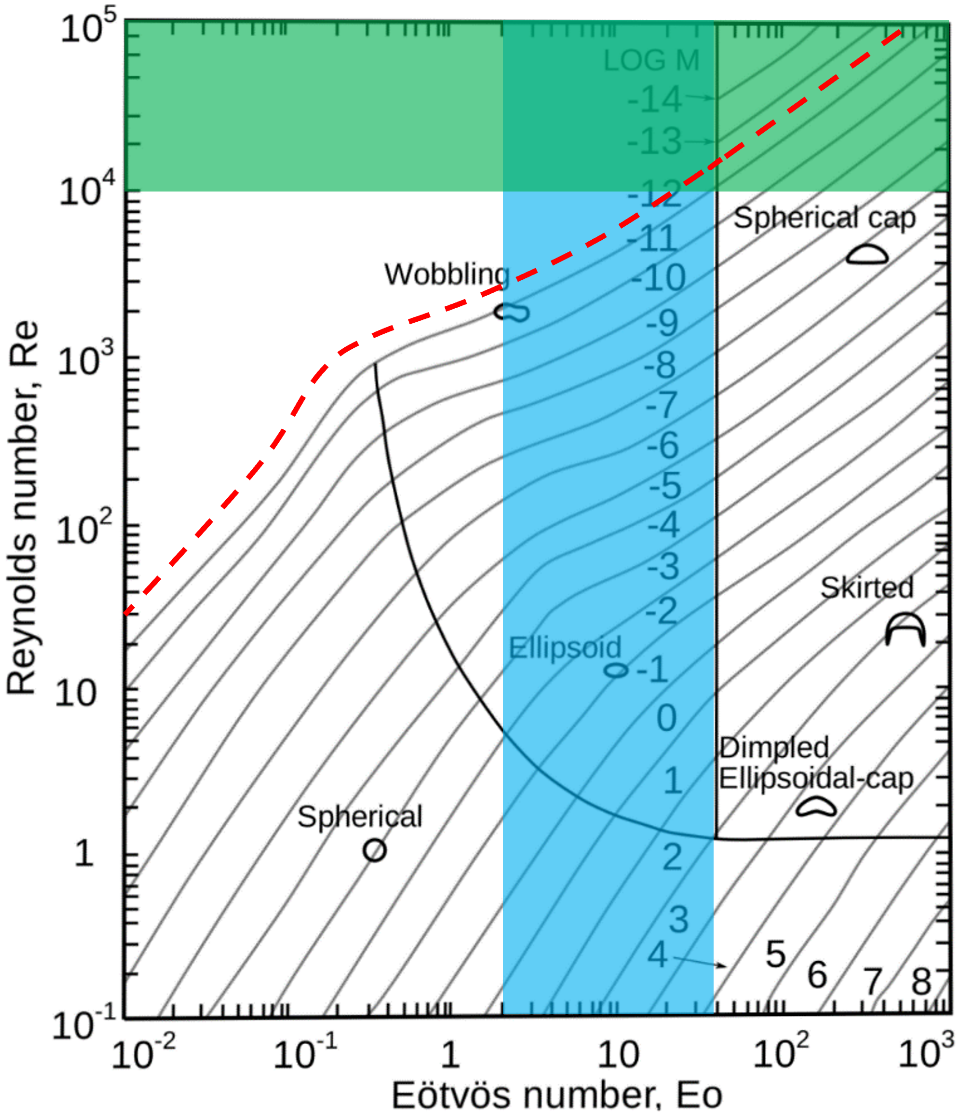

Figure 2.10: **Shape approximation to Reynolds, Eötvös, and Morton number [7]; Green shading represents the range of Reynolds number during our experiments, blue shading represents Eötvös number for bubbles from 4 to 20 mm, and the red dashed line is the logarithm of Morton number, taking into account GaInSn properties**

2.4. Governing electromagnetism and fluid mechanics equations

To describe fluid flow in the container being stirred by a moving permanent magnet system, it is necessary to use a set of electromagnetism and fluid mechanics equations. In this case, the rotating permanent magnet cause a time-changing magnetic field, which are generally described with Maxwell's laws (2.19) - (2.22). Here E and B are accordingly the electric and magnetic fields, ρ_q is the charge and J the current density and ϵ_0 the permittivity while μ_0 the permeability of free space.

$$\nabla \cdot \mathbf{E} = \frac{\rho_q}{\epsilon_0} \tag{2.19}$$

$$\nabla \cdot \mathbf{B} = 0 \tag{2.20}$$

$$\nabla \times \mathbf{E} = -\frac{\partial \mathbf{B}}{\partial t} \tag{2.21}$$

$$\nabla \times \mathbf{B} = \mu_0 \Big(\mathbf{J} + \epsilon_0 \frac{\partial \mathbf{E}}{\partial t} \Big) \tag{2.22}$$

According to Faraday's induction law (2.21), a changing magnetic field in a conductive media induces currents. This means that magnetic field and current density distributions simultaneously exist in the container. Lorentz force (2.23) acts on a particle with charge q and velocity u in a magnetic field, it is comprised of force caused by the electric field and the magnetic field.

$$\mathbf{f} = q(\mathbf{E} + \mathbf{u} \times \mathbf{B}) \tag{2.23}$$

In a continuous medium, the Lorentz force is written as in Eq. (2.24) where the current density is obtained from Ohm's law (2.25), where σ is the electrical conductivity.

$$\mathbf{f} = \rho_e \mathbf{E} + \mathbf{J} \times \mathbf{B} \tag{2.24}$$

$$\mathbf{J} = \sigma(\mathbf{E} + \mathbf{u} \times \mathbf{B}) \tag{2.25}$$

To understand which member in equation (2.24) dominates, we shall do order of magnitude estimates, τ will denote time scale while l the length scale. First part is $\rho_e \mathbf{E} \sim \frac{u\tau_e}{l} JB$ [19] and the term $\frac{u\tau_e}{l} JB \sim 10^{-18}$ thus the second part $\mathbf{J} \times \mathbf{B}$ dominates in Lorentz force. As a result Eq. (2.24) reduces to (2.26).

$$\mathbf{f} = \mathbf{J} \times \mathbf{B} \tag{2.26}$$

The current obeys continuity equation (2.27) which is derived from charge conservation. Since ρ_e is small, the right side term $\frac{\partial \rho_e}{\partial t}$ approaches 0.

$$\nabla \cdot \mathbf{J} = \frac{\partial \rho_e}{\partial t} \tag{2.27}$$

Ampere's law (2.22) now simplifies, since we can discard displacement currents $\epsilon_0 \frac{\partial \mathbf{B}}{\partial t}$. As a result, the system of electromagnetic equations is reduced to (2.28).

$$\begin{cases} \nabla \times \mathbf{B} = \mu_0 \mathbf{J} \\ \nabla \cdot \mathbf{J} = \dfrac{\partial \rho_e}{\partial t} \\ \nabla \times \mathbf{E} = -\dfrac{\partial \mathbf{B}}{\partial t} \\ \nabla \cdot \mathbf{B} = 0 \\ \mathbf{J} = \sigma(\mathbf{E} + \mathbf{u} \times \mathbf{B}) \\ \mathbf{f} = \mathbf{J} \times \mathbf{B} \end{cases} \tag{2.28}$$

With this system equation, it is possible to describe electromagnetism for MHD [19]. Practically solving these equations for an entire system is mostly done with numerical methods.

If we combine Ohm's, Faraday's, and Ampere's law, it is possible to obtain magnetic field transport equation (2.29) that relates magnetic field induction **B** to velocity **u** of conducting fluid. It describes the evolution of the magnetic field in time, where the first right side term characterizes advective transport due to conductive fluid velocity **u**. The second term describes the diffusive transport of magnetic field where $\frac{1}{\sigma \mu}$ is the diffusion coefficient with unit m^2/s.

$$\frac{\partial \mathbf{B}}{\partial t} = \underbrace{\nabla \times (\mathbf{u} \times \mathbf{B})}_{\text{advection}} + \underbrace{\frac{1}{\sigma \mu} \nabla^2 \mathbf{B}}_{\text{diffsuion}} \tag{2.29}$$

One can compare the magnitude of the advection term and diffusion term in magnetic field transport equation (2.29) to distinguish regimes where one term is dominant. The resulting quantity is a dimensionless number called magnetic Reynolds number (2.30).

$$R_m = UL\sigma\mu \tag{2.30}$$

Our laboratory setup has the following characteristic values: $U = 2\ m/s$; $L = R = 0.1\ m$;

$\sigma = 3 \cdot 10^6\ S/m$ and $\mu = 4\pi \cdot 10^{-7}\ kg \cdot m/A^2 \cdot s^2$. This gives $R_m = 0.5$, meaning that the magnetic field, for the most part, will be weakly affected by the liquid metal flow in the experimental laboratory model. Using the dimensions of the proposed industrial unit and aluminum properties (see table 4.2 and table 4.1 in section 4) magnetic Reynolds number is expected to be a magnitude higher than in the laboratory model.

Some other useful dimensionless numbers are used in subsection 5.5. They are Hartmann number Eq. (2.31), Stuart number Eq. (2.32), Péclet number Eq. (2.33) and dimensionless frequency Eq. (2.34).

$$Ha = \frac{\text{EM forces}}{\text{Viscous forces}} = BL\sqrt{\frac{\sigma}{\mu}} \tag{2.31}$$

$$N = \frac{\text{EM forces}}{\text{Inertial forces}} = \frac{\sigma}{\rho}\frac{B^2}{\omega} \tag{2.32}$$

$$Pe = \frac{\text{Advective mass transport}}{\text{Diffusive mass transport}} = \frac{uL}{D} \tag{2.33}$$

Dimensionless frequency is the ratio of applied magnetic field frequency to the inverse of magnetic field diffusion time. Diffusion time is the length of time in which an applied magnetic field penetrates a stationary object with conductivity σ and permeability μ. Analytical solutions for magnetic field diffusion exist for simple geometries [20]. Characteristic magnetic field diffusion time here is chosen to be $\tau_B = \mu\sigma L^2$

$$\Omega_D = \omega\sigma\mu_0 L^2 \tag{2.34}$$

A slightly different form of Maxwell's equations is used in numerical modeling of this problem by Berenis et al. [21]. Magnetic vector potential $\mathbf{A}$ is introduced which in respect to $\mathbf{B}$ is expressed as (2.35) and the current density is written as (2.36):

$$\nabla \times \mathbf{A} = \mathbf{B} \tag{2.35}$$

$$\mathbf{J} = \sigma(-\nabla\phi - \frac{\partial \mathbf{A}}{\partial t} + \mathbf{v} \times \mathbf{B}) \tag{2.36}$$

And the only electromagnetic force we are interested in is the Lorentz force which remains the same as introduced previously.

In general, fluid dynamics of incompressible fluids are governed by the Navier-Stokes equation (2.37). The first term is the convective derivation of the velocity containing a time-varying acceleration part and convective transport of momentum. The second term is the gradient of pressure. The third term describes the diffusion of the velocity field.

The fourth and fifth terms are volume forces. The fourth being gravity but specific to our case, is the fifth - the Lorentz force (2.26). Lorentz force connects the fluid dynamics with electromagnetism, thus creating a need for a feedback loop and complicating the MHD calculation, which now can not be done independently.

$$\underbrace{\rho\left(\frac{\partial \mathbf{u}}{\partial t}+\mathbf{u}\cdot\nabla\mathbf{u}\right)}_{1}=-\underbrace{\nabla p}_{2}+\underbrace{\eta\nabla^2\mathbf{u}}_{3}+\underbrace{\rho\mathbf{g}}_{4}+\underbrace{\mathbf{J}\times\mathbf{B}}_{5} \tag{2.37}$$

Numerical calculations discussed in this work were performed with the OpenFOAM open-source code using the SIMPLE algorithm for the steady-state incompressible Navier–Stokes equation (2.38)

$$\mathbf{u}\cdot\nabla\mathbf{u}+\nabla\left(\frac{p}{\rho}\right)-\nu\nabla^2\mathbf{u}+\frac{\mathbf{F}}{\rho}=0 \tag{2.38}$$

where u is the velocity; p is the pressure; ρ is the density; and F is the volume force. The inertia of the fluid is assumed to be sufficiently large to neglect the oscillatory component of force. We considered only closed containers; therefore, all walls have a no-slip boundary condition.

Since we study flows with Reynolds number of 10^5, turbulence models must be used. Spalart–Allmaras turbulence model was used for most velocity calculations across the frequency domain. The Menter shear stress transport (SST) turbulence model was used to obtain turbulence kinetic energy dissipation rate. The SST turbulence model does not directly calculate TKE dissipation rate ϵ but does calculate turbulent kinetic energy k and specific rate of dissipation ω. TKE dissipation rate then can be simply calculated using the relationship (2.39)

$$\epsilon = C_\mu k\omega \tag{2.39}$$

where C_{mu}=0.09 is a constant used in the model. These findings are later used to predict the size of bubbles if gas is to be injected in such flow without calculating the actual two-phase flow.

3. LITERATURE OVERVIEW

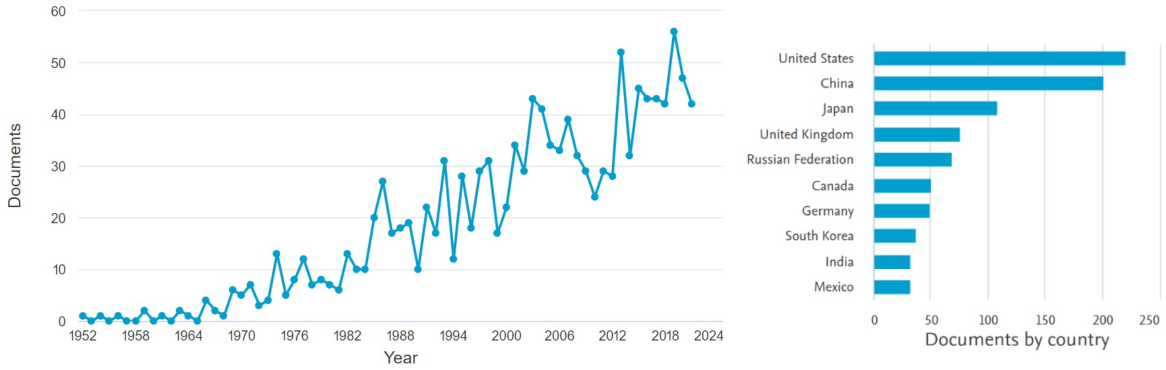

Figure 3.1: **Scopus library results for search terms ”aluminum” + ”degassing” from year 1952 to 2021**

Aluminum production on an industrial scale has been happening for more than a century with the development of the Hall–Héroult process. Scientific articles on aluminum degassing date back to at least the year 1952 and most contributions are from countries with prominent aluminum industry, as can be seen in Fig. 3.1 where a Scopus search is shown displaying the popularity of keywords ”aluminum” and ”degassing”. Thus this chapter will be a literature summary of degassing methods, bubble dynamics in liquid metal, and permanent magnet systems for liquid metal stirring.

3.1. Existing aluminum degassing methods

Multiple degassing methods exist, such as gas purging, ultrasound, vacuum, and tablet degassing. They differ technologically, but the underlying mechanisms of hydrogen removal are always via diffusion. Suppose nothing is done to an aluminum crucible. In that case, the dissolved hydrogen moves in the direction of the concentration gradient to the free surface (assuming a lower H_2 concentration in air). Such a scenario is impractically slow in the case of an aluminum furnace with a characteristic size of 1 m. So all existing methods aim to accelerate the diffusion rate by manipulating the pressure, surface area, and/ or the distance to a place of lower concentration. In the case of gas purging, the free surface area increases, and the distance decreases. Tablet degassing uses the same principle but a completely different gas source via chemical reactions. In vacuum degassing, the ambient pressure is lowered. In ultrasound degassing, pressure oscillations cause a rectified diffusion process. All of the methods are explained in the following sub-subsections. Still, the focus is on gas purging since this method shares the most similarities to the electromagnetic degassing studied in this work.

3.1.1. Gas purging

Gas purging is achieved by injecting inert gas (usually Argon) into the metal. The gas collects hydrogen bubbles and leaves the metal through its free surface. While there is some hydrogen concentration in the melt, an inert gas bubble has zero hydrogen concentration, so the hydrogen diffuses from the melt into the inert gas bubble. The factors contributing to an accelerated diffusion are vastly larger surface area and the reduction of the hydrogen's mean path to travel.

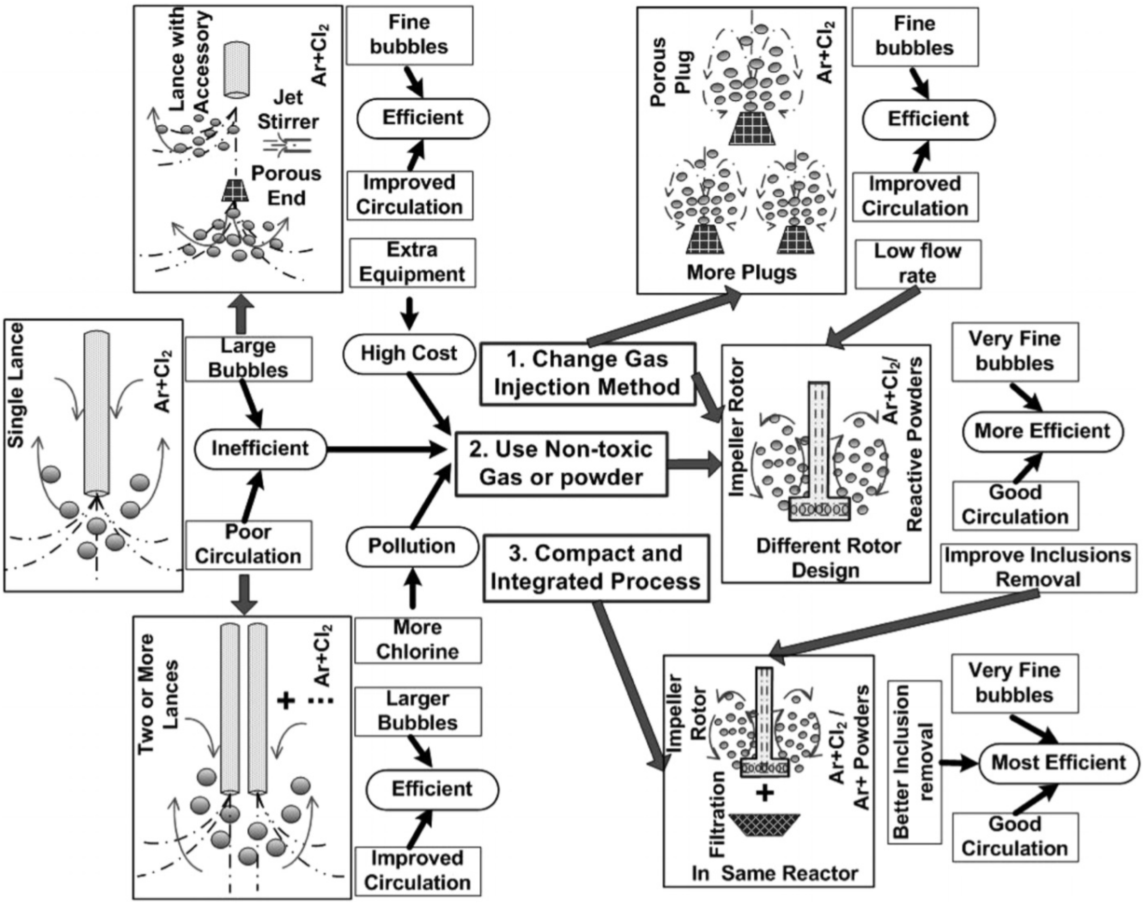

Figure 3.2: **Various degassing approaches** [8]

Overall, gas purging is the most researched method, and through the past 40 years [8] has gone through many iterations, as can be seen in Fig. 3.2. Optimization has happened in geometry, specifically nozzle design, which can rotate and expel gas or powder to refine the gas bubbles to a specific size. The main variables to adjust in the process are volumetric rate, rotational speed, and bubble size and flow rate. One of the challenges here is to ensure highly turbulent flow near the gas inlet while maintaining a flow type with minimal surface deformation since they can lead to oxide trapping in melt in the form of bifilms [22] which worsens mechanical properties. Another aim is to have a flow that maximizes argon bubble rising time to improve degassing efficiency since hydrogen trapping by inert gas bubbles is a physical process.

The most primitive way to do gas purging is gas injection via lance-producing bubbles with the size of centimeters which has thermodynamic efficiency around 10..20 %. Thermodynamic efficiency here is defined as the hydrogen content in the carrier gas bubble vs the maximum possible hydrogen concentration in the bubble (determined by the hydrogen concentration in the melt). Using a porous plug at the end of a lance produces finer bubbles, increasing efficiency to 30..40 %.

Advancement in gas purging methods came in 1966 [23] when the ”Spinning Nozzle Inert Flotation” (SNIF) process was introduced. Such a method can produce fine bubbles measured in millimeters, achieving degassing efficiencies close to 100 % [9]. The key in the SNIF process is inserting a spinning rotor and a stator that encloses the rotor. Massive shear forces are created in the gap between the rotor and the stator. Thus, the gas is injected precisely there. The benefit of this approach is the efficiency mentioned earlier and the confinement of the turbulent flow, thus reducing surface deformations. The correlation of the degassing efficiency and the degassing bubble size for a 250 kg crucible furnace is shown in Fig. 3.3 and clearly illustrates that the bubble size is critical to degassing efficiency in this process. In practice, the rotary degassing process is aided by adding fluxing agents, which improves hydrogen removal but causes an increase in inclusions [24]. These inclusions must be removed, and it is usually done by filtration, which is the last step before the casting.

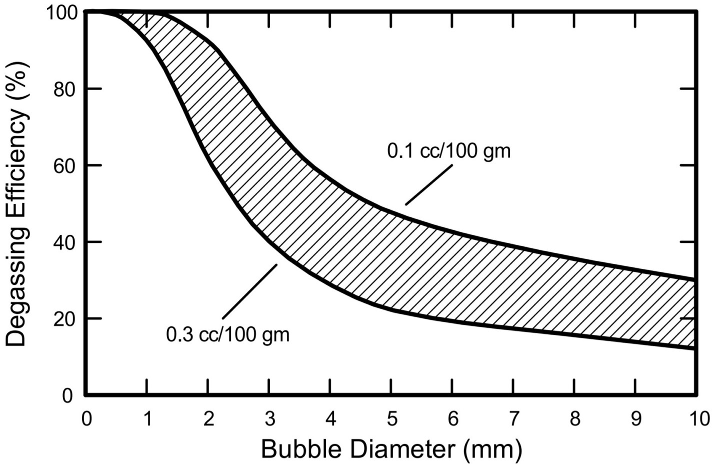

Figure 3.3: **Degassing efficiency at two hydrogen content levels** [9]

Currently, there is considerable research focus on the impeller and flow optimization to address degassing challenges by

1. reducing the inert gas consumption and processing time by reducing the average bubble size and increasing bubble rise time [25];

2. reducing the surface deformations and vortex generation that can accelerate the reabsorption of hydrogen and entrapment of oxide films[26];
3. increasing impeller longevity which is degraded by its direct contact with the melt [25].

Although these obstacles have been partly solved or limited, the demand for better methods exists in the industry, and new studies [27, 28, 29, 30] have been conducted to find more effective and sustainable aluminum degassing methods for large aluminum production lines.

3.1.2. Ultrasound

Another mechanism for bubble collapse is to create pressure oscillations with high enough amplitude [31, 32]. These oscillations fall in the category of mechanical ultrasound waves with a usual frequency in the range of 10-30 KHz. Pressure amplitude of mechanical waves with intensity I is described with equations (3.1) and (3.2):

$$p_{max} = p_0 + \sqrt{2\rho c I} \tag{3.1}$$

$$p_{min} = p_0 - \sqrt{2\rho c I} \tag{3.2}$$

where p_0 is the ambient pressure, ρ is the density, and c is sound velocity in liquid medium. The minimum threshold for causing cavitation for example in liquid aluminum is 10 W/cm^2 [33]. When mechanical ultrasound is applied, an instantaneous variation in local pressure takes place. During the phase of low-pressure tiny gas bubbles form, which at the high-pressure phase collapse and produce shock waves. Dissolved hydrogen removal happens through a diffusion process, and these oscillations greatly increase the mass transfer rate through rectified diffusion [34]. According to the article: *"During this bubble oscillation, the pressure within the bubble decreases as it expands and increases as it compresses. Consequently, gas and/ or vapor diffuse in and out of the bubble due to the differences in pressure between the interior and exterior of the bubble. Several effects contribute to an unequal diffusion in and out of the bubble."*. This result is a vastly increased diffusion rate compared to the case where nothing is done. For example, aluminum degassing for samples of 0.2 kg to 2.0 kg happens in the range of 1-7 minutes depending on conditions [33].

Ultrasound degassing is very effective for small volumes but loses applicability when the aluminum volume is scaled. That happens because ultrasound intensity drops off quickly with distance making the degassing localized only around the probe.

There also exists a variation of this method where the mechanical energy in the form of ultrasound is created electromagnetically with a coil. There are proposals using a top coil from the top surface [35] to achieve contactless ultrasonic melt treatment. In the cases where induction crucibles are used for melting the metal a similar approach can be applied. With the same coil, it is possible to perform a electromagnetically-induced vibrational degassing operation [36]. Both of the mentioned approaches are not used in the aluminum industry.

3.1.3. Vacuum degassing

In vacuum degassing, the pressure above the melt is reduced to a fraction of normal pressure to accelerate gas removal [37]. When partial pressure is reduced, the maximum hydrogen solubility drops according to Sievert's law shown in Eq. (2.3). A practical analogy is the first opening of a carbonated drink. There CO_2 is dissolved in water and is stable in the elevated pressure of $2 - 3.5$ atm. The pressure is reduced to atmospheric when the bottle is opened, and CO_2 starts escaping. However, despite the high degree of saturation, if the water is not perturbed, CO_2 escapes slowly with a characteristic time of hours. That is why the vacuum degassing method is often combined with ultrasonic degassing [38] since vacuum degassing alone is too slow. For example, for an 800 g aluminum sample, the degassing process takes 20-30 minutes [33], and the duration would only increase with the aluminum volume rise. Adding another perturbation in the form of ultrasound increases process time by an order of magnitude.

3.1.4. Tablet degassing

Tablet degassing works by adding compounds that react with aluminum and produce gases that are less soluble in aluminum than hydrogen. As an example, hexachloroethane (C_2Cl_6) is added as a solid, and various reactions [39] take place:

$$Al + C_2Cl_6 \rightarrow Al + C_2Cl_4 + Cl_2$$

$$2Al + 3Cl_2 \rightarrow 2AlCl_3$$

$$Al + C_2Cl_4 \rightarrow Al + CCl_4 + C$$

$$Al + CCl_4 \rightarrow Al + 2Cl_2 + C$$

$$Al + C_2Cl_6(\text{solid}) \rightarrow Al + C_2Cl_6(\text{gaseous})$$

Produced gases utilize the same principle as gas purging and remove dissolved hydrogen via insoluble gases that rise to the top.

3.2. Bubble Dynamics in Liquid Metals

An extensive review of bubble dynamics in liquid metals is found in a review article [40] by Haas et al. It covers measurement methods, emphasizing the applicability to liquid metals and discussing their shortcomings and difficulties. The most relevant to this thesis is the discussion about the bubble formation mechanism at nozzles and purging plugs. Firstly, it shows that the gas inlet's surface properties dictate bubble formation. In the case of bubble generation through a sieve tray (see Fig. 3.4), wetted and non-wetted surfaces produce a radically different result. Wetted sieve creates smaller bubbles that are more homogeneously dispersed through more holes [10]. Articles also highlight the gas flow rate limits before bubbles from neighboring holes join together and form a blanket of gas instead of individual bubbles. Laboratory experiments in this thesis use a single orifice for gas injection; however, wetting the crucible walls becomes essential due to the small size. If the flow is not strong enough and the gas inlet is close to a wall ($< 1\ cm$), a gas pocket might slip between the wall and the metal. This had happened in initial laboratory aluminum experiments and of course is unfavorable to the degassing process.

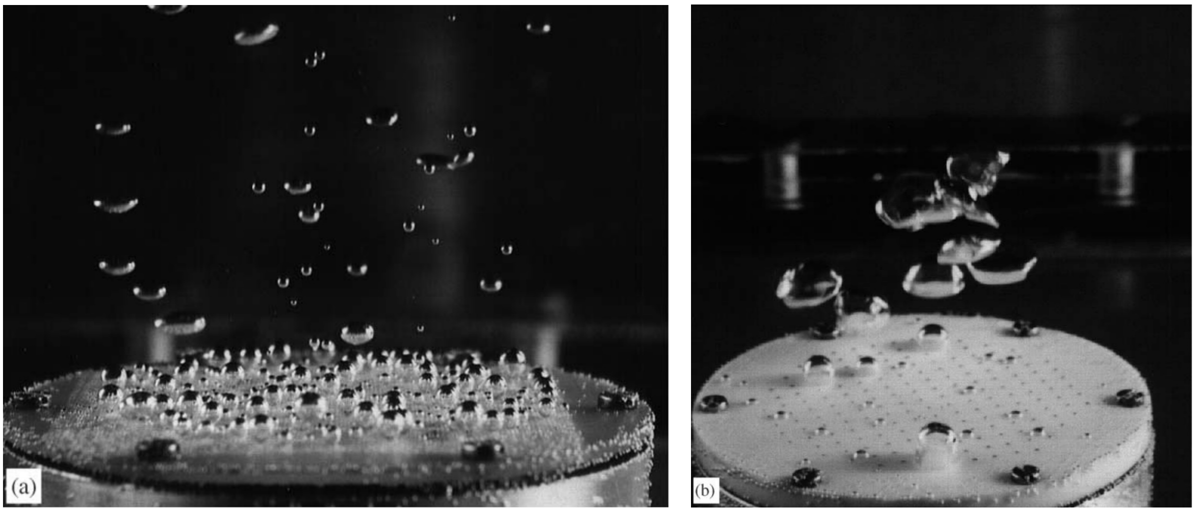

(a) **Wetted** *(b)* **Non-wetted**

Figure 3.4: **Bubble generation trough copper and Teflon sieves with the same flow rate** $W = 3.33 cm^3/s$ [10]

Secondly, the gas flow rate and gas inlet size determine the bubble size. A recent article "Bubble characteristics and turbulent dissipation rate in horizontal bubbly pipe flow" [41] collects critical Weber numbers for different turbulent flow setups. They are usually in the range of 0.585 to 2.35. The article experimentally shows a more significant number of bubbles right after birth. Still, at a later time, they experience coalescence and reach a stable count in the turbulent pipe flow. Bubble size spectra (number of observed bubbles vs bubble size) follow a $-10/3$ power law.

Gas bubble diameter moderately increases with increasing gas flow rate [42]. The average volume of a gas bubble is roughly proportional to the gas injection flow rate. Noteworthy is the fact that if the flow rate is controlled (e.g., with a mass flow controller), one can measure the frequency of the bubble detachment process and make predictions of the bubble size. An example of such correlations can be seen in this study [43].

Gas bubble diameter depends on the injection orifice size [44]. They have investigated the dynamics of bubble formation from submerged orifices ranging from 0.04 to 0.8 mm and found the different mechanisms of bubble formation compared with millimeter-range orifices. Regardless, the correlation remains the same - the smaller the orifice, the finer bubbles can be produced. Cross-flowing liquid significantly impacts the bubble generation at the orifice [45]. The simulation results also suggest that the bubble formation frequency and the detached bubble size can be controlled by adjusting the liquid flow.

Two-phase flows are commonly found in industrial processes, e.g., in chemical reactors, hydrotransport, and biomedical treatment [46, 47]. Besagni [48] highlights multiple lengths scales relevant to chemical reactors' processes. Starting from the smallest, there is the molecular scale at which fundamental chemistry is necessary to study the interfacial phenomena, catalysts, and gas conversion processes. Next is the bubble scale, where theoretical and experimental exist to quantify and understand bubble size distributions, shapes, and single bubble dynamics. The author also describes the existence of "non-coalescence-induced" bubble dynamics and "coalescence-induced" behavior as models of break-up and coalescence. Following is the "reactor scale", where flow patterns, the mean residence time of the dispersed phase, dynamics of mesoscale clusters, liquid recirculation, and fluid back mixing have been studied. The largest scale is the industrial scale. In it, scale-up methods are applied to estimate the fluid dynamics reactors based on the laboratory-scale experimental facilities.

Review article about chemical reactors [49] focuses on bubble column reactors, their description, design, operation, and application area. They present fluid dynamics and encountered regime analysis together with parameters characterizing the operation.

Experiments in liquid metal are far fewer because of the challenges that come with the aggressive medium of molten metal. Also, imaging of metal is much more difficult because metal is opaque. That means directly observing bubbles in the melt is possible only with advanced methods such as x-ray imaging [50], or neutron radiography [51]. Nevertheless, in HZDR, they have built a large-scale test facility for modeling bubble behavior and liquid metal, which models two-phase flows in a steel ladle [52]. The test facility and the corresponding measuring systems serve as a powerful and flexible experimental platform for modeling complex multiphase flows in metallurgy and casting. The paper presents the first measurements of the gas distribution close to the free liquid metal surface for various gas flow rates, plug positions, and types. They characterize flow regimes and quantify void fraction, liquid and bubble velocities, and properties. This information can then provide unknown boundary conditions for numerical simulations of various metallurgical reactors, such as steelmaking converters or ladles.

3.3. Permanent magnet systems

MHD machines and devices can pump, stir or damp molten metal and affect its crystallization structure [53]. Focusing on pumping and stirring problems: many machines use alternating current (AC) inductors to create the alternating magnetic field. Coil configuration is made so that the time-averaged Lorentz force is oriented in a particular direction. This way, metal can be pumped contactlessly without moving parts (except electrons). That is why they are used in metal transport applications where conventional methods are obsolete due to the high temperatures and the chemically aggressive medium.

Permanent magnet systems can generate strong magnetic fields. If the permanent magnet is moved (often rotated), it is an energy-effective way of creating an alternating magnetic field compared to traveling field inductors since the magnetic field in a permanent magnet is maintained with ”no cost”. Hence, permanent magnetic stirring can be superior in cost and operational aspects compared to electromagnetic stirring based on AC [54]. As of now, permanent magnet pumps have been constructed for a couple of decades [55]. In metallurgy, permanent magnet stirrers are applied for aluminum melting furnaces [56], but overall it is a relatively new technology. Depending on temperature requirements, samarium-cobalt or NdFeB permanent magnets are used with a remanent magnetization of 0.8 to 1.4 T. Depending on the geometry, physical properties of metal, and performance requirements, dipole or multi-pole devices are used. As a general rule of thumb, if the channel wall thickness is low multi-pole devices are better, but if the distance from the magnetic field source to metal is large, then dipole becomes better in creating larger forces in metal [57]. This can be explained by the magnetic field decay of dipole fields compared to multi-pole fields. The dipole magnetic field has the slowest decay with the distance, which is why it was chosen as the magnetic field source in this study.

In this work, a single dipole is used to stir the metal, which in different geometries has been studied by other authors. Grants [12] studied four configurations of a rotating magnetic dipole-driven turbulent flow in an electrically conducting liquid cylinder. It confirms that the setup used in this work (axis of magnets rotation parallel to the metal cylinder axis) does yield the fastest mean velocity. Also, the article highlights an important finding that up to a distance that is comparable to the magnet size, smaller permanent magnets can be used to achieve the same EM interaction if the rotational velocity is increased. Berenis [21] analyzed permanent magnet bottom-stirred swirling flow in coaxial shallow cylindrical containers. By studying the problem analytically and numerically, he found that shallow containers are more effectively stirred with a permanent coaxial magnet with a strong axial component rather than an RMF stirrer with a strong transverse part of the magnetic field.

One of the tasks of this study is to predict the operating parameters of permanent magnet machinery used in the laboratory and industry prototype for aluminum. For example, what is the maximum operating frequency of electromagnetic stirring to achieve the highest flow velocity? The best criterion for the answer is the dimensionless frequency shown in Eq. (2.34), which considers frequency, material properties, and characteristic size. In general, an optimum frequency exists, exceeding it might lead to a plateau or a reduction of, for example, flow velocity. Unfortunately, there is no single agreed value on when exactly that happens. Moffat [11] predicts maximum kinetic energy will be found around $\Omega_D = 40$ for electromagnetically stirred fluid. Priede [58] found that maximum torque on the electromagnetically levitated sphere in the uniform field is reached when $\Omega_D = 11.6$ and in the linear decaying field $\Omega_D = 27.8$. Chen [59] modeled cold crucibles and found optimum $\Omega_D = 8.7$ for maximum turbulence kinetic energy and $\Omega_D = 50$ for maximum flow velocity. This finding is very thought-provoking since there is more than five times difference in frequency for maximum velocity and maximum turbulence kinetic energy. Nikulin [60] studied induction melting numerically and found flow maximum at $\Omega_D = 7$. Most of these articles calculate dimensionless frequency with radius as the chosen length scale - the same is true in this study. For direct comparison, the values found in articles that did not use the same length scale were converted.

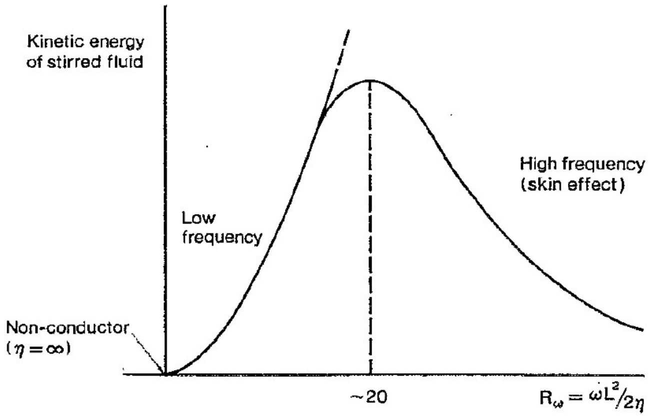

Figure 3.5: **A qualitative sketch of the change in kinetic energy for an electromagnetically stirred fluid, as a function of the dimensionless frequency Ω_D; Regular perturbation theory is applicable in the low-frequency regime, and skin-effect analysis is applicable in the high-frequency regime [11]**

4. EXPERIMENTS

Experiments are the foundation of this work, so experimental setups are introduced and described in detail in this chapter. Broadly speaking, they can be divided into experimental series with GaInSn alloy and aluminum. All measurement methods used are mentioned here for both cases. Most work is done with GaInSn alloy in a single setup adapted for a multitude of experiments. The goal and vast majority of results and discussion are found in the next chapter No. 5. A few results regarding magnetic field optimization are already discussed here since they dictated any further model design.

4.1. GaInSn experimental model

Table 4.1

Dimensions of experimental and industrial system

Type	Metal	Diameter, m	Height , m	Rotor, m	gap, m
Laboratory model	GaInSn	0.20	0.03	0.12	0.038
Industrial degassing unit	Al	0.60	0.14	0.36	0.11

A scaled experimental model for the proposed degassing unit has been built to better understand the electromagnetically created flow and validate our numerical model. The model (see Fig. 4.1) has a GaInSn reservoir designed from acrylic glass with implemented measuring holes for ultrasound Doppler velocimetry (UDV). The placement of the measuring holes is shown in Fig. 4.2. Under the liquid container, a permanent magnet rotor is placed co-axially to the vessel, and an electric motor controls it via variable-frequency drive. A permanent magnet rotor is magnetized radially (see Fig. 4.5 on page 41), and such a setup produces a magnetic field in the container as shown in Fig. 4.3. The model provides an option to circulate the liquid metal through loops or restrict the stirring in the GaInSn reservoir in order to model all possible use cases. Dimensions of the reservoir are given in Table 4.1.

Table 4.2

GaInSn and aluminum properties

Metal	$T_m, ^o C$	$\rho(l), kg/m^3$	$\sigma, S/m$	$\nu, m^2/s$	$\eta, Pa \cdot s$
GaInSn [61]	-19	6400	$3.46 \cdot 10^6$	$3.75 \cdot 10^{-7}$	$2.4 \cdot 10^{-3}$
Aluminum [62, 63]	660	2391	$4.85 \cdot 10^6$	$1.55 \cdot 10^{-6}$	$1.0..4.0 \cdot 10^{-3}$

Gallium alloy GaInSn is used as the metal for the scaled model. Its properties, together with molten aluminum's, are shown in Table 4.2. GaInSn is 2.7 times denser, has

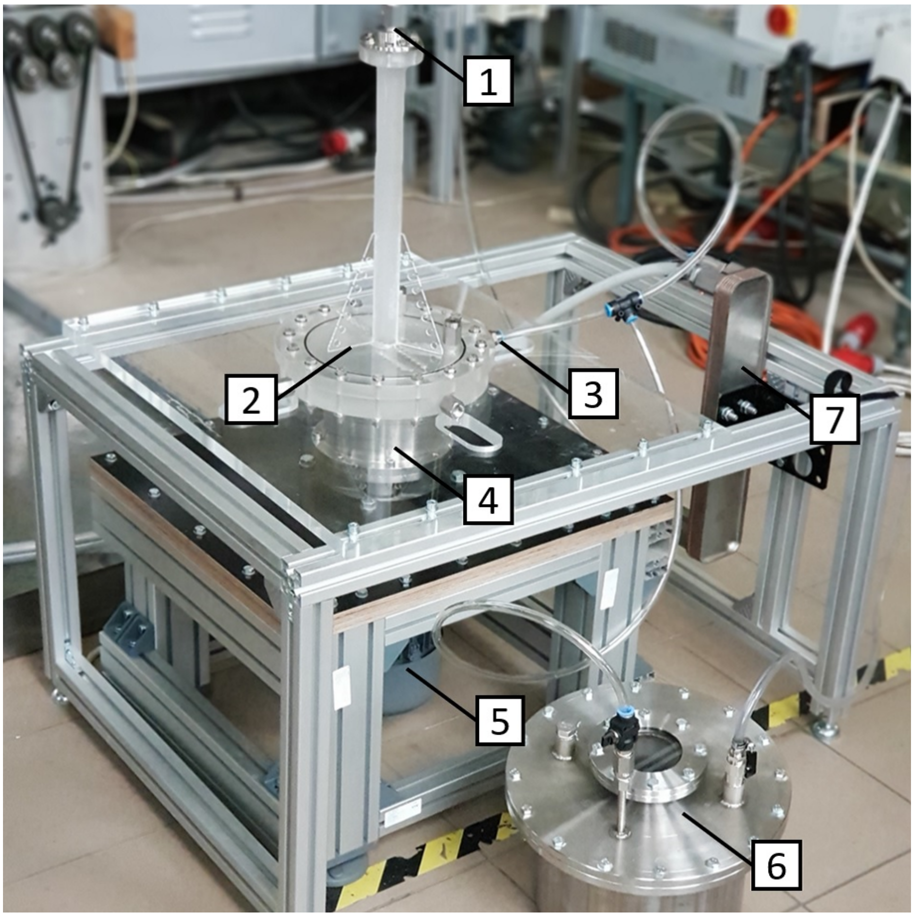

Figure 4.1: **GaInSn experimental model: 1 - inlet 2 - plexiglass vessel for GaInSn; 3 - outlet; 4 - permanent magnet rotor; 5 - electric motor; 6 - GaInSn storage; 7 - heatsink**

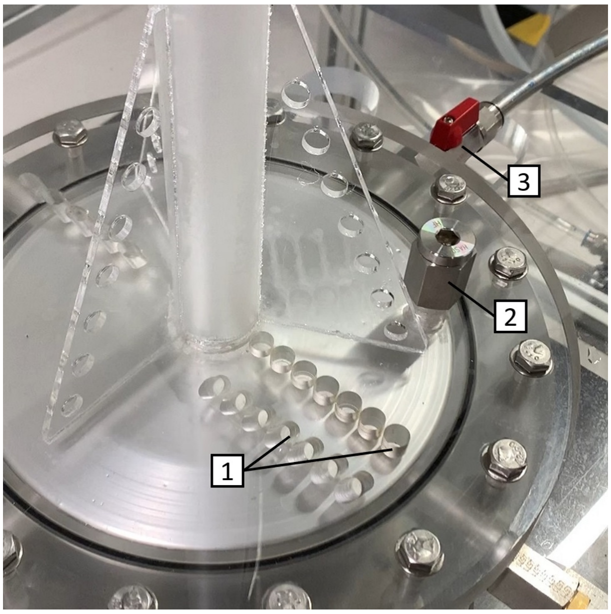

Figure 4.2: **UDV measuring holes: 1 - measuring holes for UDV; 2 - argon inlet; 3 - outlet**

about 70 % of electrical conductivity, and has about the same dynamic viscosity as typical aluminum alloy. In the case of aluminum, the properties vary with temperature and the type of alloy used. Here we describe values just above the melting temperature. Out of all properties, alloying materials most drastically impact electrical conductivity, making it worse. That happens even in low concentrations under 1 %. There can be up to a 3 times difference in electrical conductivity between some aluminum alloys compared to pure aluminum in elemental form. This is important to us because electromagnetic forces are proportional to electrical conductivity. Alloying elements can both decrease and increase viscosity. For example dynamic viscosity of pure aluminum at melting temperature is about $2 \cdot 10-3$ Pa·s but viscosity range of aluminum alloys is from $1 \cdot 10^{-3}$ Pa·s to $4 \cdot 10^{-3}$ Pa·s. The effect of alloying elements on viscosity and resistivity is visualized in the attachment (see Fig. 6.4 on page 98).

4.1.1. Optimization of magnetic field

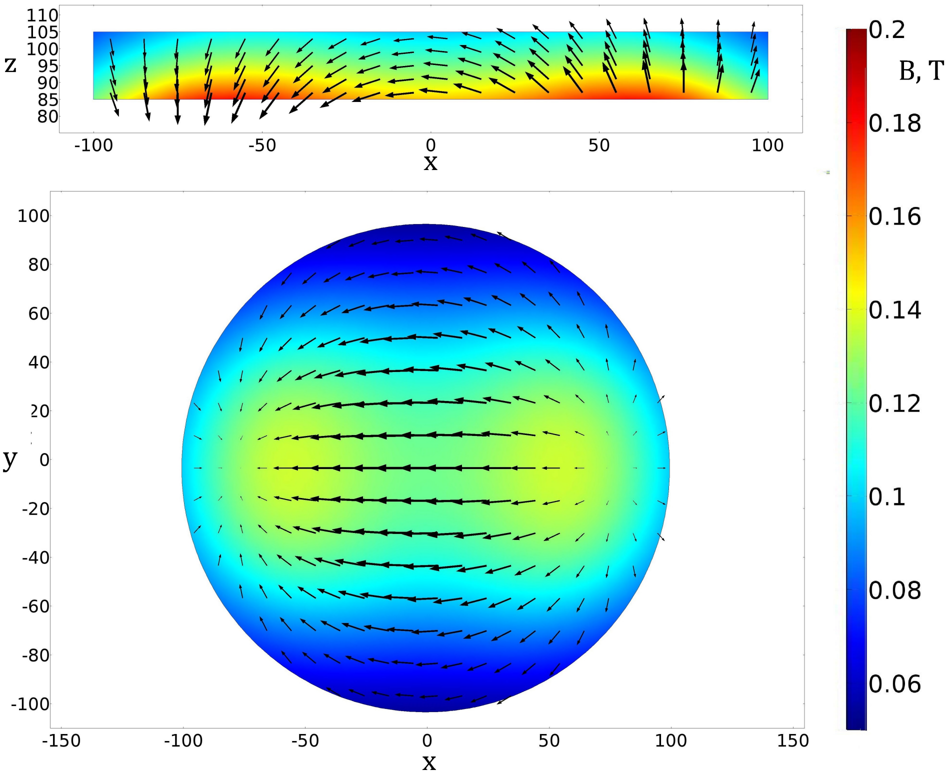

Figure 4.3: **Magnetic field in the container, xy and xz planes of the container are plotted**

The induced current $\mathbf{j}$ in metal is proportional to the rate of change of magnetic field, so by examining the Lorentz force $\mathbf{f} = \mathbf{j} \times \mathbf{B}$ we can conclude that $\mathbf{f} \sim \mathbf{B}^2$. Thus increasing the magnetic field has an enormous effect on the intensity of the induced flow. More specifically, we want to maximize the magnetic field in the vessel where the liquid metal is stirred. Straightforward solutions include positioning the magnet as close as possible to the melt and increasing its size. In practice, the minimal size of the nonmagnetic gap is limited by the furnace's geometry and the magnets' cooling constraints. Material costs of permanent magnet material constrain the size increase. A cost-effective way might be to use magnetic flux concentrators to increase field strength in the pool of liquid metal. Here it was practically carried out by adding two sectors of iron yokes to the top half of the magnetic rotor. The optimal shape of ferromagnetic sectors was found with numerical calculations by doing multiple parametric sweeps for the sector's thickness, height, and angle. The aim was to maximize the vertical component of the magnetic field in the container, and 60 degree sectors with a thickness of 2 cm and height of 6 cm were picked. Some parameters were not necessarily maxima but were chosen since increasing that parameter would bring diminishing returns.

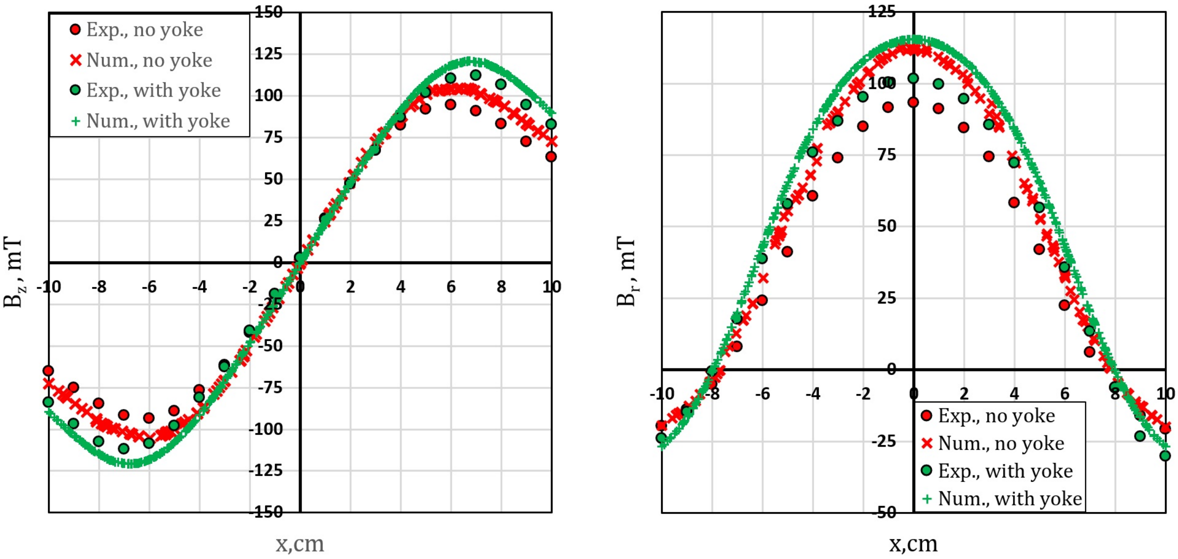

(a) **Vertical component** B_z

(b) **Radial component** B_r

Figure 4.4: **Comparison of experimentally measured and numerically calculated magnetic field in the container; Line across container at** $y = 0$

The permanent magnet rotor is magnetized radially and centered under a cylindrical metal pool. In doing so, the magnetic field inside the container is increased, especially the vertical component. A numerically calculated magnetic field in xy and xz planes is shown in Fig. 4.3, which illustrates that the radial component dominates in the center. Still, above the edges of the permanent magnet, the vertical component dominates. Cases with and without magnetic flux concentrators are compared with numerical results by analyzing the magnetic field plotted on a line across the container (see Fig. 4.4). The radial component (see Fig. 4.4b) firstly shows that numerical calculations in both cases show higher magnetic field values than the experimental measurements, and the difference between the case with iron yokes across the profile is minor (up to 5 %).

On the other hand, experimental curves show a 10-25 % increase in the radial component of the magnetic field. The vertical component (see Fig. 4.4a) also shows higher values in the numerical calculation; however, the ratio between cases with and without iron yokes is similar. It can be concluded that iron yokes, as magnetic flux concentrates, yield up to a 25 % increase in the magnetic field depending on the position and which component we analyze.

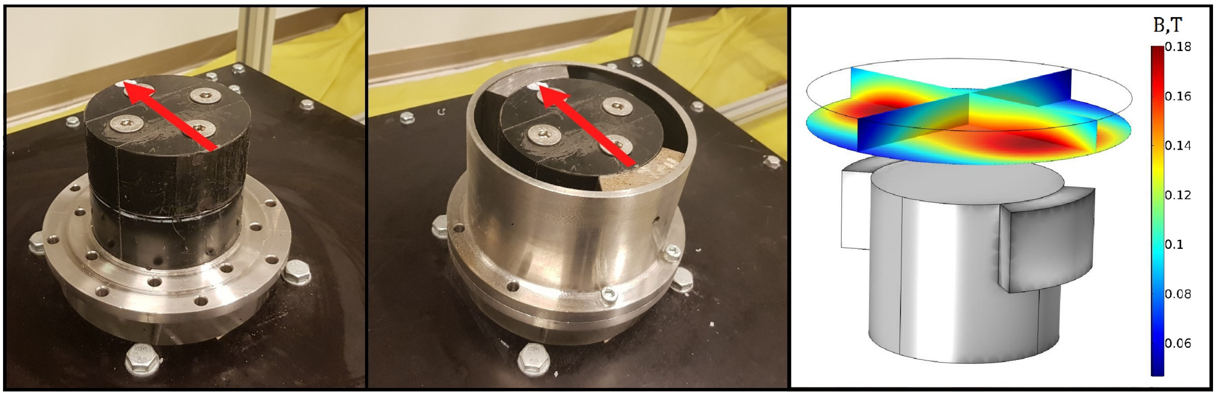

Figure 4.5: **From left: a permanent magnet rotor, a rotor with iron yokes, and a liquid metal container position relative to the magnet are shown; Magnet magnetization is indicated with an arrow**

If we set a fixed magnetic field goal, it is possible to save magnetic material using a smaller magnet with ferromagnetic yokes. For example, let's compare this 120 mm magnet with yokes to a larger cylindrical magnet without yokes. One can find an equivalent diameter that produces the same vertical magnetic field in the container. It was found that for a 120 mm magnet with yokes, an equivalent magnet would have to be with 140 ± 1 mm diameter. Thus it is possible to save 26.5 ± 1 % of magnetic material with magnetic flux concentrators.

4.1.2. Inert gas injection

One of the features that dictate the bubble size of the injected gas in a liquid is the diameter of the injection orifice [44]. Broadly speaking, smaller bubbles can be produced by a smaller injection orifice. The industrial solution is using either porous material or material with small (sub-millimeter) holes drilled into it. Most likely, the chosen injection method in the aluminum industry will be through a porous ceramic plug. Practically it means injection will happen through hundreds of tiny pores from a flat surface measuring roughly 10 cm^2. An example of a small porous plug is shown in the attachment, in Fig. 6.8 on page 101.

In this experiment, we iterated the nozzle design and reached a solution to use a 0.4 mm medical needle with an adapter shown in Fig. 4.6b so it could be connected to a standard gas pipe. Argon is injected into the melt via an inlet shown in Fig. 4.6a. The injection port is located close to the outer wall of the cylinder since the bubbles in this system move toward the center. Here it is also essential that the injection tip is not within the wall but protrudes into the metal to achieve maximum shear forces as mentioned in previous sections.

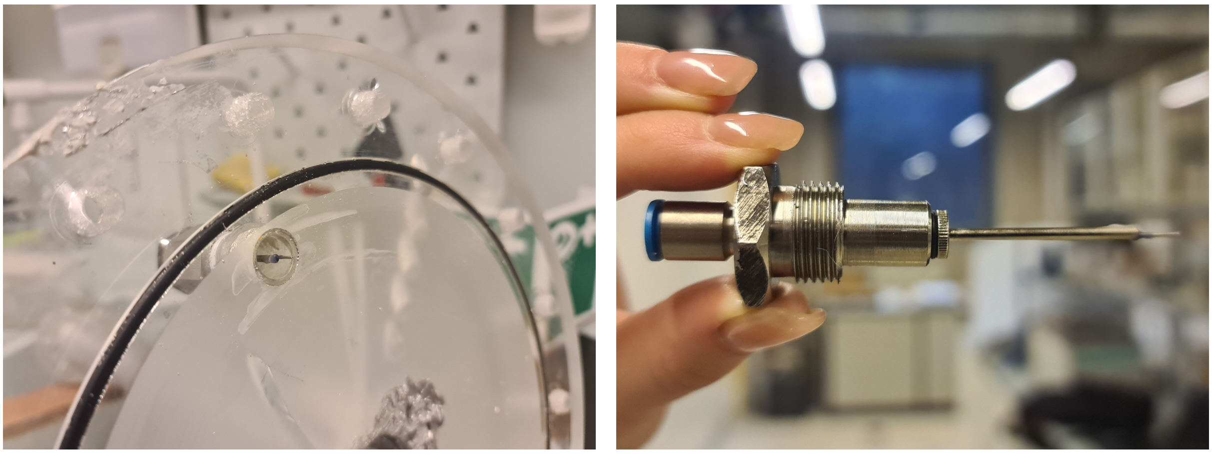

(a) **Position of the needle** *(b)* **Injection adapter with the needle**

Figure 4.6: **Second iteration of the gas injection system: A 0.4 mm needle is used to inject argon bubbles into the melt**

The path and bubbles can be seen through the acrylic wall if the metal does not wet the surface, thus, after each experiment system was cleaned. With rare exceptions, both pressure and UDV measurements (described in next subsection) were performed without the bubble injection.

4.2. Experimental measuring techniques

Multiple parameters are measured to characterize the GaInSn experimental model, including flow velocity, developed pressure, flow rate, induced power, bubble size, and bubble dynamics. In general, we want to quantify how hydrodynamics are affected by variables such as magnet rotational frequency, the geometry of the liquid metal vessel, and rotating permanent magnet machinery. Multiple experimental techniques are used to do that, described in the following subsections.

4.2.1. Velocimetry

Velocity measurements in liquid metals are challenging due to the opacity and high temperature of liquid metals. One of the few methods to measure flow velocity in liquid metal up to 150 C is pulsed Doppler ultrasound velocimetry [64]. Using the device shown in Fig. 4.7, one can measure flow velocity projection on the axis of the probe in a non-intrusive way. To reiterate, the device measures the velocity component parallel to the probe. Velocity is obtained in multiple depths, forming a profile that consists of approx. 100 points depending on settings. The principle of operation of this method is explained in the attachment (see Fig. 6.3 on page 96).

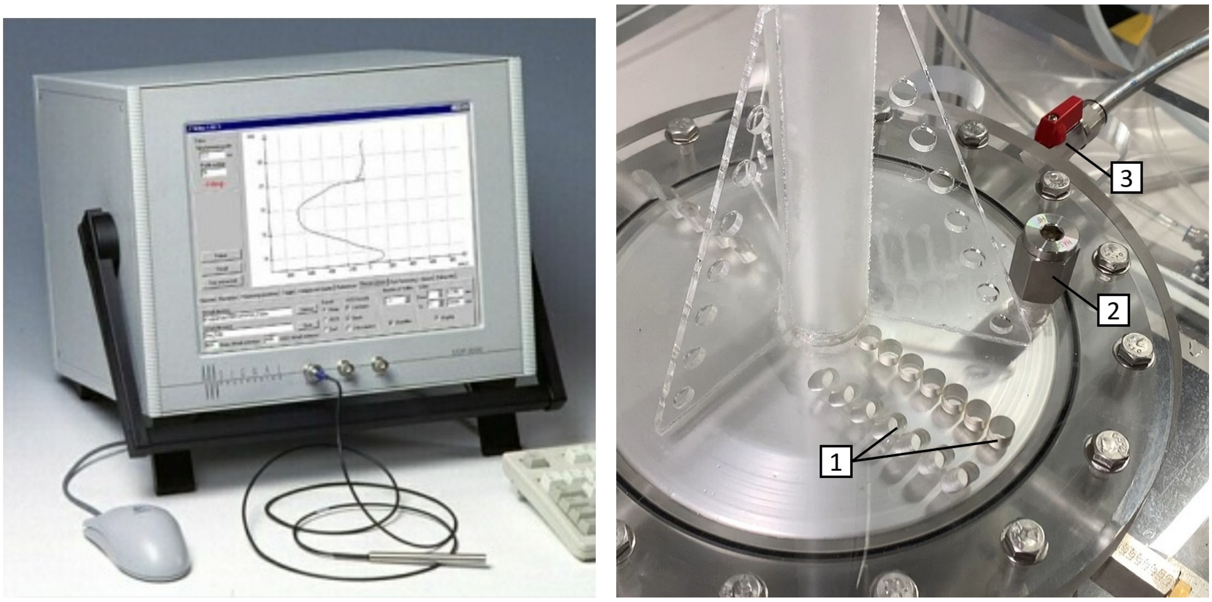

(a) **DOP2000** *(b)* **Measuring positions**

Figure 4.7: **Ultrasound Doppler anemometer**

In following experiments 2 MHz emitting probe is used with pulse repetition frequency $f_{prf} = 8000..13513$ Hz which allows measurements in depth $x_{max} = 10..17\ cm$ and of maximum velocity $v_{max} = 2.7..4.6$ m/s. Each velocity measurement in our measurement profile is done within a finite volume. It can be approximated as a cylinder with a base made of a cross-section of the ultrasonic beam (5 mm diameter), and height is spatial accuracy of 2.5 mm (spatial accuracy is obtained by dividing the maximum measuring depth by the number of gates). Time-averaged velocity is obtained by averaging 55 seconds of flow measurements. The uncertainty of measurement angle and effects of signal noise for the GaInSn experimental model is estimated to be 5 %. In general, an echo signal can come from many different depths, corresponding to echoes from previously emitted signals. The presence of several acoustic interfaces also causes several reflections, which can cause a false determination of the target depth. Thus thorough analysis of the beam path is examined to understand which depth of received signal is a reflection and to be dismissed. Fig. 4.7b shows a cylindrical vessel designed to be compatible with UDV velocimetry. The wall material is acrylic glass which has similar enough acoustic properties (sound velocity and acoustic impedance) to liquid metal. Firstly, when materials are compatible, less energy of acoustic waves is reflected before entering the metal. Secondly, if an acoustic beam moves through different mediums and forms an angle with an interface that is non-perpendicular, there will be a refraction of the beam. Therefore, having a similar sound velocity for measuring liquid and wall is beneficial. Here the azimuthal flow is measured at measuring holes drilled at a 45-degree angle. Measuring positions are spaced radially at r = 36; 47; 58; 69, and 80 mm.

4.2.2. Hydrostatic pressure

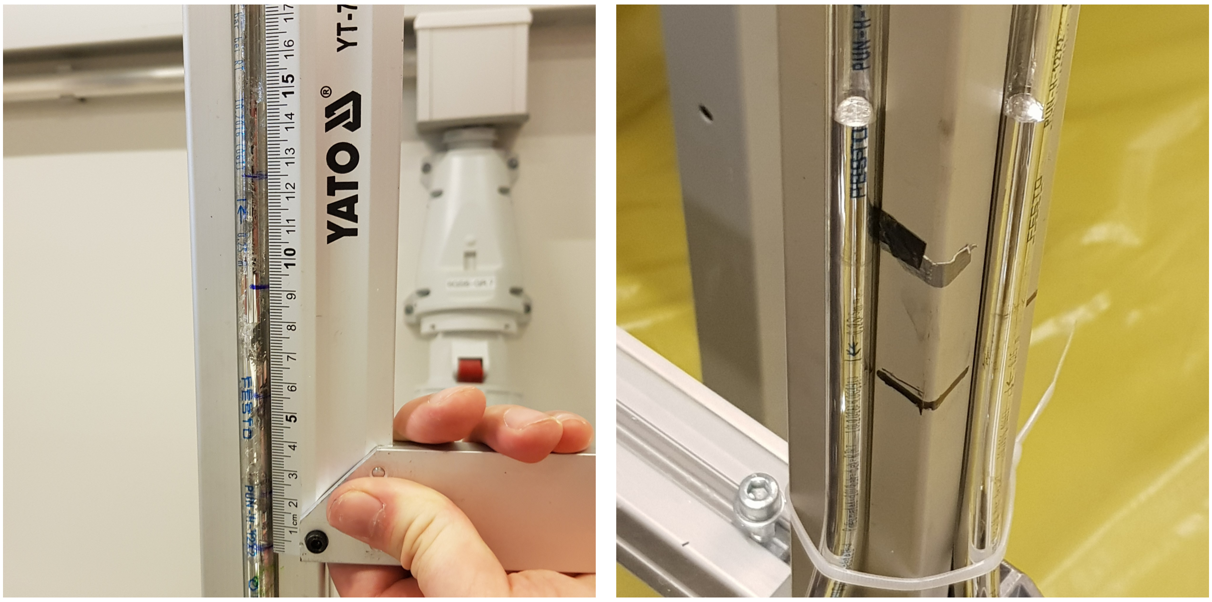

(a) **GaInSn wetting** *(b)* **GaInSn not wetting**

Figure 4.8: **Measuring of liquid metal column caused by developed pressure of experimental device**

Pressure measurements in the outlet are taken by measuring the height of the liquid metal column with an accuracy of 2 mm (see Fig. 4.8). The developed pressure is equal to $\rho_{GaInSn} g \Delta h$ where the height difference is measured relative to the reference level when there is no stirring. For reference, 0.1 atm pressure produces 160 mm pressure head in GaInSn, yielding 1.2 % accuracy at this specific pressure. There were also pressure oscillations with a period measured in seconds and an amplitude of a couple of millimeters, limiting the accuracy. Since GaInSn, by default, wet surfaces 5 % hydrochloric acid is added in a thin layer, so the surface of the metal is visible from the side (see Fig. 4.8b for the improvement). The most significant uncertainty is caused by the nonmagnetic gap between the rotor and the melt. Experimental accuracy is only 3 %, which is estimated to have a 6 % uncertainty for flow velocity.

4.2.3. Flow rate and power

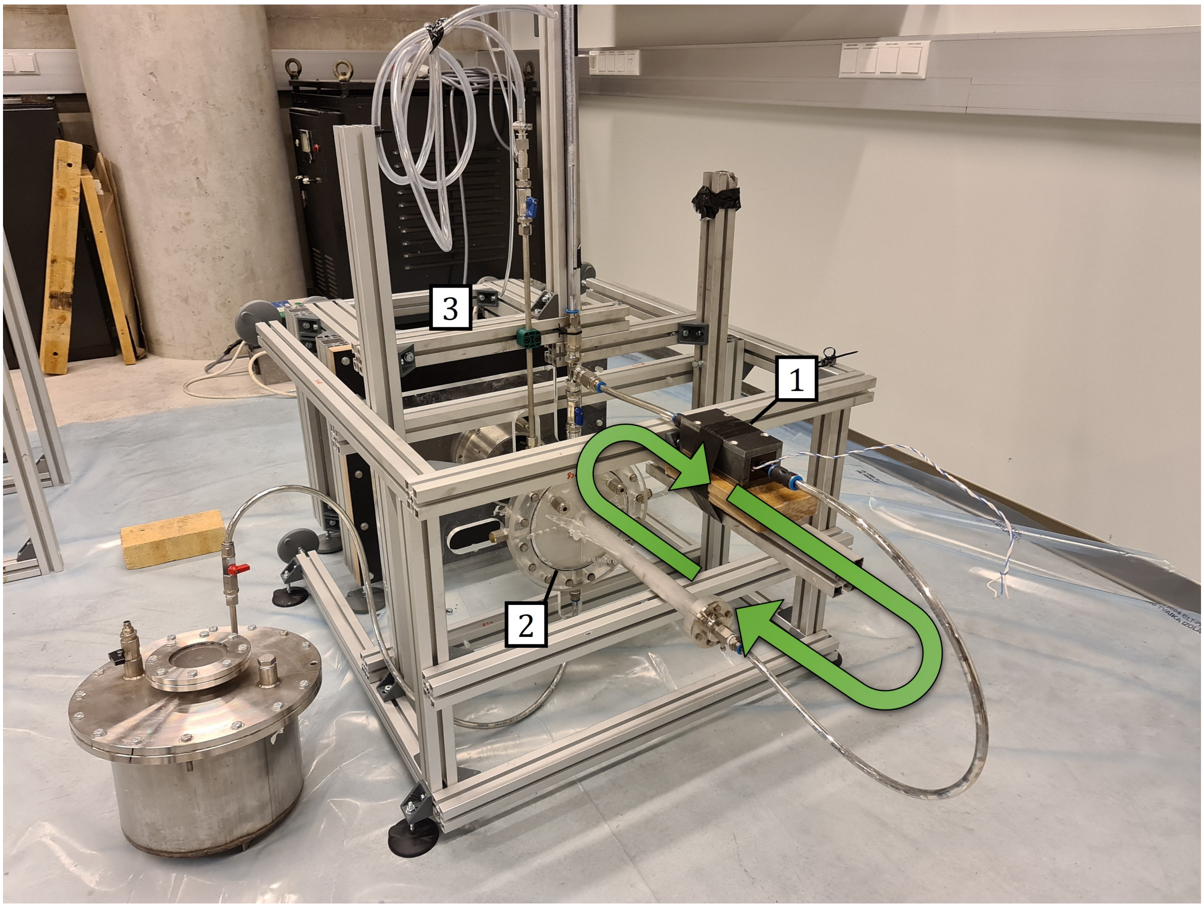

Figure 4.9: **Experimental setup and orientation in flow rate measurements. The green arrow indicates the loop of circulation. 1 - Conduction flow meter where the measurements were taken; 2 - cylindrical vessel with most metal volume; 3 - permanent magnet machine driving the flow**

In a pipe flow, the volumetric flow rate Q and the developed pressure p relate to the hydraulic power P_H as shown in Eq. (4.1). Thus pressure and flow rate measurements can give insight into the hydraulic power of the system.

$$P_H \ [W] = Q \ [m^3/s] \cdot p \ [J/m^3] \tag{4.1}$$

Flow rate measurements here are taken with a custom-built conduction flow meter. The principle of its operation is the following - a flow of conductive fluid in a duct that passes through a homogeneous magnetic field creates an electric potential that can be measured. Flow rate is calculated from flow velocity, it can be correlated to velocity since we know the inner cross-section of the pipe. However, there might be some nonlinear effects in the planned measurement range. Thus, before using the flow meter, it is calibrated with a known flow rate of liquid metal. The experiment flow meter measures the flow rate of the circuit shown in green in Fig. 4.9.

Another experimental approach for power measurements in the metal is measuring its temperature and its rise when different magnetic field frequencies are applied. If the mass together with specific heat capacity is known, and the system is thermally insulated, we can calculate the dissipated energy with Eq. (4.2):

$$m \cdot c_p \cdot \Delta T = P \cdot t \tag{4.2}$$

where c_p is the specific heat capacity of GaInSn, m is the mass of GaInSn being stirred, temperature rise over time t and P is the total power induced in the liquid metal. Measurements are done with a 3 mm K-type thermocouple and saved in the computer every 0.1 second trough *Data Translation DT9828* logger. The thermocouple was submerged directly in the alloy, so when the magnet was operating and inducing the currents, thermocouple readings were affected, as shown in Fig. 6.7 (see in the attachment on page 100). This problem was avoided by doing the measurements when the machine was off. Each frequency was measured sequentially and exposed to rotating magnetic field for one minute and then left to cool for one minute. The cooldown was performed to see and adjust for conductive heat losses. Even though acrylic glass is not a good heat conductor relative to liquid metal, significant enough temperature drops were observed. Thus a correction was introduced:

$$m \cdot c \cdot ((T_2 - T_1) + (T_3 - T_2)) = P \cdot t \tag{4.3}$$

where T_1 - temperature at beginning, T_2 - temperature after one minute of stirring, T_3 - temperature after one minute of cooling. This correction adds back the lost energy during the one minute of stirring assuming the energy loss rate is the same during the one minute of cooling. This is not entirely true, however the corrected result is still definitely closer to the truth than the uncorrected version.

In numerical model the induced power can be calculated in the following way:

$$P = \iiint_V \frac{j^2}{\sigma} dV \tag{4.4}$$

where V is the volume of the liquid metal in the active part of the experiment. Similarly, ϵ (turbulence kinetic energy dissipation rate) can be integrated over volume and multiplied by density to get the power figure by analyzing the turbulent flow.

4.2.4. Image acquisition of bubbles in a turbulent flow

Bubble dispersion by flow is central to this work. Overall filming metal surfaces poses some unique challenges. When the surface is very clean it becomes a mirror and such surface is a lot more harder to capture on film than matte one due to reflections. When surface is calm one sees long range reflection as from a flat mirror. When surface is agitated there are distorted long range reflections and reflections that have already scattered from surface more than once. Having an oxide layer (and GaInSn does form it quickly) makes surfaces matte silver. However too thick of oxide layer creates new problems by acting as cover for everything that is happening on the free surface of metal. This experimental model allows us to visually detect the bubbles by viewing the top surface where the gas bubbles are pressed against the transparent lid. Sketch of the experiment and the actual setup are shown in Fig. 4.10. In this case, surface deformations are not a problem since there is a layer of acrylic glass acting as a barrier. Despite being in argon atmosphere, oxides were still formed, but they were collected in central column away from the area being imaged. However, the acrylic glass lid did pose a new problem of wetting the surface and covering it with opaque layer of oxides. This did not happen immediately, but between the experiment series devices had to be drained, disassembled and the surface cleaned. Image acquisition is done by a *Lumix S5* digital camera with shutter speed set to 1/6400-th s to ensure that the bubbles moving with speed of 3 m/s are still sharp in the photos. Due to low exposure time extra lighting was added to keep the image noise minimal. The used field of view and resolution corresponds to

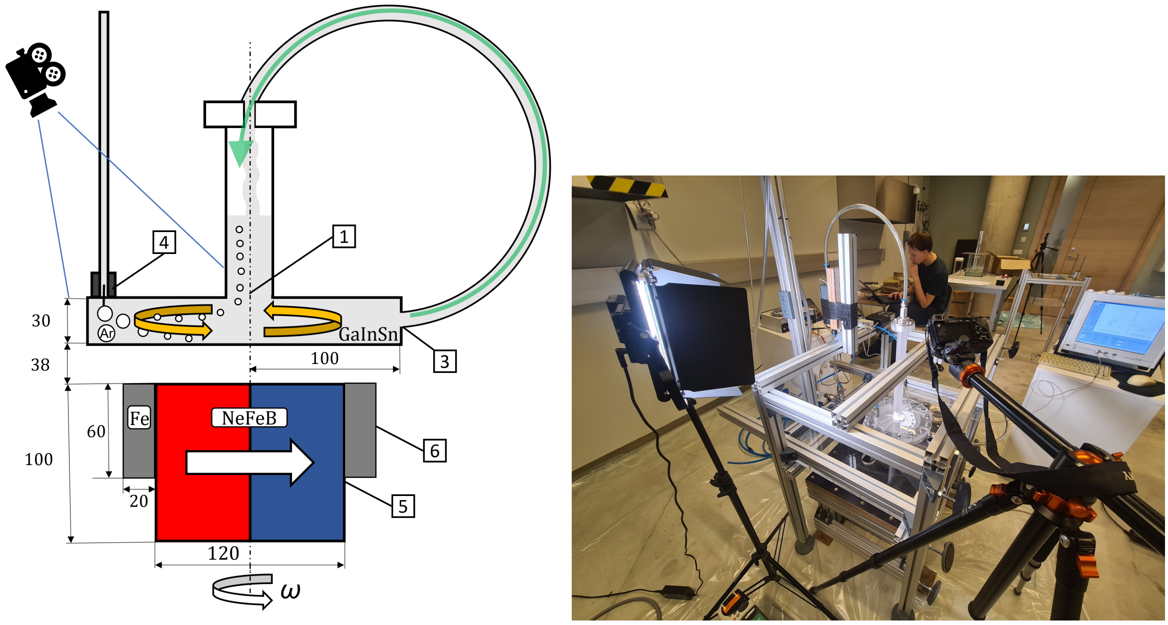

(a) **Experiment sketch** *(b)* **Experiment picture**

Figure 4.10: **Bubble imaging experiment using high frame rate camera**

15.7 pixels per 1 mm or 0.064 mm (assuming ideal conditions). Images were processed using *ImageJ Fiji* open source software [65] where bubble outline was manually traced and the area calculated. Using the area, the diameter of the bubble is calculated assuming a circular shape. Individually the opposite is true - various shapes and sizes are observed, however this is compensated by averaging at least 30 samples of bubbles for each studied frequency. Here it must be noted that we see the bubbles that are only on the surface of the metal. Also the visible bubble shape is deformed. In a stationary case when the bubble is pressed to the top of the container it is flattened. The shape of the droplet is an equilibrium of gravitational force, Archimedes force and surface tension. The result is that the maximum height of the bubble is affected and is comparable to capillary length - in this case $\lambda_c = \sqrt{\frac{\gamma}{\Delta\rho g}} = 3.1\ mm$. Another consideration using this method to film a bubble in a rotating system is the change of pressure between gas inlet and outlet. The volume of individual bubble is inversely proportional to the pressure according to ideal gas law. Since $r\ V^{1/3}$ impact on mean bubble size is reduced but still applicable and thus caution should be given to where bubble image is taken within the system.

4.2.5. Hydrogen content

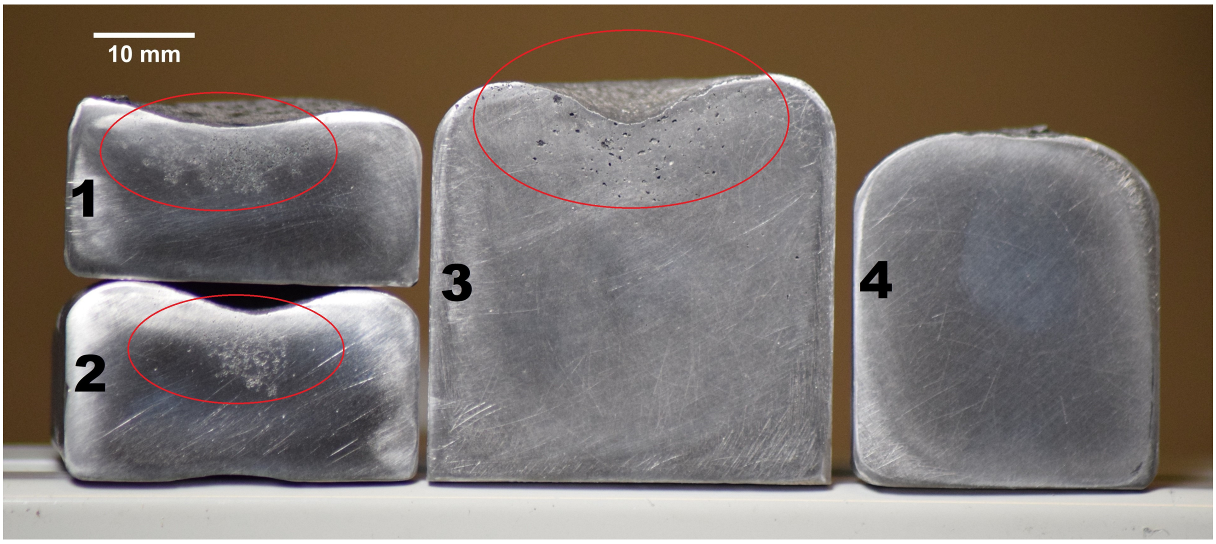

Figure 4.11: **Cross section of A356 aluminum samples under different molds and solidification conditions: 1;2 - are crystallized in graphite mold from bottom and sides, 3 - crystallized rapidly in copper mold from bottom and sides, 4 crystallized rapidly from bottom; Red circles highlight solidification defects**

Hydrogen content measuring techniques can be categorized by the stage they are used at - hydrogen content can be measured in molten aluminum prior the casting or after the crystallization in the solid state [14]. The most simple indirect measurement of hydrogen content is its density measurements. Excess hydrogen causes porosity (see

Fig. 1.1 on page 12) but to detect it accurately density must be calculated with accuracy of 0.1 %. The same goes for a situation where certain target hydrogen concentration must be reached - the resulting density for the alloy must be defined with three significant digit accuracy. All in all, absolute measurements of hydrogen content are challenging.

Cross sections of different aluminum samples show pores in solidified aluminum (see Fig. 4.11). To quantify porosity, the pores and their area can be counted. One must be careful in distinguishing the defects not to mistaken them with regular casting defect (like shrinkage). Regardless it is seen that these defects form in regions which solidify the last. Ergo, when measuring hydrogen content by measuring the density of aluminum, the choice of sample location from ingot becomes crucial. To ensure the best results, the sample crystallization can be carried out in reduced pressure to maximize the pore size and count. This reduced pressure test (RPT) method was employed on some samples.

4.3. Experiments in aluminum

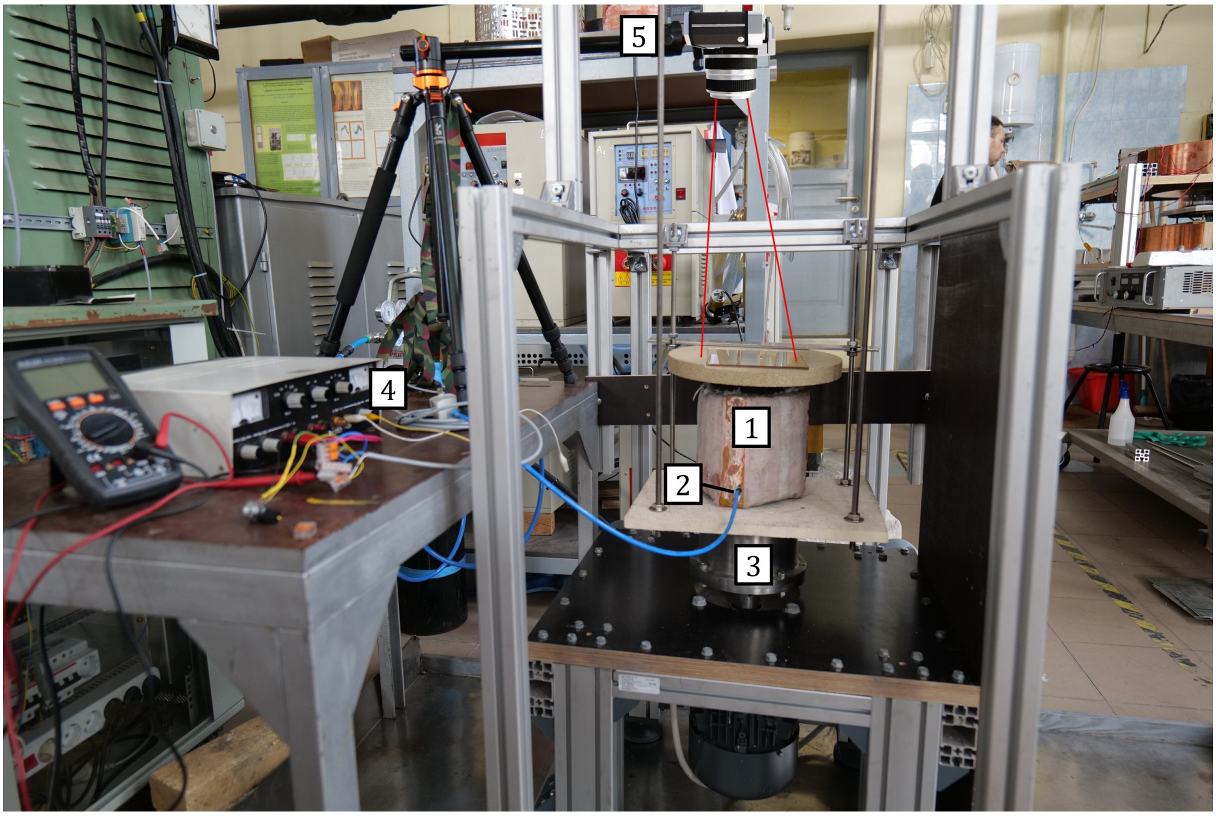

Figure 4.12: **Laboratory aluminum degassing experiment. 1 - Inductor and crucible holding 1.8 kg aluminum; 2 - argon gas inlet at the bottom; 3 - digital camera position; 4 - mass flow controller (MFC) for argon; 5 - digital camera position**

Experiments in aluminum were carried out on two scales. In the laboratory scale, we tested gas injection and bubble collapse with the experimental setup shown in Fig. 4.12. In industrial conditions, we experimented with a full-scale prototype with 800 kg aluminum shown in Fig. 4.13.

The objective of the laboratory scale setup was to familiarize ourselves with how to work with liquid aluminum experimentally. Firstly, the gas injection was tested to see how the bubbles behave in aluminum while in similar flows as tested with the GaInSn experiment. Secondly, small-scale experiments were necessary to test aluminum sample taking and post-processing.

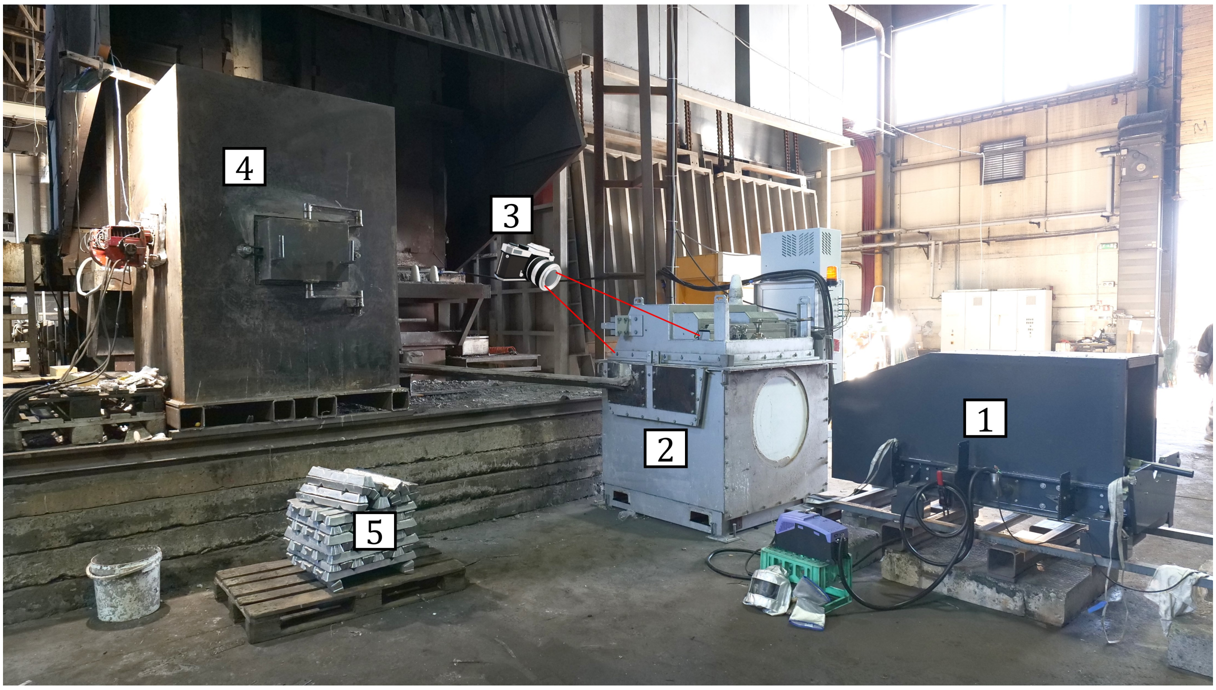

Figure 4.13: **Industrial degassing prototype experiment: 1 - permanent magnet stirrer (positioned away in stand-by regime while aluminum is melting); 2 - aluminum degassing unit; 3 - digital camera position; 4 aluminum melting furnace; 5 - aluminum alloy A356**

In the industrial experiment, different challenges arose. Firstly, the rotating permanent magnet machine had to be built on a larger scale, which posed new engineering challenges which were not present in laboratory stirrers. The central part of the machine is a 200 kg permanent magnet consisting of 216 individual parts, which have to be assembled in-house. Specific consideration has to be given to the extremely strong stray magnetic field. E.g., ferromagnetic components are subject to forces thus, they shall be avoided when possible. Additionally, on a larger scale, electromagnetic induction starts heating the surrounding electrically conductive materials, which must be considered for elements around the permanent magnet.

The laboratory-scale aluminum model uses the same permanent magnet machine as in the GaInSn model. However, the crucible holding metal had to be redesigned for aluminum. Here, a cross-section (see Fig. 4.14) shows the graphite crucible being heated by induction heating. Aluminum fills the crucible to half, but when a strong tornado-like flow is created, the metal reaches the top of the container, which is partly sealed for that exact reason.

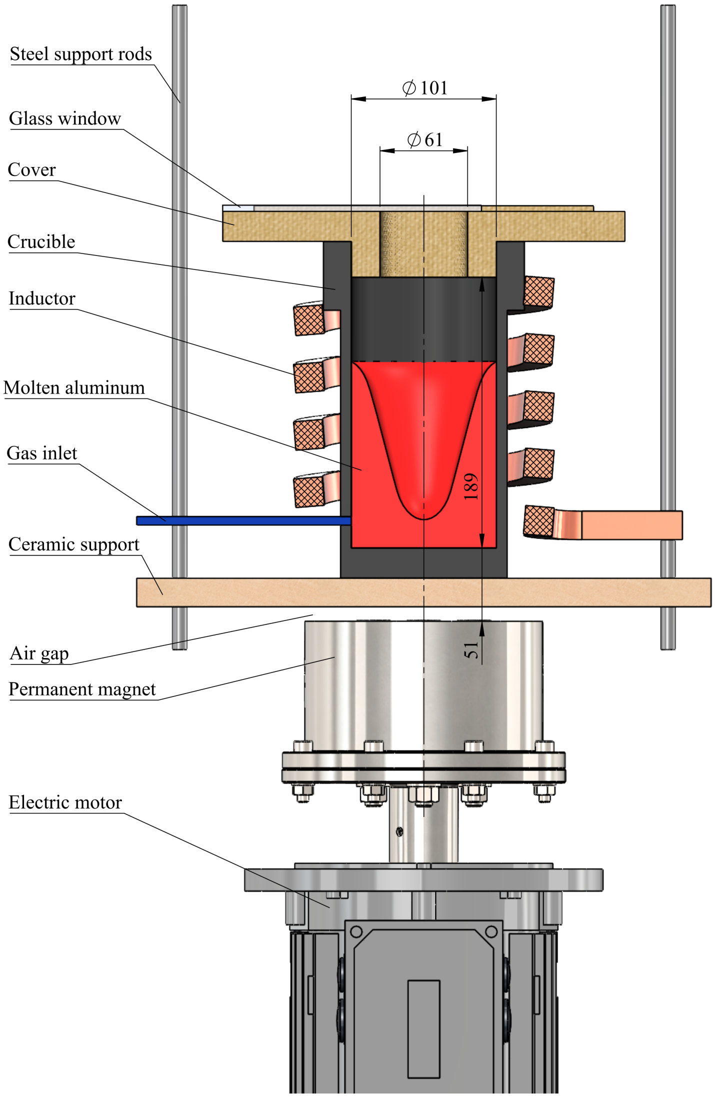

Figure 4.14: **Cross section of laboratory aluminum degassing experiment**

The simplest order of magnitude estimate can be done to balance electromagnetic and inertial forces. From there, the velocity scale is expressed in Eq. 4.5 where L is the characteristic length, B - the magnetic field (mean value is 0.1 T), $\omega = 2\pi f$ - the angular frequency and σ is the electrical conductivity. At $f = 19.5$ Hz the expected velocity is around 1.7 m/s. When scaled to industrial size and aluminum properties, velocity v is expected to rise due to higher electrical conductivity, characteristic size, and lower density.

$$\frac{1}{2}\sigma\omega B^2 L = \rho\frac{v^2}{L} \Rightarrow v = \frac{\sigma\omega B^2 L^2}{2\rho} \tag{4.5}$$

5. RESULTS AND DISCUSSION

In this section, the main results of the thesis are presented. Metal flow is characterized by analyzing velocity, pressure, flow rate, and power which all are obtained with GaInSn experimental model. Most measurements are also presented together with numerically modeled flow results done by the team's Ph.D. student Didzis Berenis as part of the project. Comparison to numerics is essential as in later parts we analyze TKE dissipation rate, which is the best predictor of bubble size, but it can not be measured experimentally in liquid metals. For that, we only rely on provided results by modeling, which, in a sense, are validated by experimental measurements we can obtain (e.g., velocity and pressure). Gas injection experiments in GaInSn gave insight into bubble size distribution, a rare, if not unique, finding in liquid metal. Aluminum experiments, by nature, provide fewer measurements and do more of a demonstration role. Yet they are vital because they test difficult-to-predict problems like a gas injection. Lastly, dimensionless analysis is done as a part of the technology scaling process, where the main dimensionless numbers are examined, and predictions about the industrial-sized system are made.

Velocity measurements were possible for azimuthal flow up to 3 m/s, which allowed us to measure flow in the applied frequency range of 2-20 Hz. Together with pressure measurements, they formed the basis of results used to validate the numerical model. Power measurements in turn produced some inconclusive results. The discrepancy between numerical and experimental measurements was more significant than for pressure and velocity. Solid aluminum cross-sections also proved to be more difficult than anticipated because of inconclusive results omitted in this work. Nevertheless, the bubble size measurements worked out well.

5.1. UDV flow velocity measurements

Liquid metal velocity as a function of permanent magnet rotation frequency is examined in three different radial positions, as seen in Fig. 5.1. Data shows the radial velocity component, which is time-averaged over one minute. It is measured at a level of half height of the liquid metal container. Again, curves of numerical calculations show larger velocities than the respective experimental measurements. Overall velocities in the range of 2.0 to 2.8 m/s are reached at the 19.2 Hz rotational frequency of the permanent magnet rotor. Considering GaInSn physical properties (see table 4.1), it corresponds to a fully turbulent flow with $Re = 5 \cdot 10^5$. Higher rotational frequencies are not measured due to limitations of the UDV measurement system in which further measurements were not

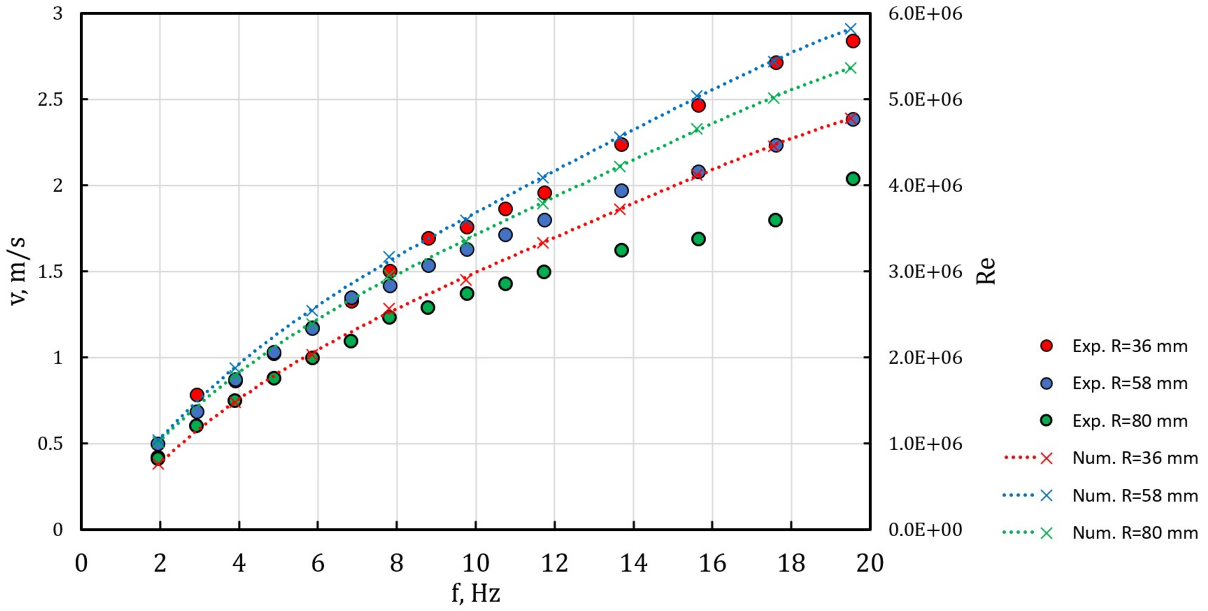

Figure 5.1: **Time averaged velocity as a function of the rotational frequency of the magnet at different radial positions**

convincing. However, frequencies up to 57.6 Hz were applied in bubble refinement experiments. In this case, the limiting factors are the slip of the magnetic field and the skin effect, which impose a maximum operating frequency. In subsection 3.3 it was discussed what is the optimal dimensionless frequency, see Eq. (2.34) for achieving the highest flow velocity. Table 5.1 shows the optimum values found in literature and how this experiment compares to them.

Table 5.1
Optimal dimensionless frequency parameter by different authors and values reached at GaInSn experiment

Author	Problem	Ω_D
Moffat [11]	General	40
Priede [58]	Levitating sphere	11.6 and 27.8
Chen [59]	Induction furnace	50
Nikulin [60]	Induction furnace	7
This work, $f = 19.6Hz$	GaInSn exp.	5
This work, $f = 57.6Hz$	GaInSn exp.	15

It is predicted that the pressure and velocity would rise further with frequency increase since the maximum dimensionless frequency reached was $\Omega_D = 5$. In bubble injection experiments discussed later, higher magnetic field frequencies were applied, which allowed us to reach $\Omega_D = 15$. The same criteria directly dictate that the maximum operating frequency in the proposed industrial degassing unit subsequently determines the maximum flow intensity.

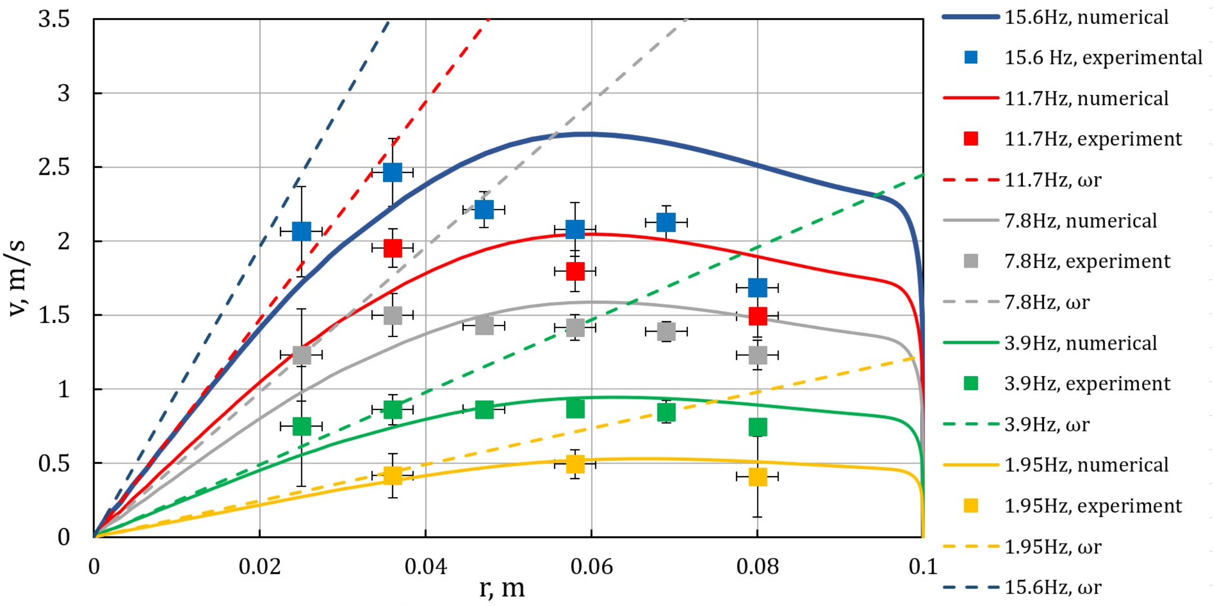

Figure 5.2: **Flow profiles at different magnet rotation frequencies: lines represent numerical calculations, squares are experimental measurements and dashed lines are ωr - velocity of the magnetic field at a given radius; The vertical error bar is one standard deviation of flow velocity, horizontal error bars indicate the width over which the velocity is averaged**

Tangential velocity in multiple radial positions is presented in Fig. 5.2, comparing magnetic field velocity with experimental and numerical measurements. Firstly, the maximum velocity in numerical calculations is observed at radial position $R = 58$ mm, while in the experiment, it is in position $R = 38$ mm. At first, it seems counter-intuitive since the velocity of the traveling magnetic field is proportional to radius $v = \omega R$, so a larger velocity is expected near the outer wall. Just as unexpected is that in the cases of low rotational frequency in the region closer to the center, the fluid moves as fast as the magnetic field. These findings can be explained by the radial flow's inward transfer of angular momentum.

The numerical model shows that there are zones with significant radial velocity. In some areas, the secondary flow can have up to 1/3 of the magnitude of the primary flow (see Fig. 5.3). Even though time-averaged force density is highly inhomogeneous across the z coordinate, exploring the azimuthal velocity, it has the same magnitude across the entire height with an even slightly higher maximum near the top as shown in Fig. 5.4. Similarly, the magnitude of radial flow is slightly higher near the top wall even though force distribution decays rapidly with the distance to the magnet, which is positioned under the liquid metal container. The Taylor-Proudman theorem explains this stabilizing mechanism, which applies to rotating flows with high angular velocity.

As expected, the azimuthal flow profiles show higher velocities with higher stirring frequencies. Qualitatively, the only minor changes are the peaks in the rate near the top

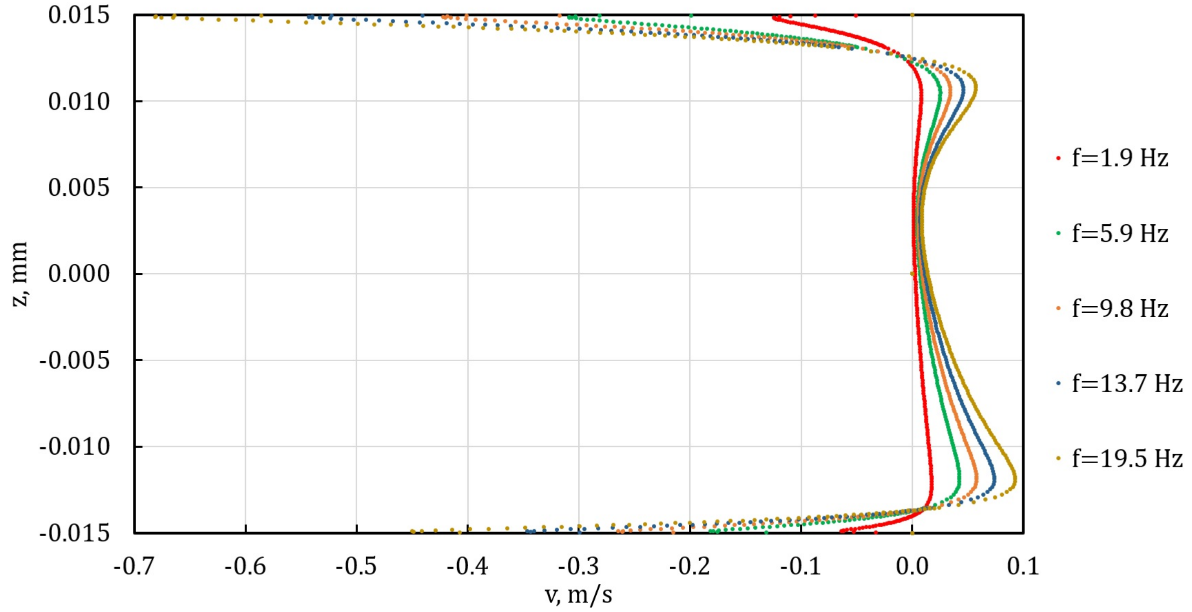

Figure 5.3: **Numerically calculated radial velocity variation as a function of container height; The rotating permanent magnet is positioned below, the radial position is** $R = 58mm$

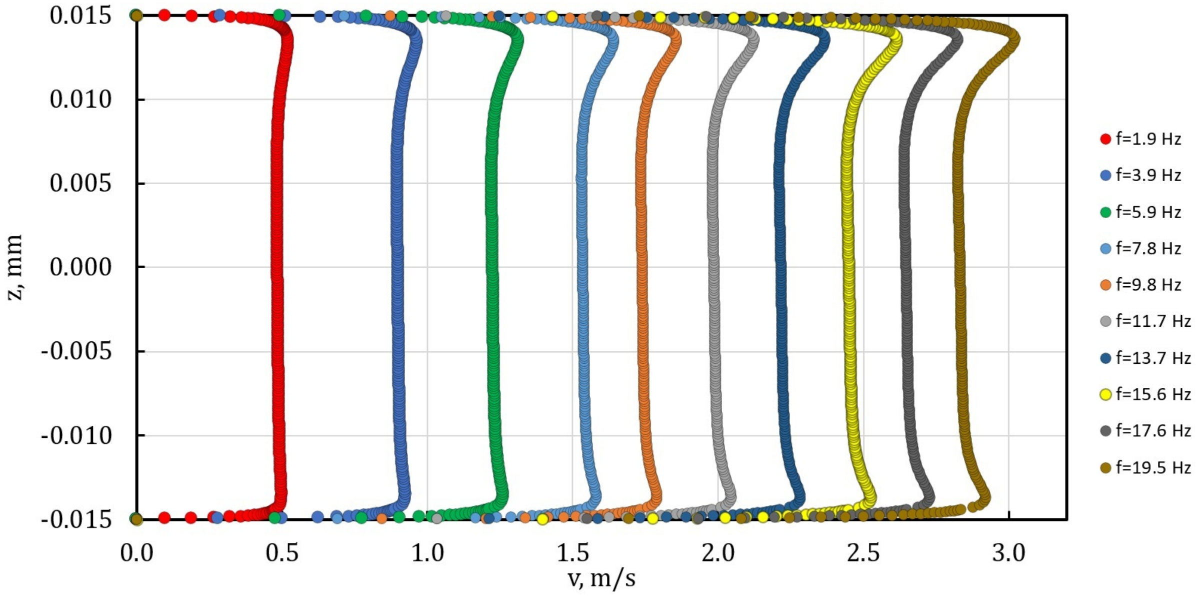

Figure 5.4: **Numerically calculated azimuthal velocity variation as a function of container height; The rotating permanent magnet is positioned below, the radial position is** $R = 58mm$

and the bottom walls. They are more pronounced if we normalize the profile with respect to mean or maximum azimuthal flow.

5.2. Hydrostatic pressure measurements

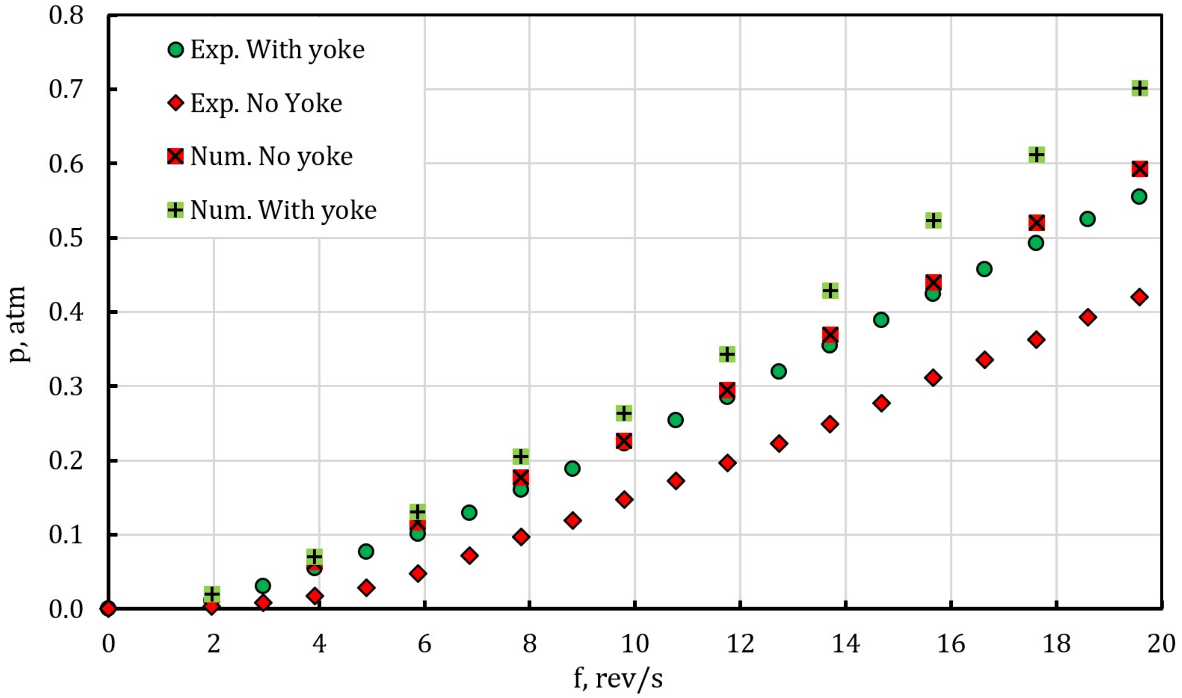

Figure 5.5: **Pressure in the outlet as a function of magnet rotation speed; No flow rate**

The first integral parameter measured in the model is the pressure in a perpendicular outlet of the GaInSn vessel. Both pressure and velocity are measured at various magnetic field rotation frequencies. Since it essentially is a dipole field, its rotational frequency is the same as a permanent magnet's. In Fig. 5.5, cases with and without yokes are compared experimentally and numerically. It is shown experimentally that pressure with the yoke is 32 % higher at the fastest of the tested configurations and the difference in numerical calculations is 22 %. The numerical model produces higher pressure in both cases. However, the curves have similar slopes when compared to the experiment. An overall pressure head of 884 mm GaInSn (or 0.55 atm) is a good result because when the degassing unit is up-scaled, it would be able to lift the aluminum multiple meters if the device is also used as a pump for molten aluminum transport.

Experimental pressure measurements and velocity measurements can be compared by integrating angular velocity across radius according to Eq. 5.1

$$p = \int_0^R \rho \omega^2 r dr \tag{5.1}$$

where $\omega = v/r$. There are seven measurements across the radius from which ω is interpolated to first order and then integrated. Graphically this is visualized in Fig. 5.6 where the area under curves is equal to the integrated value. It is possible to determine which radial positions have the greatest impact on total pressure in this system where angular velocity is not constant along the radius. For this calculation, it is assumed that there is only tangential flow. This approach allows us to cross-check experimental measuring systems. As shown in table 5.2, result values are 20 % higher than the direct measurements but are in line with numerical model predictions.

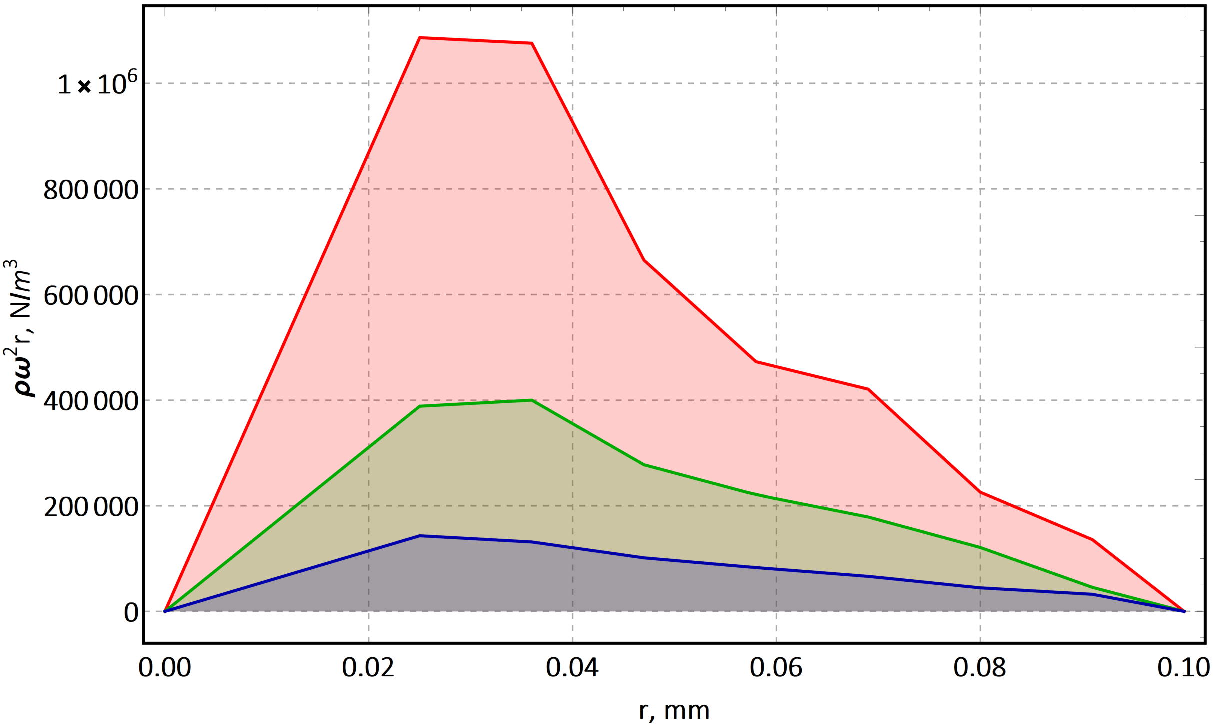

Figure 5.6: **Interpolated function, which is integrated to obtain pressure: Red** 15.6 rev/s**, Green** 7.8 rev/s **and blue is** 3.8 rev/s

Table 5.2

Comparison of the measured pressure, pressure calculated by integrating velocity measurements, and pressure from a numerical model

Angular velocity, rev/s	3.9	7.8	15.6
Pressure directly measured, mbar	55	160	424
Pressure calculated from velocity, mbar	76	206	524
Pressure numerically modeled, mbar	70	205	523
D_{max} experimentally measured, mm			9
D_{max} numerically modeled (bulk), mm			5

5.3. Flowrate and power measurements

In Fig. 5.7, GaInSn experimental setup (see Fig. 4.9) was tested with an open external channel, thus causing flowrate in the loop which was measured. We know the diameter of the circuit at the measuring point (D = 8 mm), so both the flow rate and velocity can be plotted as a function of the magnetic field frequency. It is evident that the flow rate rises as the frequency increases, but the correlation is not linear as in the case of pressure's dependence on the frequency.

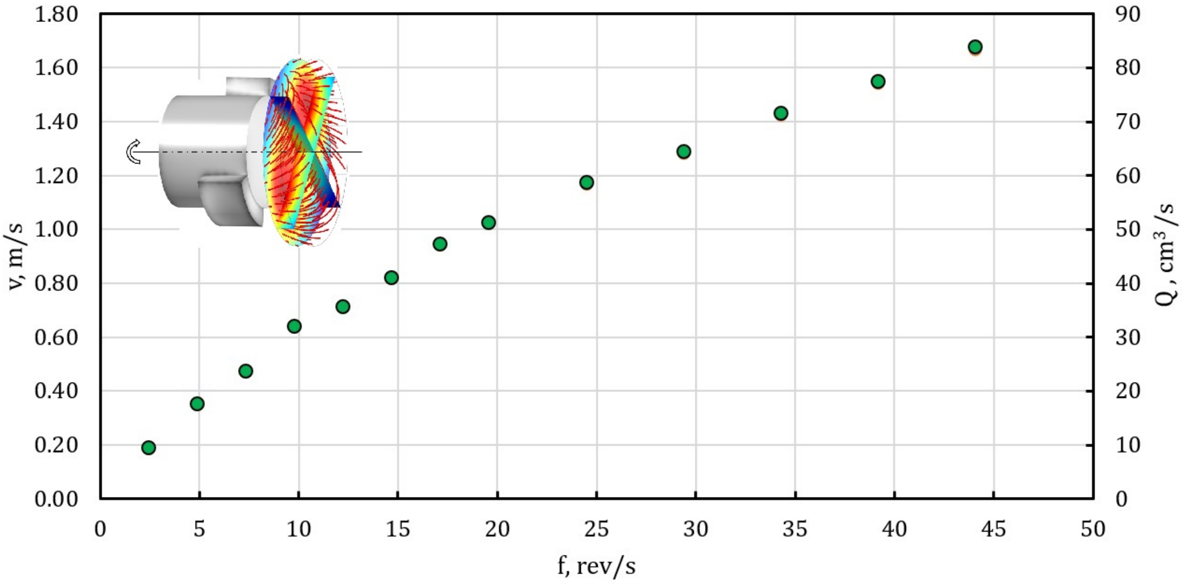

Figure 5.7: **Measured velocity and flow rate in the pipe as a function of magnet rotational speed; Vertical orientation with yokes**

Flowrate and pressure measurements, usually in the form of $p - Q$ curves, are essential tools in characterizing the performance of electromagnetic pumps. Even though the machine studied in this work will not be a part of an enclosed circuit, it is valuable to talk about the developed pressure and power transfer to liquid metal by electromagnetic coupling. Usually, pressure and flow rate are measured simultaneously, and the hydraulic resistance of the circuit is changed, thus obtaining a curve in the p-Q diagram. Pressure multiplied by the flow rate gives us the hydraulic power, which then can be compared, e.g., with control of EM machines pumping the flow (regardless of whether it is a system of AC inductors or permanent magnets driven by an electric motor). Here we measure the power with multiple methods: variable frequency drive and temperature measurements in the metal and calculate it numerically by looking at joule heating.

In Fig. 5.8 p-Q curves are shown for two magnet rotational frequencies. They are obtained by chaining the hydraulic resistance of the circuit and measuring the pressure and

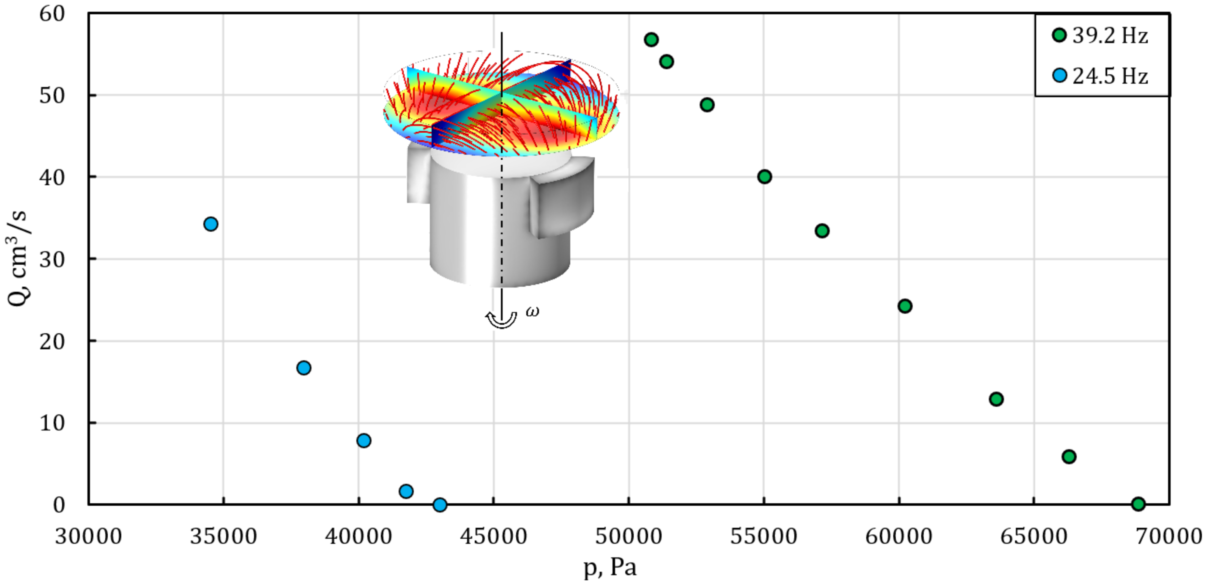

Figure 5.8: **Pressure-flow rate curves at two rotational frequencies; Horizontal orientation with yokes**

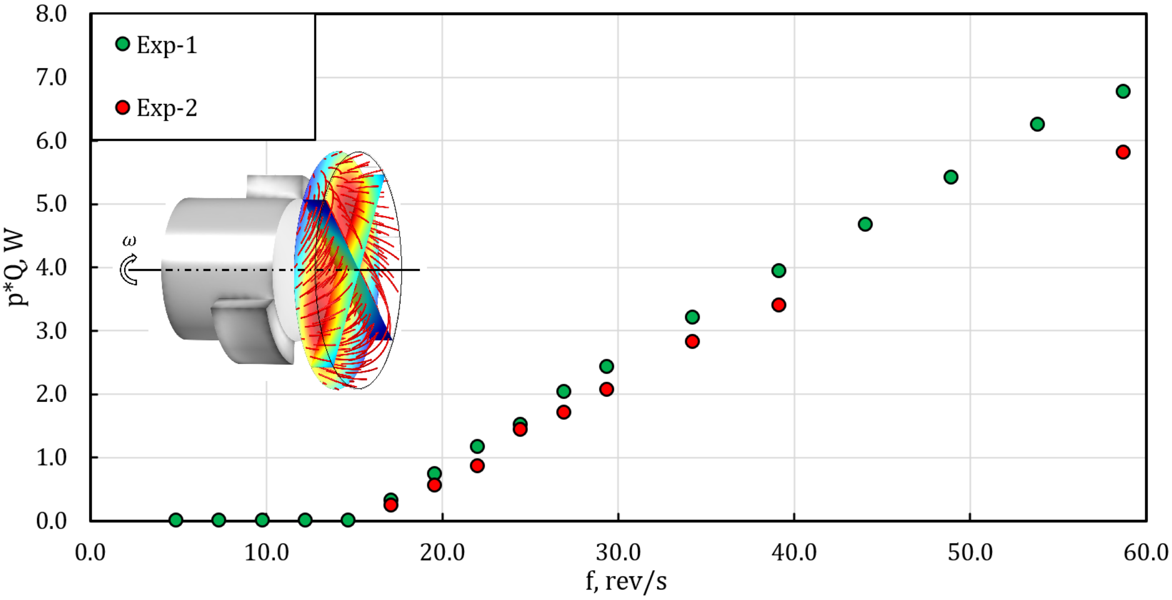

Figure 5.9: **Hydraulic power versus rotational frequency; The picture within the graph indicates the orientation of the vessel**

the flow rate independently. As expected, increasing the hydraulic resistance decreases the flow rate and increases the measured pressure head. Unfortunately, this highlights a drawback of the performed flowrate experiments – to begin with, an unrestricted loop had too high hydraulic resistance. Thus p-Q curves were obtained in a narrow region bordering a closed loop/maximum pressure point. There were experimental attempts to solve this by increasing the pipe diameter to 12 mm, thus increasing the pipe's cross-section by 2.25 times. Still, there were built-in constrictions within the existing setup that could not be overcome.

In Fig. 5.9 hydraulic power is calculated in circulation loop by Eq. (4.1). When sufficient pressure is achieved, the hydraulic power in the circuit rises linearly with the applied magnetic field frequency. At the highest frequency, around 7 W of power goes to pump the metal through the circuit. This measurement is useful for order-of-magnitude efficiency estimates performed later.

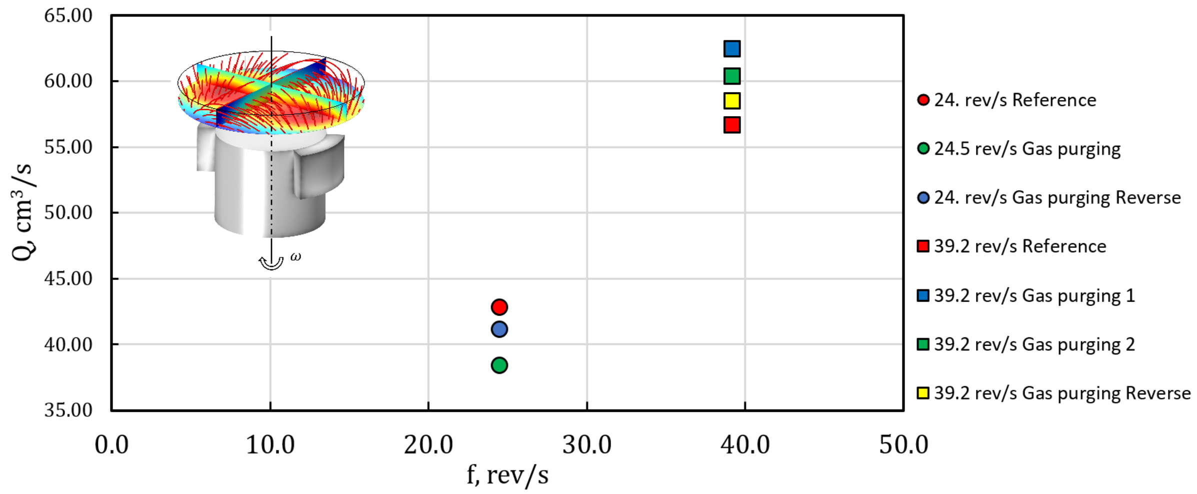

Figure 5.10: **Gas injection effect on flow rate; The picture within the graph indicates the orientation of the vessel**

Fig. 5.10 shows flow rate changes when there is no gas injection and with it. Gas injection experiments were performed both clockwise and counter-clockwise since the position of the injection port (tangential to the cylinder when viewed from the top) made these experiments different. Results show minimal variation (within 10 pct.) between reference and gas injection experiments. These results eliminate the concern of gas fraction interacting with the induced current density distribution, thus reducing the electromagnetic performance of the permanent magnet stirrer.

When the power is measured with the variable frequency drive, the power drawn from the whole circuit is obtained. Power draw is obtained by measuring the supplied current to the three-phase motor. Since we want to isolate the power that will stir and heat the metal, we compare two cases of operation. "No load" where the rotor is spinning

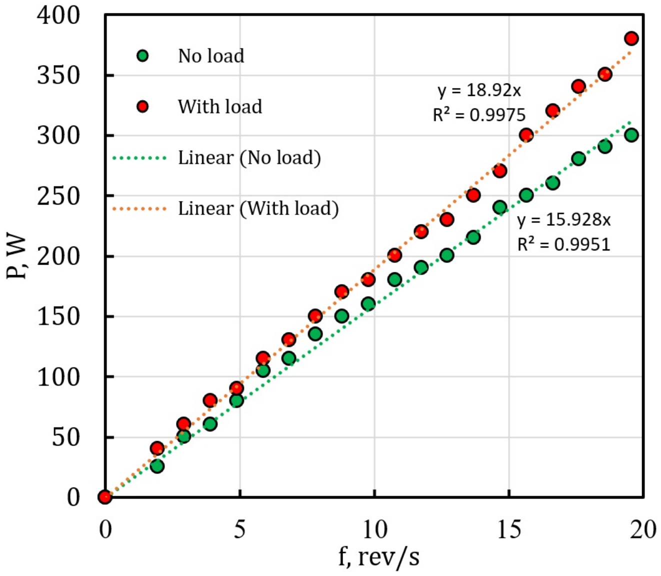

Figure 5.11: **Supplied power to an electric motor with and without load for rotor without yoke**

with no metal on top, and ”with load” where a GaInSn vessel with no flow rate is used. Results and the power difference are shown in Fig. 5.11, and at 19.5 rev/s, only 60 W of power is transferred to the metal.

In Fig. 5.12, different power measurements and calculations are compared. In all cases, increasing rotational frequency, the power rises approximately as a quadratic function. Overall, induction heating calculations show larger values than the experimental temperature measurements indicate. To analyze how rapidly different types of power scale with the frequency, it is helpful to explore it in logarithmic scale as shown in Fig. 5.13.

To quantify the relationship between power and frequency, we can approximate the data points relationship $P(f) = a{\cdot}f^b$. Converting to logarithmic scale changes relationship to $log(P(f)) = a_1 + b{\cdot}log(f)$ where a and a_1 are constants and b is exponent in linear scale and coefficient of slope in the logarithmic scale. Ideally, the power is expected to follow a quadratic relation to the applied frequency. Due to the slip and the skin effect - both parasitic effects - one might experimentally expect a lower power factor than two. This is the case with experimentally measured power measurements, where $b = 1.92$.

However, numerically calculated induction heating values exceed the value, and the slope coefficient b is 2.40. At first, this was an alarming result, but this result is feasible upon further analysis. Skin effect, caused by the induced magnetic field, becomes relevant with higher frequencies. It is known that the induced magnetic field is a monotone function with respect to frequency. Thus this can not cause a higher-than-expected slope on the induction power graph. However, the slip does behave differently. Flow velocity relative to magnetic field velocity is higher in the case of lower frequencies when the

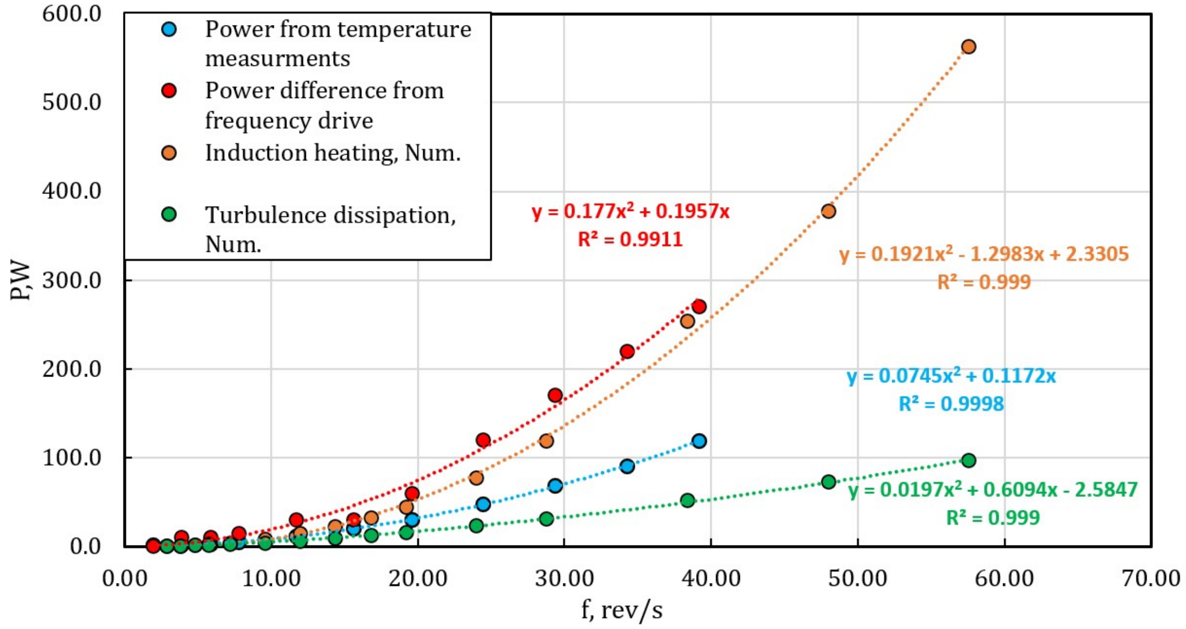

Figure 5.12: **Comparison of power consumption, heating measurements, induced power in metal, and turbulence dissipation power**

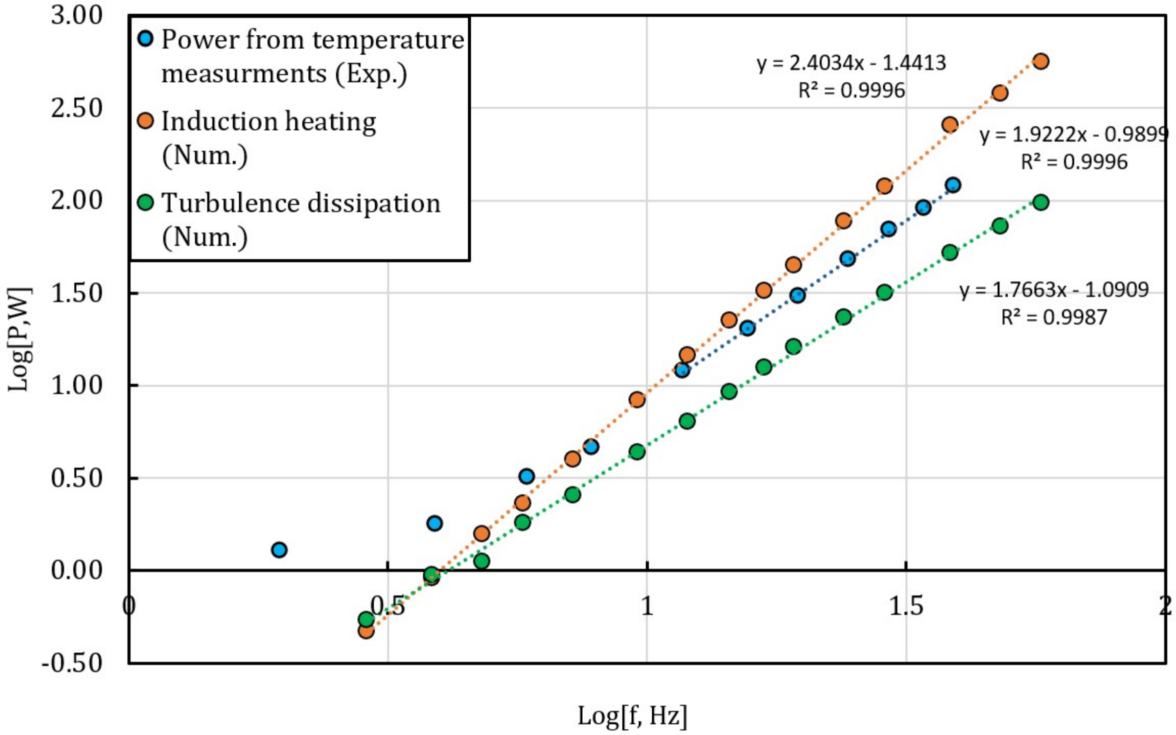

Figure 5.13: **Comparison of heating measurements, induced power in metal and turbulence dissipation power in logarithmic scale; Induced power and turbulence dissipation were calculated numerically, the graph shows integrated values across the whole cylindrical volume**

flow is slower. This can be seen both experimentally and numerically in Fig. 5.2. Thus the effective frequency, which causes forces and velocity in the metal, is more affected by the slip in the lower frequency range. This is the most plausible explanation for a higher-than-expected slope coefficient.

5.4. Bubble size measurements in GaInSn

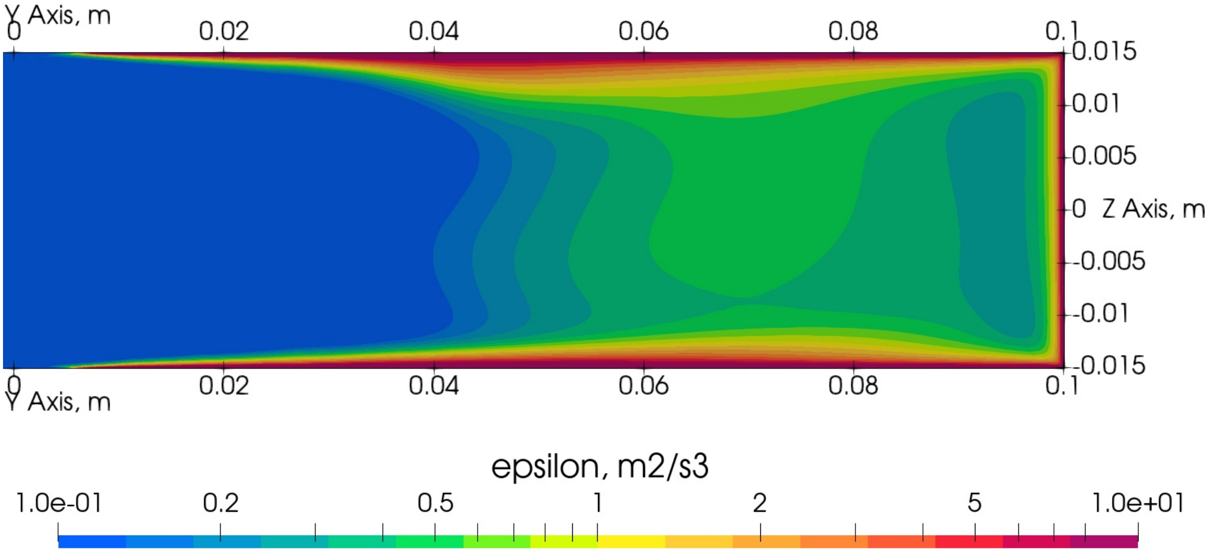

Figure 5.14: **Distribution of the turbulence energy dissipation rate ϵ in the container at a magnet rotational frequency $f = 15.6\ rev/s$; This result was obtained with the Shear Stress Transport (SST) $k - \omega$ turbulence model**

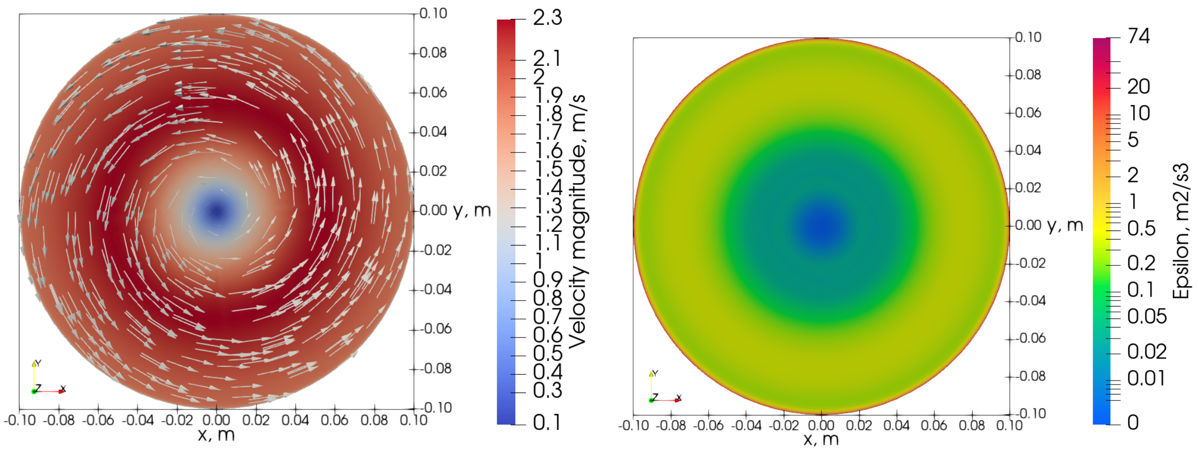

(a) **Velocity** *(b)* **dissipation**

Figure 5.15: **Numerical modeling results for $f = 14.4Hz$; Horizontal cross-section slices container in half at $z = 0$**

Fig. 5.14 shows that the TKE dissipation rate spans multiple orders of magnitude in vertical cross section (y = 0 is the center axis). For further calculations, we use a bulk value which is the dissipation integrated over the volume and divided by the volume. This is believed to be the best predictor of bubble size, but it can not be measured in liquid metal experimentally. If we analyze dissipation on the radial line at $z = 0$, the maximum is expected at $r = 0.7R$, slightly further from the center than the maximum radial velocity ($r = 0.6R$).

Horizontal velocity cuts and the dissipation shown in Fig. 5.15 follow an axially symmetric distribution. Despite having an unsymmetrical 3D force distribution, the time-averaged flow is symmetrical due to the rotational nature of the setup and the co-axial position of the magnet relative to the container.

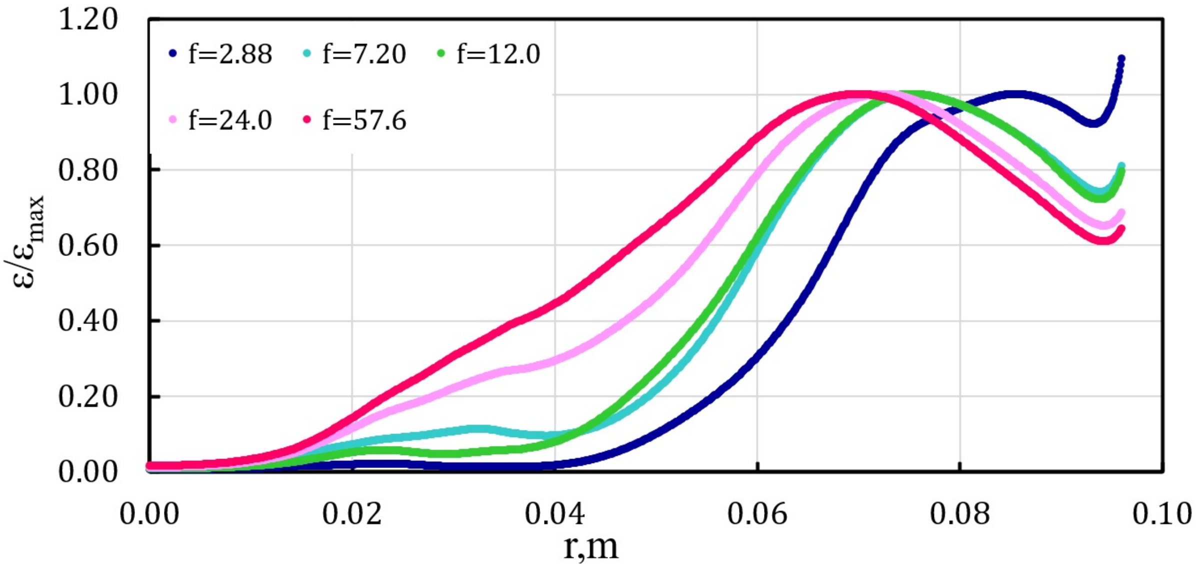

Figure 5.16: **Normalized dissipation vs. radius of a cylindrical vessel; Values are represented on a radial line in the middle of the container (z=0)**

Fig. 5.16 shows that the maximum dissipation value shifts closer to the center if we raise the stirring frequency. In other words, turbulence is more spread out in the container, which is favorable for our purpose. The peak values (except for the slower stirring regimes studied) are found within the range of $r = 0.65R$ to $r = 0.75R$. That is a bit further away from the center than the peaks of the maximum azimuthal velocity, which were found at $r = 0.55R$ to $r = 0.60R$.

Another helpful way to represent the effects of TKE dissipation on bubbles is to directly depict the maximum bubble size with a density plot of a cross-section of the container shown in Fig. 5.17. Note that only a half of the cross-section of the container is visualized. Maximum bubble size is calculated with the formula Eq. (2.10). This shows what would theoretically be the maximum bubble size of 95 % of bubbles if we were to inject the gas in that location. Due to the exponent of -0.4 of epsilon, the maximum bubble size graph does not have so large of a difference between regions as epsilon itself shown earlier in Fig. 5.14.

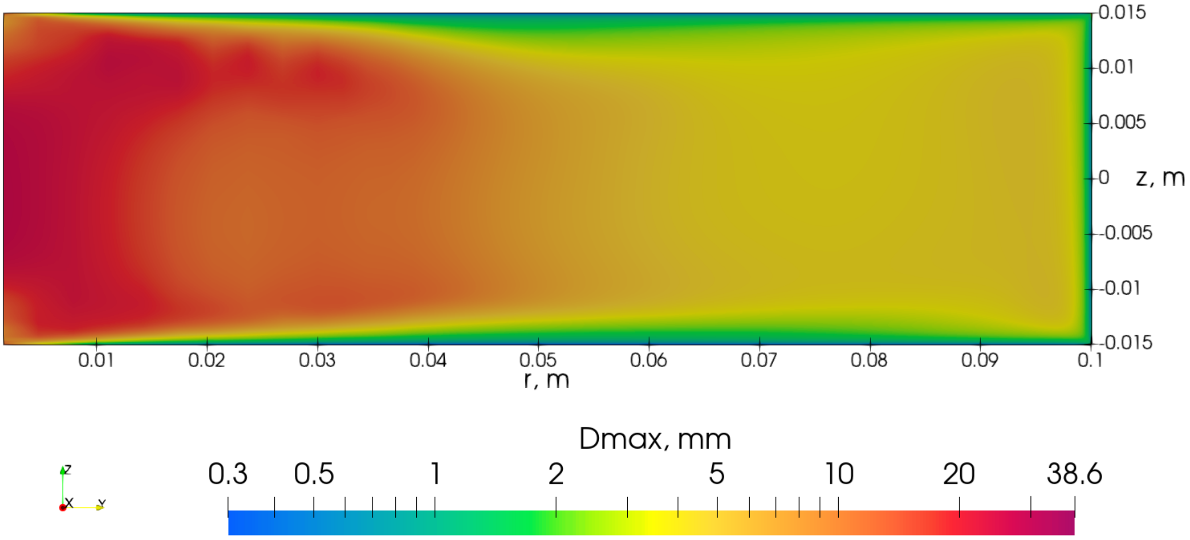

Figure 5.17: **Predicted maximum bubble size in the container at a magnet rotational frequency $f = 14.4\ rev/s$; Relationship Eq. 2.10 was used for the calculation**

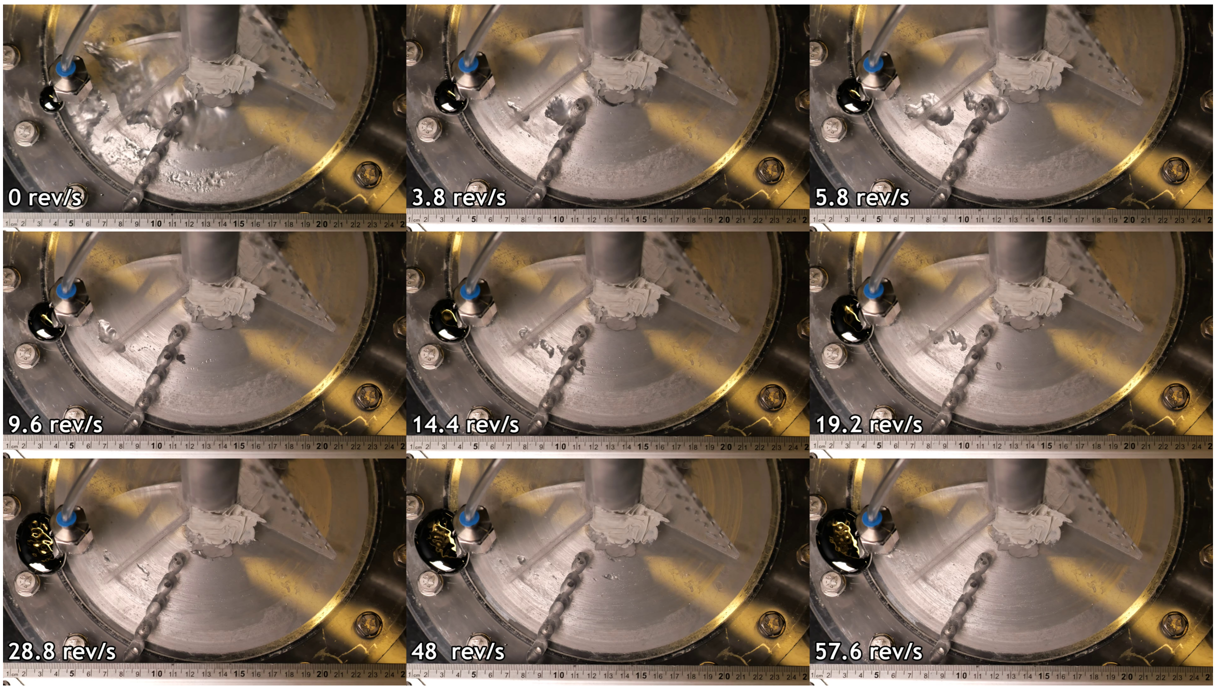

Figure 5.18: **Instant snapshots of the top surface; Various bubble shapes are observed**

Instant snapshots of bubble experiments in GaInSn are shown in Fig. 5.18. The image collage spans across all tested frequencies and highlights that without stirring, the size of produced bubbles is comparable to the radius of the container. Generally, two or three bubbles are visible at a given moment at lower frequencies and up to five bubbles at higher stirring regimes. Slow-motion videos showed some bubble-bubble merging, but overall the number of such occurrences was in the minority.

Due to the turbulent flow, chaotic shapes were observed. In a case with no external flow rate, the lighter fraction is expected to move to the center in a rotating flow. This was observed in an experiment where bubbles moved toward the center in a spiral trajectory. We also performed some tests with external flow rate, but it did not change the bubble trajectory.

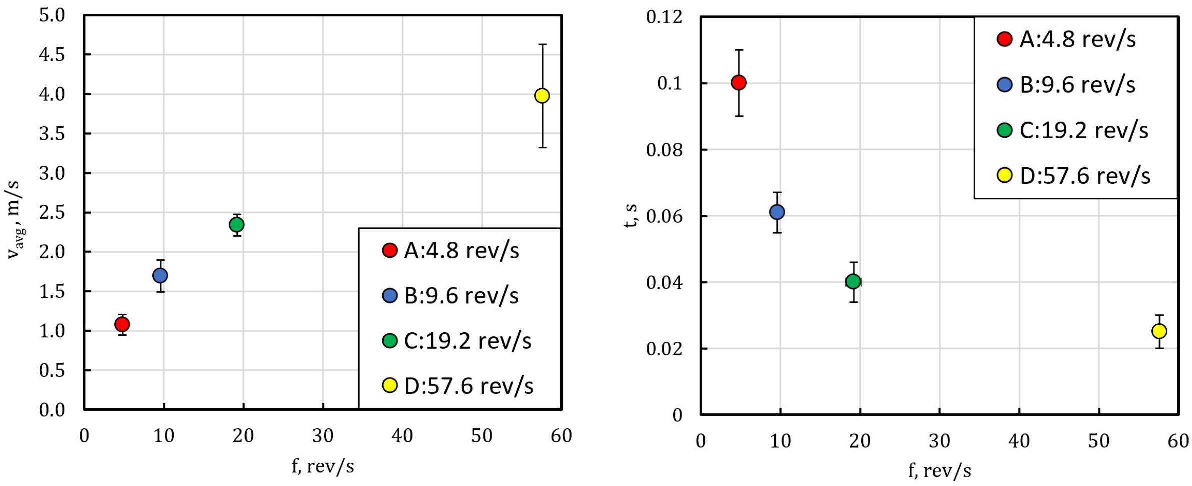

(a) **Speed** *(b)* **Residence time**

Figure 5.19: **Bubble tracking results for four stirring frequencies; The error bar is one standard deviation**

Bubble flow velocity and residence time was measured by analyzing slow-motion videos frame by frame. With an exposure time of 1/180 s, the bubble path was visible for 5-15 frames, which is plenty to calculate the total bubble residence time. An exception was the case with the fastest stirring, there, it was impossible to track an individual bubble from inlet to outlet due to its small size and large velocity. The bubble residence time was extrapolated, knowing velocity and distance. Bubble velocity was obtained by measuring the center of mass movement of 10 bubbles for each stirring regime for 2-4 frames. Measurements are shown in Fig. 5.19. Bubble velocity shown in Fig. 5.19a was measured from 1 to 4 m/s which is on par with UDV measurements seen in Fig. 5.1. Though, direct comparison is avoided because it is unclear how bubble velocity correlates with the flow velocity. Bubble residence time in the tested range is from 0.025 to 0.1 seconds which is insufficient in degassing context.

Overall there was not a significant variation in the bubble velocity. This is the opposite of the results of spinning nozzle tests in water [25, 66]. There the bubble size spectrum is large, and also the trajectories they take are more complex, and bubbles manage to recirculate more through the volume. Bubble residence time could be improved by tilting the setup by 90 degrees. An example of this is shown in Fig. 4.9. By doing this geometrically, the vertical distance between the inlet and the outlet increases significantly.

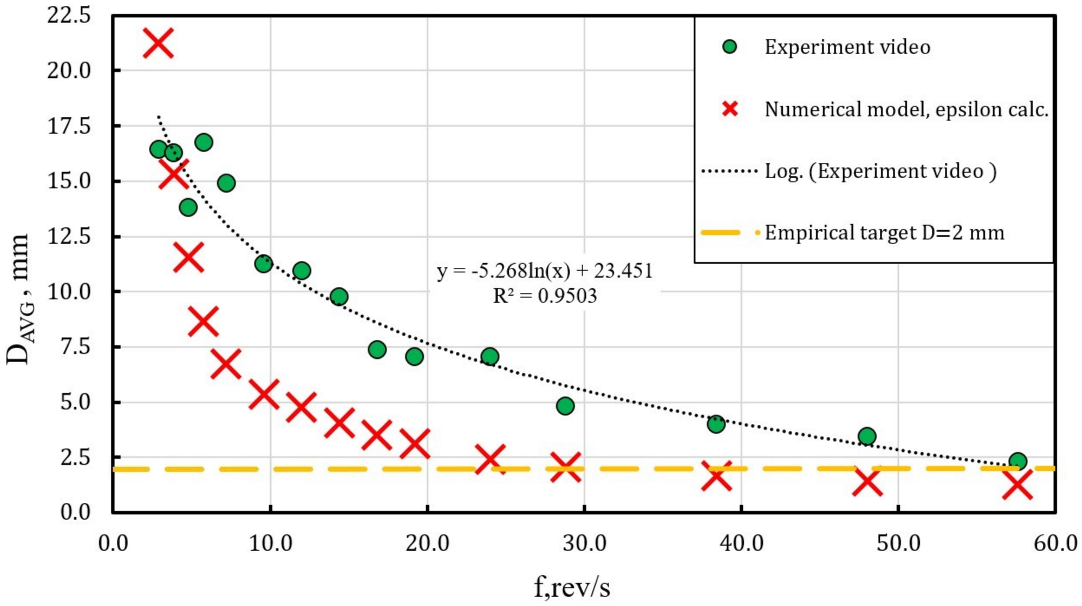

Figure 5.20: **Mean bubble size a function magnet rotational frequency; Experimentally measured value comparison to analytical/numerical calculations; The dashed orange line indicates the empirical target**

Moreover, it would be possible to inject gas in a flow parallel to the force of gravity, thus prolonging the rise time of bubbles because of Archimedes' force. It is estimated that by changing the direction of gravity relative to flow, we expect to improve residence time by an order of magnitude. It was tried experimentally, but initial experiments were unsuccessful for two circumstantial reasons. A mass flow controller was not yet used, and the gas outlet in the tilted setup was narrower, creating an excess gas collection.

Fig. 5.20 shows experimentally mean bubble size decreased from 16 to 2.3 mm reaching the minimum desired threshold (ideally 1 - 2 mm bubble size should be achieved) [9]. Numerical results predict a similar reduction in size from 22 to 1.2 mm with increasing frequency. Unfortunately, our analytical estimate by Eq. (2.10) does not provide any information about the bubble distribution but instead works as an upper limit for the predicted bubble size. More precisely, 95 % off bubbles should be equal to or smaller than the calculated value. In practice, the numerical model underestimates the predicted bubble size (by overestimating ε). Experimentally ε cannot be measured, however, to validate the numerical model, we can compare both pressure and velocity measurements. For example, the numerical model overestimates developed pressure by 1/3, however, assuming the same difference for epsilon, this would not fully explain the discrepancy between the experimentally observed bubble size and the analytical calculated one.

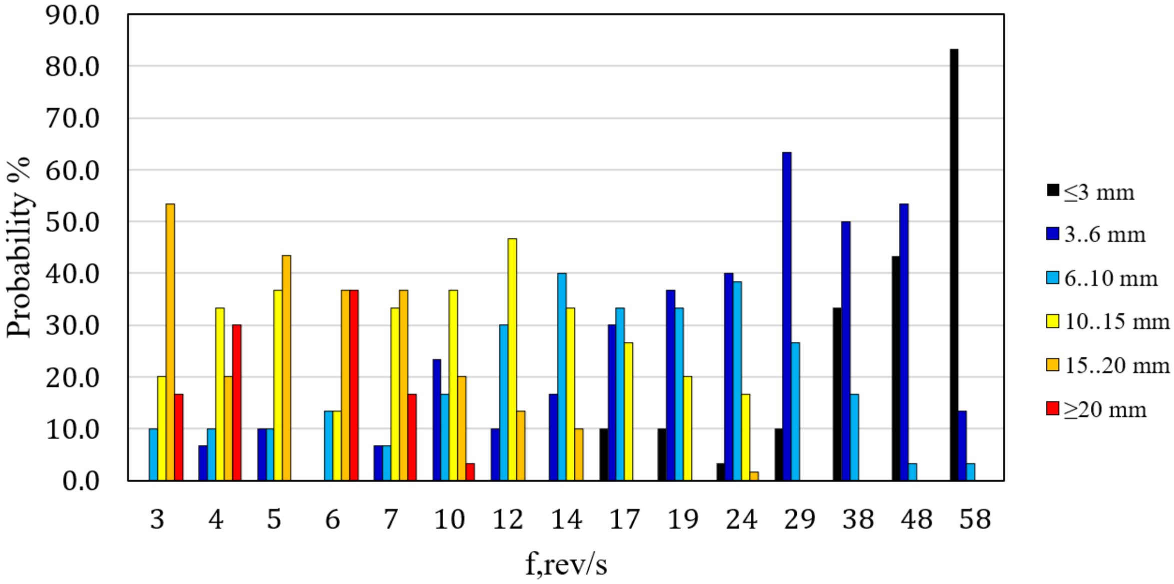

Figure 5.21: **Bubble size distribution across different stirring frequencies**

Fig. 5.21 shows bubble size distributions across the whole tested frequency range highlighting the shift to smaller bubbles denoted in darker colors. Overall the size of bubbles can span an order of magnitude regardless of the stirring frequency. This fact complicates the theoretical analysis since most of the volume of the gas could be found in relatively few large bubbles, but a lot of surfaces could be formed by many tiny bubbles.

A comparison in Fig. 5.22 is made to understand whether size reduction follows a theoretically predicted trend. The orange line is simply a plot of Eq. (2.10) at relevant ϵ values found in the experiment. Since it is impossible to measure ϵ in liquid metal, the numerically modeled value was taken. More specifically, we have bubble size measurements at a certain frequency, and the ε value is provided by the numerical model at that frequency. Experimental values follow a bubble reduction trend with the same slope as the theory predicts (-0.4). However, the absolute values are about two times larger than theoretically predicted.

Turbulence kinetic energy dissipation rate ϵ is the most important bubble size predictor we obtain from the numerical modeling results. In Fig. 5.23 ε is analyzed as a function of the frequency of applied magnetic field at fixed positions at regular and logarithmic scales. It is possible to see that ε rises rapidly with the frequency. A logarithmic plot is analyzed to quantify how quickly it rises, and the two regimes become distinct. To quantify the relationship between ε and f we can approximate the curves with straight

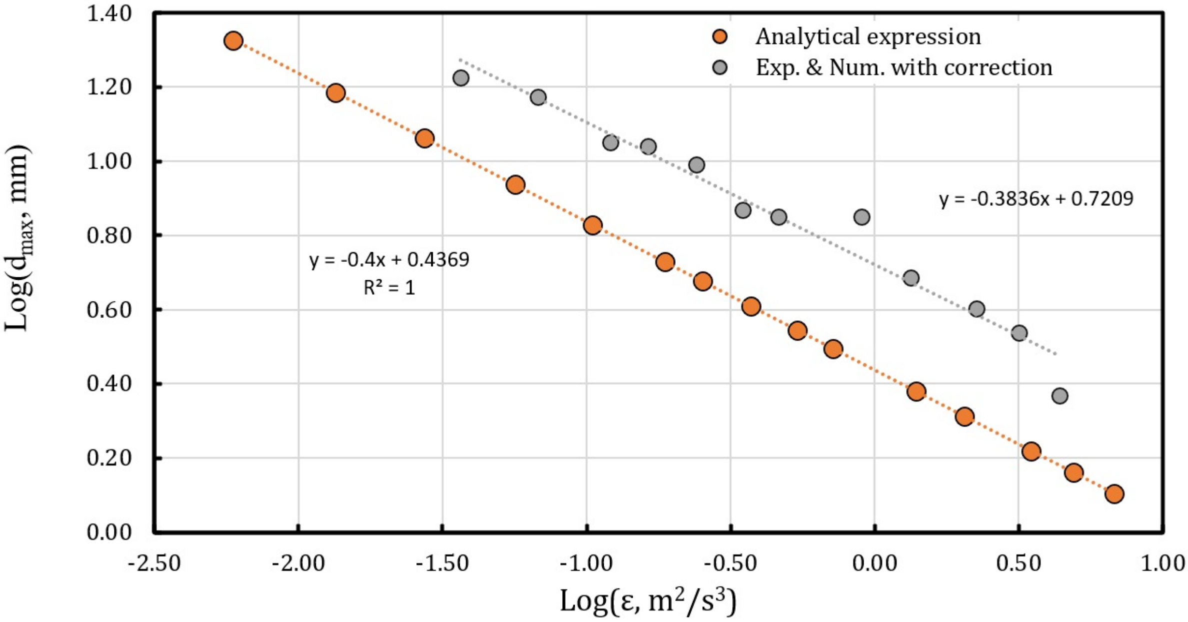

Figure 5.22: **Mean bubble size predicted by analytical function and experimentally measured bubble size at numerically calculated epsilons values**

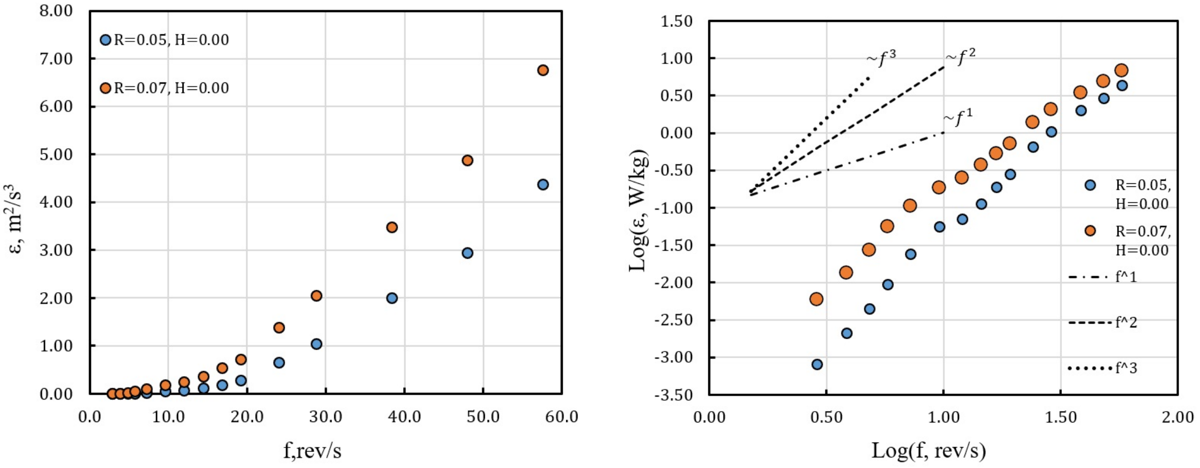

(a) **Linear scale**

(b) **Logarithmic scale**

Figure 5.23: **Numerically calculated epsilon values as a function of magnet rotational frequency**

line $log(\varepsilon) = a_1 + b \cdot f$ where a_1 is a constant and b is the coefficient of a slope. For the first six data points in the frequency range $b = 3.43$. Last six data points gives $b = 1.95$. This shows us that at higher frequencies, it is harder to “pump in” more energy into the system by electromagnetic forces. Reasons for this are skin-effect, a slip of magnetic field relative to flow, and possibly the nature of turbulence itself.

5.5. Scaling findings to aluminum

Table 5.3

Dimensionless numbers of laboratory model and numerical prototype

-	Unit	GaInSn model	Aluminum lab model	Aluminum industry prototype
R	m	0.10	0.05	0.30
V	L	1	1	50
u	m/s	5	2.5	6
f	Hz	57.6	57.6	10
Re	-	$4.4 \cdot 10^5$	$1.5. \cdot 10^5$	$1.0 \cdot 10^6$
Re_m	-	$2.1 \cdot 10^0$	$7.6 \cdot 10^{-1}$	$1.1 \cdot 10^1$
Ha	-	$6.1 \cdot 10^2$	$3.7 \cdot 10^2$	$2.2 \cdot 10^3$
N	-	$3.2 \cdot 10^{-2}$	$1.3 \cdot 10^{-1}$	$7.3 \cdot 10^{-1}$
Pe	-	$1.3 \cdot 10^8$	$3.1 \cdot 10^7$	$4.5 \cdot 10^8$
Ω_D	-	$1.5 \cdot 10^1$	$5.6 \cdot 10^0$	$3.4 \cdot 10^1$
δ	m	0.037	0.030	0.072
ε	W/kg	5	N/A	1
D_{max}	mm	2.2	10	5
τ	s	13	N/A	26

Main system parameters and dimensionless numbers are collected in Table 5.3. The GaInSn model, laboratory aluminum model, and aluminum industry prototype are compared here. The linear size-wise aluminum prototype is three times larger, and its volume is around 50 times bigger than laboratory experiments. Velocity predicted by numerical modeling is 5 m/s for the GaInSn model and 6 m/s for the industry prototype. Due to the larger size, the Reynolds number still will be significantly larger in the industry prototype. Used frequencies on the larger scale are naturally smaller. Due to lower frequencies and larger size, skin-depth is bigger in absolute terms. Relative to the smallest dimension, this ratio is more or less constant since it is one of the main limiting factors for electromagnetic stirring.

Hartmann’s number is bigger than unity in all cases, so electromagnetic forces dominate viscous forces. Stuart’s number is smaller than the one in all cases, with the largest value for the industrial prototype. This indicates that electromagnetic forces, at best, are comparable to inertial forces. Magnetic Reynolds number is around unity for laboratory models and 10^1 for the prototype. This means that the velocity of the conducting fluid will significantly impact the magnetic field distribution. Maximum values of dimensionless frequency are 15 for the laboratory model and 34 for the industrial prototype. That means diffusion of the magnetic field can not keep up with the rapid changes of the magnetic field. This is on par with literature where optimal dimensionless frequency for maximum energy transfer is around $\Omega_D = 10..50$ (See section 5.1). The TKE dissipation rate in the industry prototype was lower than in the laboratory experiment (values in bulk). Thus the predicted bubble size is around 5 mm. Characteristic mixing time rises with the size, and it is two times longer for the industry prototype. This indicates that permanent magnet machines work well as electromagnetic stirrers in this setting. This is also supported by the Péclet number, which tells us that forced convection will dominate the mass transfer.

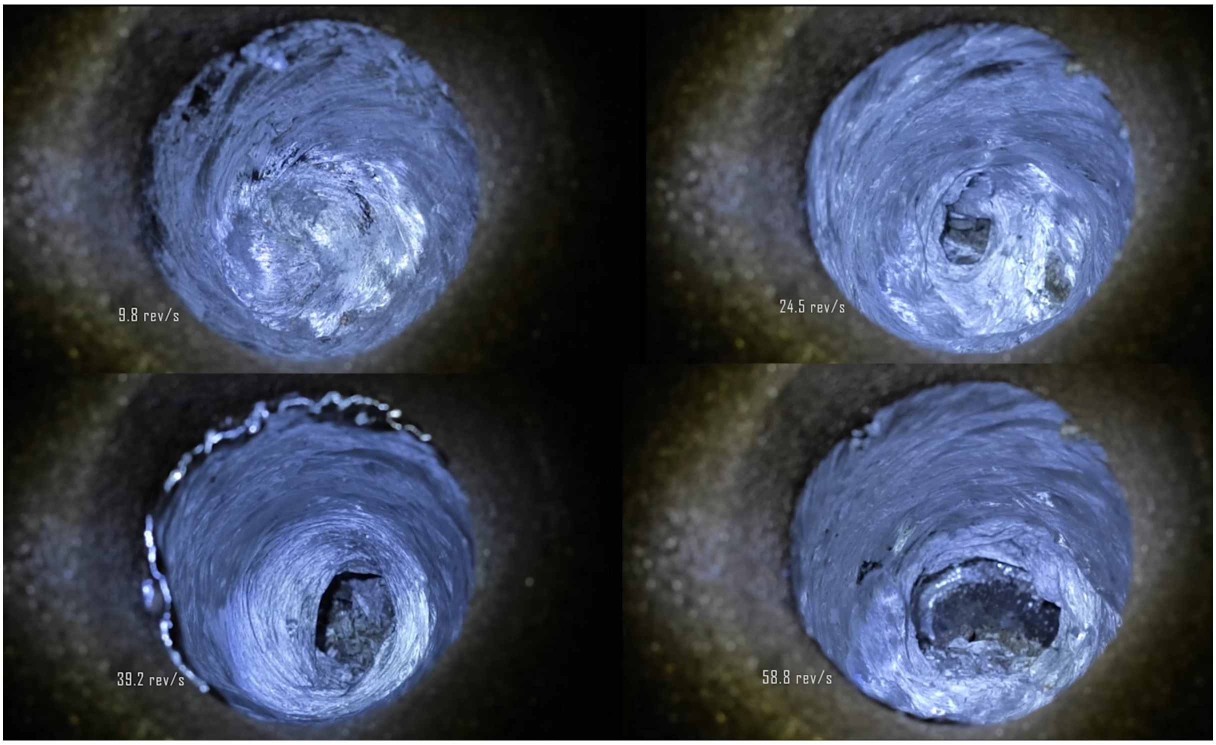

Figure 5.24: **Instant snapshots of an aluminum experiment where argon was injected in an intense aluminum tornado-like flow; For different magnetic fields, rotational frequencies are shown**

Fig. 5.24 shows four instant snapshots of the aluminum experiment. It is a top-down view of different magnet rotational velocities tested, which result in a tornado-like flow where in the most intense stirring regimes, the eye of the tornado reaches the bottom of the crucible. By analyzing the videos, it has been observed that without stirring or with little stirring (up to 10 - 15 rev/s), the oxide film traps the argon in a gas pocket in the size of all crucible diameter. Introducing stirring above 1.5 m/s changes the situation drastically since gas does not collect under the top layer of slag but escapes as individual bubbles.

The bubble size is reduced to the 5 - 10 mm range at the highest stirring intensities. Such surface deformations, of course, are not welcomed in the aluminum industry. Therefore this experiment tests only the electromagnetic performance (how quickly aluminum can be stirred) and the bubble injection in aluminum. In industrial size, this problem becomes simpler since aluminum volume is larger. Thus there can exist a zone with a turbulent flow where the bubble is injected and a relatively calm surface that does not break the top film, which has a protective function.

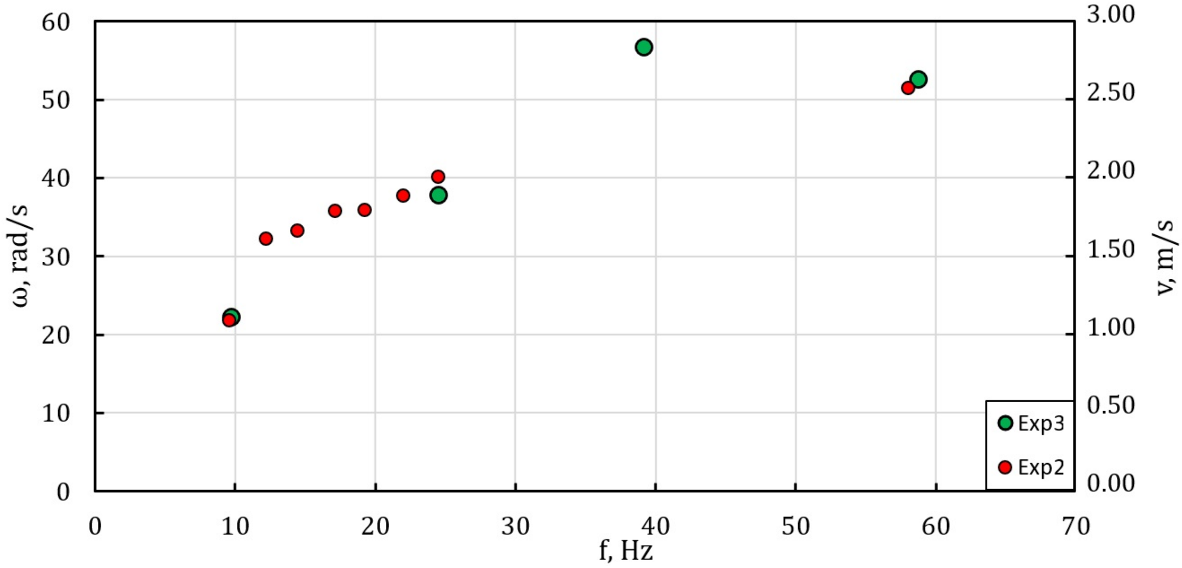

Figure 5.25: **Flow angular velocity and velocity as a function of magnet rotational frequency in laboratory aluminum experiment; Two independent experiments are shown**

Filming the surface with a high frame-rate camera (180fps) with low exposure time (1/6400 s) allows us to track the angular velocity of the aluminum surface. Flow velocity at the maximum radial position (ignoring the turbulent boundary layer and assuming constant angular velocity along radius) can be calculated by the formula $v = \omega r$. Both angular velocity and velocity vs frequency have been plotted in 5.25. During two separate experiments, a flow velocity of around 2.5 m/s was reached in a crucible with a diameter of 101 mm.

Before and after the experiment aluminum samples were taken in a graphite crucible ($L \times W \times H = 50 \times 34 \times 16$ mm) and their vertical cross-section was analyzed as shown in Fig. 5.26. In the reference sample, the pores can be found near the top surface where the metal is solidified the last. This is a normal occurrence since S/L the interface during the solidification can reject the inclusions like gas bubbles (up until it is physically impossible). After electromagnetic stirring and gas injection, another sample was taken. Despite having some argon flow rate at all times, the resulting sample is worse than the reference. This might be explained by the fact, that we created massive surface deformations and exposed

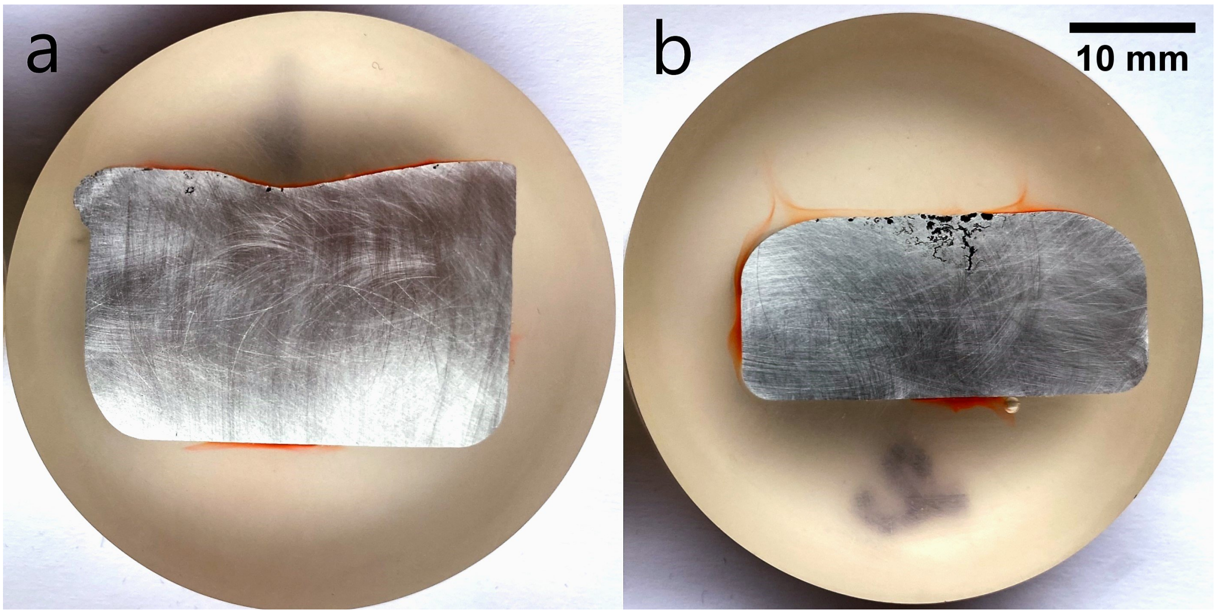

Figure 5.26: **A365 aluminum samples: a) reference before experiment; b) after experiment where aluminum was stirred and purged for 5 minutes**

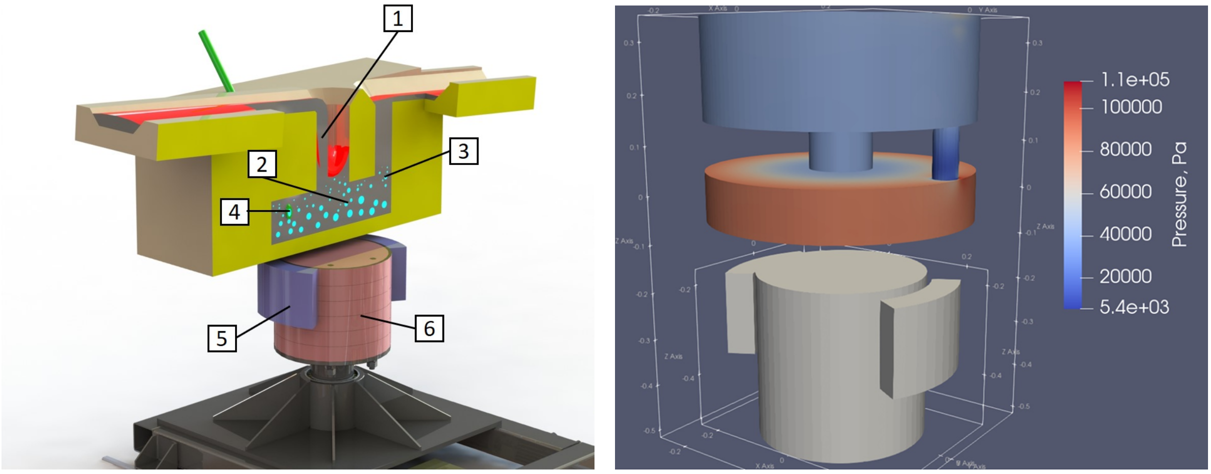

(a) **Industrial concept**

(b) **Numerical model representation**

Figure 5.27: **(a) Industrial degassing unit concept: 1 - inlet of contaminated aluminum; 3 - outlet of degassed aluminum; 4 - argon injection; 5 - iron yokes for magnetic flux optimization; 6 - permanent magnet rotor; (b) representation of it in the numerical model; An extra reservoir is added to ensure the same flow is in the inlet and the outlet**

the aluminum surface to the environment. It has been shown that degassing in larger scales with a lid and inert atmosphere drastically differs in degassing speed and minimum possible concentration [2].

An industrial degassing concept (Fig. 5.27a) is modeled numerically (Fig. 5.27b) to predict the created flow. Here a time-dependant model solved a 3D turbulent flow again coupling the EM problem with fluid mechanics. To ensure the same flow rate in the inlet and the outlet an extra reservoir was added which exists purely in numerical problem. This was done because the flow rate is unknown in this problem, thus has to be solved.

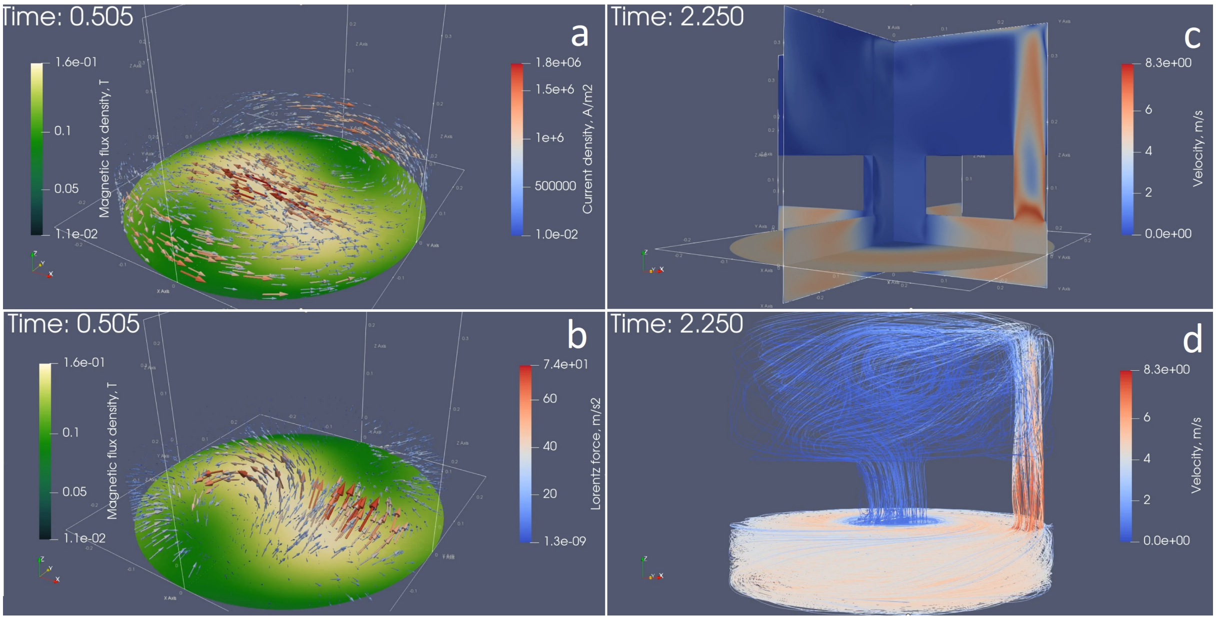

Figure 5.28: **Numerical modeling results in industrial size degassing unit; Dimensions of setup are shown in 4.2, and the rotational frequency of the magnet is 10 Hz: a) induced current density; b) Lorentz force; c) velocity magnitude plot; d) Velocity streamlines**

Fig. 5.28 shows the magnetic field, induced current density, force density, and velocity obtained by the numerical modeling problem on an industrial scale. The current forms two horizontal loops in the vessel which are rotating synchronously with the magnet. The force density is three-dimensional and also time-varying with a double frequency of the applied magnetic field. Due to geometry constraints, the force forms a strong azimuthal flow up to 6 m/s in bulk.

Fig. 5.29 shows ϵ and D_{max} distribution. It is clearly shown that in the outlet, ϵ values are large, and the expected bubble size would be easily in the sub-millimeter range. However, a more reasonable approach is to analyze values in bulk. For 10 Hz (which is the top of the planned range), the dissipation is around 1 $\frac{W}{kg}$ yielding 5-10 mm large bubbles. These results indicate a need for some kind of constriction around gas injection to ensure high enough epsilon values, as seen in the outlet.

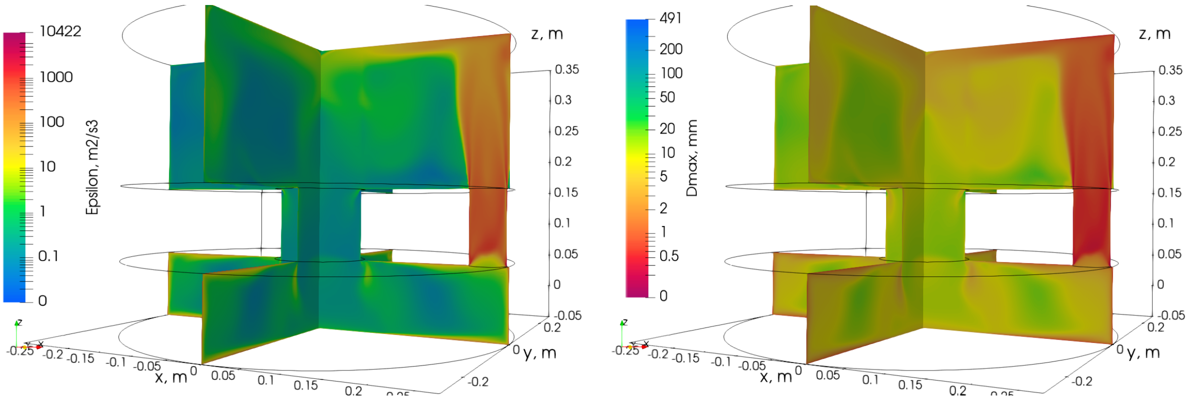

(a) ϵ, $\frac{W}{kg}$ *(b)* D_{max}, *mm*

Figure 5.29: **Numerical modeling results of TKE dissipation rate in industrial size degassing unit at $f = 10Hz$: (a) ϵ distribution and (b) maximum bubble size predicted by ϵ**

The concept of mixing time τ_m is introduced to characterize mixing by stirring in a liquid metal bath. Assuming isotropic and homogeneous turbulence equation (5.2) calculates the time for mixing that takes place by 'eddy diffusion' where the largest eddies play the dominant role in this process. Thus τ_m depends on a characteristic vessel dimension L, for instance, the radius.

$$\tau_m \sim 100\left(\frac{L^2}{\epsilon}\right)^{\frac{1}{3}} \tag{5.2}$$

Inputting value for $R = 0.3$ m and $\varepsilon = 1$ W/Kg, mixing time τ is 26 seconds. This estimate shows that stirring-wise the setup is very potent.

Increasing free surface deformations were observed with increasing the applied frequency of the magnetic field, as seen in Fig. 5.30. This is a good sign. It shows the whole designed range from 2-11 Hz can be used without saturation taking place. Unfortunately, no flow velocity measurements are possible in molten aluminum. Practically the only way to confirm the performance of electromagnetic stirring would be pressure and flow rate measurements.

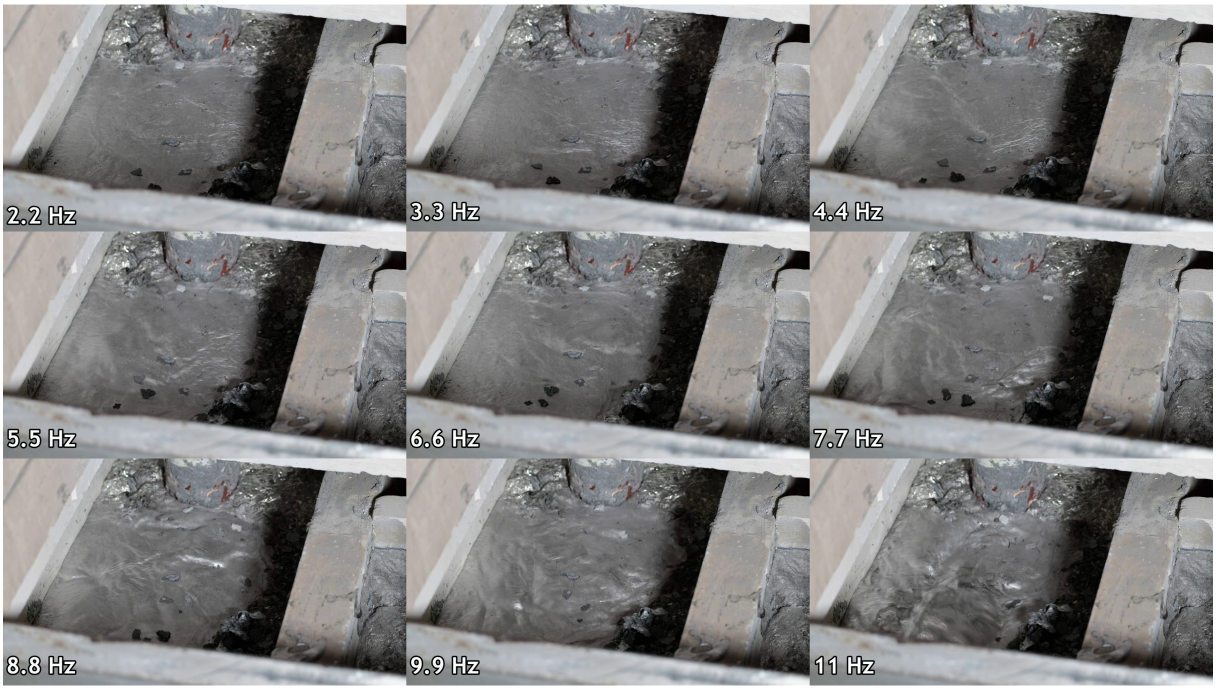

Figure 5.30: **View of free surface deformations on industrial degassing prototype experiment when permanent magnet stirrer is operating at different frequencies; The angle of the camera view is shown in Fig. 4.13 numbered 3**

6. SUMMARY AND CONCLUSIONS

Most of the tasks were carried out successfully, and the thesis objectives were achieved. In the process following conclusions were made:

1. Bubbles can be refined by an electromagnetically created turbulent flow. Experiments imaging the GaInSn surface prove bubble size reduction with more intense stirring.
2. The bubble size in metal flow is correlated to flow condition, mainly ϵ -turbulent kinetic energy dissipation rate. Numerical models providing ϵ values are validated using experimentally measurable quantities such as velocity and pressure.
3. Author proposes a method for scaling the bubble refinement problem to aluminum. Numerical modeling tools can calculate the dissipation, which, together with empirical formulas, are used to predict the bubble size in aluminum.
4. Laboratory scale experiments with aluminum indicate significant bubble behavior changes when stirring is applied. Imaging the free surface showed bubble size reduction.
5. The developed pressure head is high enough for the system to work as an electromagnetic pump. This is an added benefit that none of the existing degassing methods has.
6. Iron yokes can be used as cost-effective tool as magnetic flux concentrators even on rotating permanent magnet machinery. This setup provides at least a 30 % pressure increase which means more intensive flow or the ability to use 27 % less magnetic material for the same hydrodynamic performance.
7. Power measurements show how much energy can be transferred to the system by EM forces. They proved that the limit in frequency was not reached in the tested frequency range. This is useful for building and scaling EM machines for metal stirring.
8. Despite producing a small enough bubble, vertical setup proved to have very poor bubble residence time.

6.1. Publications and participation in conferences

Publications

1. R. Baranovskis, D. Berenis, I. Grants, A. Bojarevics, T. Beinerts, M. Milgravis
   Contactless Aluminum Degassing System—GaInSn Model Experiments and Numerical Study
   Journal of Sustainable Metallurgy (2021)

2. D. Berenis, R. Baranovskis, I. Grants, T. Beinerts, A. Bojarevics,
   Permanent magnet bottom-stirred swirling flow in coaxial shallow cylindrical containers
   Physics of Fluids 33 (5), (2021)

3. I. Grants, R. Baranovskis
   Experimental observation of metal-electrolyte interface stability in a model of liquid metal battery
   Magnetohydrodynamics 57 (2), (2021)

4. R. Baranovskis, M. Sarma, M. Scepanskis, T. Beinerts, A. Gaile, S. Eckert, D. Räbiger, E.H. Lehmann, K. Thomsen, P. Trtik
   Investigation of Particle Dynamics and Solidification in Two-Phase System by Neutron Radiography
   Magnetohydrodynamics 56 (1), (2020)

5. I. Kaldre, C. Wang, R. Baranovskis
   Experimental investigation of weld pool flow under external DC magnetic fieldy
   Magnetohydrodynamics 55 (4), (2020)

6. I. Kaldre, A. Bojarevics, T. Beinerts, R. Baranovskis, R. Nikoluskins, M. Milgravis, M. Kalvans
   Contactless electromagnetic method for aluminium degassing
   IOP Conference Series: Materials Science and Engineering, 424 (1), (2018)

7. T. Beinerts, A. Bojarevics, R. Baranovskis, M. Milgravis, I. Kaldre.
   Permanent magnet dipole stirrer for aluminium furnaces
   IOP Conference Series: Materials Science and Engineering, 424 (1), (2018)

8. A. Bojarevics, R. Baranovskis, I. Kaldre, M. Milgravis, T. Beinerts
   Two cylinder permanent magnet stirrer for liquid metals
   IOP Conference Series: Materials Science and Engineering, 228 (1), (2017)

Conferences

1. 12th International PAMIR International Conference - Fundamental and Applied MHD July 04 – 08, 2022, Krakow, Poland
   R. Baranovskis, D. Berenis, I. Grants, A. Bojarevics and T. Beinerts
   Bubble dispersion in liquid metal flow.

2. 2022 CaNAl Alumina Summer School, July 13 – 16, 2022, Trondheim, Norway
   R. Baranovskis, D. Berenis, I. Grants, A. Bojarevics and T. Beinerts
   Novel electromagnetic degassing system

3. Electromagnetic processing of materials 2021, June 13 - 17, 2021, Riga, Latvia
   R. Baranovskis, D. Berenis, I. Grants, A. Bojarevics and T. Beinerts
   Experimental modelling of permanent magnet stirrer for aluminum degassing

4. XIX International UIE Congress on Evolution and New Trends in Electrothermal Processes (UIE 2021), September 1 – 3, 2021, Pilsen, Czech Republic
   R. Baranovskis, D. Berenis, I. Grants, A. Bojarevics and T. Beinerts
   New contactless aluminum degassing system - GaInSn model experiments with a numerical study
5. 14th Virtual Congress WCCM and ECCOMAS 2020, January 11 - 15, 2021, online
   I. Grants, R. Baranovskis, A. Bojarevics and T. Kalnins
   Liquid metal battery instability experiment using two-layer gallium-electrolyte model
6. Latvijas Universitātes 79. Konference, Sekcija: ”Lietišķā un fundamentālā magnetohidrodinamika”, (2021)
   R. Baranovskis, D. Berenis, I. Grants, A. Bojarevics and T. Beinerts
   Caurteces un jaudas mērījumi degazatora plūsmas modeļa eksperimentos
7. Latvijas Universitātes 78. Konference, Sekcija: ”Lietišķā magnetohidrodinamika un elektromagnētiskās materiālu apstrādes metodes”, (2020)

R. Baranovskis, D. Berenis, I. Grants, A. Bojarevics and T. Beinerts
Degazācija elektromagnētiski ierosinātā plūsmā - GaInSn eksperimentālā modeļa pirmie rezultāti

8. 11th International PAMIR International Conference - Fundamental and Applied MHD July 01 – 05, 2019, Reims, France
   R. Baranovskis, M. Sarma, M. Ščepanskis, T. Beinerts, A. Gaile, S. Eckert, D. Räbiger, E.H. Lehmann, K. Thomsen, P. Trtik
   Investigation of Particle Dynamics and Solidification in Two-Phase System by Neutron Radiography

9. Latvijas Universitātes 77. starptautiskā konference, sekcija ”Fundamentālā un lietišķā magnetohidrodinamika”, (2019)
   R. Baranovskis, V. Dzelme, A. Jakovics, A. Gaile, I. Kaldre
   Rotējošu pastāvīgo magnētu radītas šķidrā metāla plūsmas skaitliska un eksperimentāla izpēte

10. Latvijas Universitātes 76. starptautiskā konference, sekcija ”Materiālu elektromagnētiskās apstrādes un izpētes metodes”, (2018)
    R. Baranovskis, M. Ščepanskis, M. Sarma, T. Beinerts, M. Kalvāns, K. Thomsen, P. Vontobel
    Daļiņu iesalšanas procesa eksperimentālie pētījumi orientētās kristalizācijas laikā

11. XVIII International UIE-Congress on Electrotechnologies for Material Processing
    R. Baranovskis, M. Milgravis, A. Bojarevics, I. Kaldre
    Liquid Metal Homogenization and Crystallization under Low-Frequency Alternating Magnetic Field

12. Latvijas Universitātes 75. Konference, Sekcija ”Šķidri, elektrovadoši un feromagnētiski materiāli un ar tiem saistītās iekārtas’’, (2017)
    R. Baranovskis, I. Kaldre, A. Bojarevics
    Divcilindru pastāvīgo magnētu maisītājs alumīnijam

13. Latvijas Universitātes 74. Konference, Sekcija ‘‘Lietišķa Magnetohidrodinamika’’, (2016)

R. Baranovskis, A. Bojarevics, T. Beinerts, M. Kalvans
Divu pastāvīgo magnētu cilindru maisītājs šķidru metālu homogenizācijai

Patents

1. LV15144 ELEKTROVADOŠU METĀLISKU UN PUSVADĪTĀJU KAUSĒJUMU MAISĪŠANAS IERĪCE
   Andris BOJAREVIČS (LV), Jurijs GEĻFGATS (LV), Toms BEINERTS (LV), Matīss KALVĀNS (LV), Reinis BARANOVSKIS (LV)
2. LVP2021000051 IEKĀRTA BEZKONTAKTA PLŪSMAS IEROSINĀŠANAI ELEKTROVADOŠOS ŠĶIDRUMOS
   Andris BOJAREVIČS (LV), Jurijs GEĻFGATS (LV), Toms BEINERTS (LV), Reinis BARANOVSKIS (LV)

6.2. Further research

Bubble dispersion in liquid metals has a larger scope of an impact than just liquid metal degassing. This research could apply to range of two-phase liquid metal flows. Most prominent examples include such applications:

1. Decarbonization and stirring of steel furnaces by use of bubble columns. The bubbles rising locally can create a flow throughout the furnace. Bubble dynamics of this process have been researched numerically [67] and experimentally [68]. Steel furnaces also do desulfurization [69] where chemical agents are added on top or injected through a lance via carrier gas in the melt. The latter process shares the aims of bubble dispersion similar to aluminum degassing.
2. Production of hydrogen from natural gas pyrolysis has recently gained interest in research and energy technology. Pyrolysis of natural gas has not yet been commercialized under the aspect of hydrogen production, but when the carbon by-products of this process can be used for material production, the produced hydrogen has a low carbon footprint. This article [70] reviews the literature on the state of the art of methane natural gas pyrolysis process developments and assesses the technology readiness level (TRL). Introducing electromagnetic stirring to bubble reactors, could boost their efficiency and alter the maximum feasible size of reactors. Metal does not take place in the reaction. It works as a catalyst, ensuring the right temperature

and oxygen-free environment for reactions to take place. Without a catalyst (like Nickel), the decomposition still occurs, albeit at higher temperatures. Different metals and molten salts have been proposed as catalyst [71]. Aluminum could be hypothetically used thus sharing a similar problem as this work of "how to break and disperse bubbles in liquid metal".

3. Removal of inclusions using microbubbles is a topic of interest in the aluminum and steel industry [2]. They remove the inclusion by collecting them to the surface/ liquid interface of the bubble and then transporting the attached inclusion to the top, where they can be skimmed. The problem is how to create a dispersed cloud of microbubbles such they do not coalesce with each other. Quoting the authors: *"... the formation of microbubbles is indeed possible in liquid metal systems, provided one has the following elements in place: a rapidly shearing flow system, strong convective flows, a dispersed flow of bubbles, plus abundance of the kinetic energy of turbulence"*. The studied electromagnetic technology in this work can be used to create a turbulent flow in liquid metal systems.

The limits of the studied technology are not fully explored within this work. This leaves room to improve the concept, both by incrementally optimizing some parameters and by fundamentally adding new elements to it. A couple of ideas that could be tested further are:

1. First are improvements in geometry where multiple optimization options seem possible. Increasing the magnetic field is possible by enlarging the magnet and decreasing the non-magnetic gap. That would lead to larger EM forces and faster/ more turbulent liquid metal flow. Increasing container height in the existing setup would improve residence time for the bubbles in the melt. Numerical modeling results showed that in the inlet and outlet, there is a significantly higher TKE dissipation rate. Similarly, a constriction of the channel cross-section area could be applied at the gas injection position. Lastly, the cylindrical container with a liquid metal setup can be shifted 90 degrees to a position that resembles a coin standing on the edge. That would have no effect on EM forces and fluid dynamics in single-phase flow but would drastically change the bubble path in the metal when gas is injected.

2. Second is the usage of not one but two rotating magnets, which are counter-rotating. An example of this is shown in Fig. 6.1. This setup is expected to form a similar flow between two coaxial rotating disks [72] (such setup has also been studied on a large scale with liquid metal in von Kármán Sodium experiment [73]). This causes regions of opposite azimuthal flow near the bottom and top wall. Even though mean flow

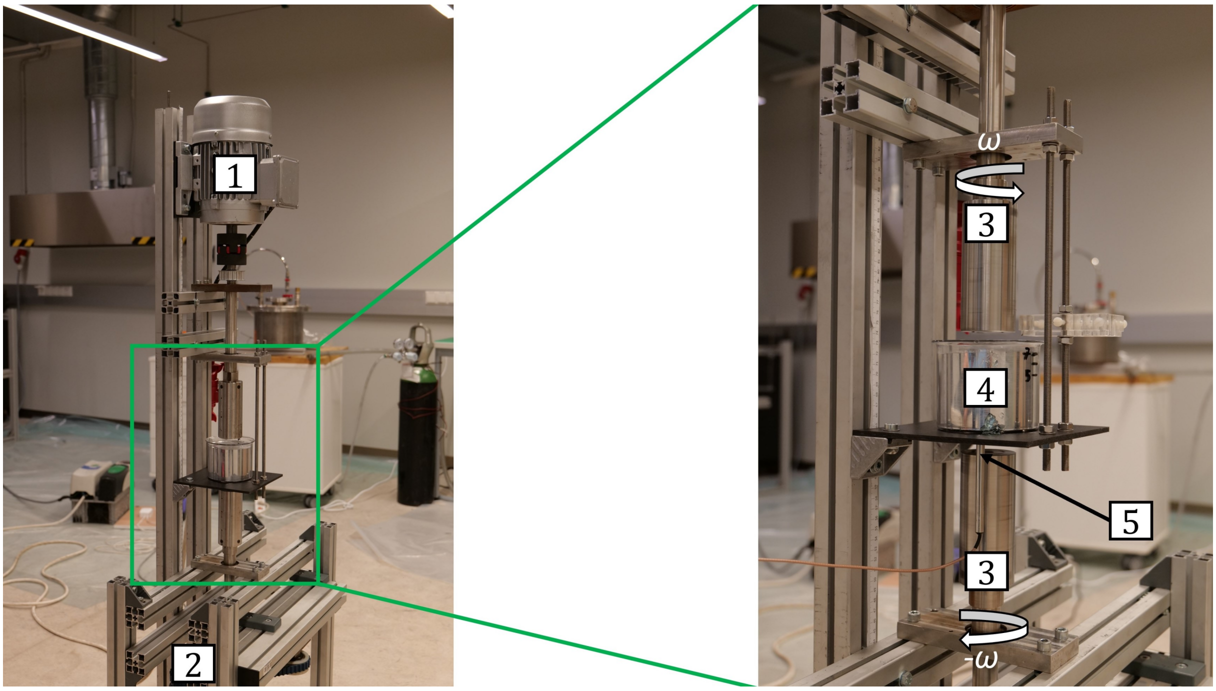

Figure 6.1: **Experimental rig for two magnet shear flow: 1 - electric motor driving upper magnet; 2 - lower magnet motor; 3 - permanent magnets (D=50 mm, H=100 mm, f=10 Hz), magnetization is radial (see blue arrows); 4 - GaInSn container (D=100 mm, H=70 mm); 5 - UDV probe measuring axial velocity**

velocities are lower than compared to one magnet (or one rotating wall) this setup produces high shear forces in the plane which slices the setup horizontally in the middle. Experimentally such a setup was tested as an idea in the laboratory. We saw the system was very sensitive to magnet positioning, it was difficult to balance the strength of electromagnetic forcing probably due to the free surface. The distance between the magnet and the surface of the metal was 20 mm, so the total separation between the magnet surfaces was 110 mm. At this distance there were some visible forces exerted between the magnets, e.g one magnet spinning caused the rotation of the second magnet. In the measurements, shown in Fig. 6.2 it was shown that velocity pulsations (indicated by the error bar) were indeed larger than the time-averaged velocity. Even though the azimuthal velocities are the strongest, it was easier to measure the axial velocity in this particular geometry.

3. Thirdly, an obstruction could be added to the flow. Adding an obstacle in rapid moving flow would cause a turbulent wake behind it. That area might be a good candidate for gas injection. Yet, in the case of aluminum, the object would have to be from ceramic material so that it would ntot be prone to erosion. However, a strong localized magnetic field is an intriguing way to create a virtual obstruction. An example of this is in articles by Román [74, 75] where they experimentally study vortex wakes produced by localized Lorentz force in a shallow layer of electrolyte.

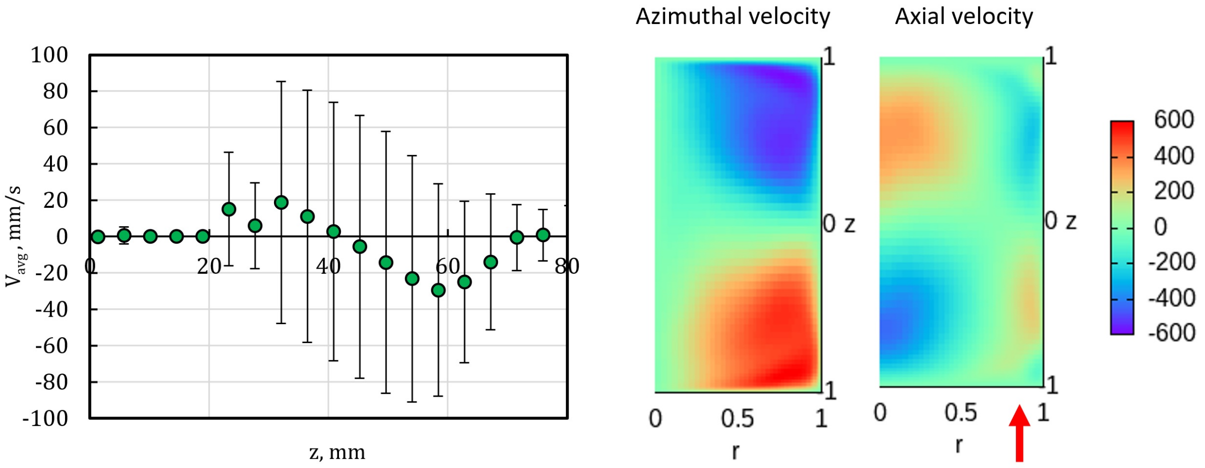

(a) **Exp. axial velocity** *(b)* **Numerical**

Figure 6.2: **Axial velocity UDV measurements and numerical calculation. Modeling is done by thesis advisor I. Grants using the same approach as in [12]; Values of density plot are dimensionless velocity**

Even though a stationary magnetic field brakes the fluid, they have shown that such magnetic obstacles, can, for example, aid the heat transfer by making the flow more turbulent. Such a concept could theoretically could be applied near the gas injection zone, to make the flow more turbulent and hopefully aid bubble breaking process.

6.3. Author's contribution

Due to the nature of experiments in this research area, most of them are performed in a team. The author of this thesis was taking part in and managed all of the laboratory experiments in this study. In total there were more than 30 GaInSn experiments and 5 aluminum experiments in the laboratory.

The project team manufactured the industrial prototype and organized the test in the aluminum plant. The author contributed to the design of the permanent magnet rotor through magnet field modeling, ferromagnetic yoke calculations, and stray magnetic field estimates. The author also took part in the design of the assembly process of the permanent magnet rotor which consists of 216 individual magnets which had to be done in-house due to the complexity of the problem. In industrial aluminum tests, the author was doing flow imaging and aluminum sample acquisition.

Magnetic field calculations in subsection 4.1.1 were performed by the author using the software COMSOL Multiphysics. Flow modeling was performed by Didzis Berenis within the ERDF project. The prototype of the industrial degassing unit was developed by the project team.

Dimensionless number calculations and their analysis in the scaling process are solely done by the author of the thesis.

In the aforementioned publications authorship order indicates the relative contribution of each author.

References

[1] D. E. J. Talbot, Effects of hydrogen in aluminium, magnesium, copper, and their alloys, International Metallurgical Reviews 20 (1) (1975) 166–184. doi:10.1179/imtlr.1975.20.1.166.

[2] T. Engh, G. Sigworth, A. Kvithyld, Principles of Metal Refining and Recycling, Oxford University Press, 2022.

[3] M. Leitner, T. Leitner, A. Schmon, K. Aziz, G. Pottlacher, Thermophysical Properties of Liquid Aluminum, Metallurgical and Materials Transactions A 48 (6) (2017) 3036–3045. doi:10.1007/s11661-017-4053-6.

[4] N. Müller-Fischer, P. Tobler, M. Dressler, P. Fischer, E. J. Windhab, Single bubble deformation and breakup in simple shear flow, Experiments in Fluids 45 (5) (2008) 917–926. doi:10.1007/s00348-008-0509-1.

[5] J. O. Hinze, Fundamentals of the hydrodynamic mechanism of splitting in dispersion processes, AIChE Journal 1 (3) (1955) 289–295. doi:10.1002/aic.690010303.

[6] B. O. Hasan, Experimental study on the bubble breakage in a stirred tank. part 1. mechanism and effect of operating parameters, International Journal of Multiphase Flow 97 (2017) 94 – 108. doi:10.1016/j.ijmultiphaseflow.2017.08.006.

[7] T. Wairegi, J. Grace, The behaviour of large drops in immiscible liquids, International Journal of Multiphase Flow 3 (1) (1976) 67–77. doi:10.1016/0301-9322(76)90036-7.

[8] L. Zhang, X. Lv, A. T. Torgerson, M. Long, Removal of impurity elements from molten aluminum: A review, Mineral Processing and Extractive Metallurgy Review 32 (3) (2011) 150–228. doi:10.1080/08827508.2010.483396.

[9] G. K. Sigworth, E. M. Williams, D. C. Chesonis, Gas Fluxing of Molten Aluminum: An Overview, Springer International Publishing, Cham, 2016, Ch. Furnaces, Melting, Fluxing, and Alloying, pp. 65–70. doi:10.1007/978-3-319-48228-6_9.

[10] T. Loimer, G. Machu, U. Schaflinger, Inviscid bubble formation on porous plates and sieve plates, Chemical Engineering Science 59 (4) (2004) 809–818. doi:10.1016/j.ces.2003.10.020.

[11] K. Moffatt, Electromagnetic stirring, Physics of Fluids - PHYS FLUIDS 3 (1991) 1336–1343. doi:10.1063/1.858062.

[12] I. Grants, Rotating magnetic dipole-driven flows in a conducting liquid cylinder, Physics of Fluids 33 (5) (2021) 055115. doi:10.1063/5.0047240.

[13] E. Mancilla, W. Cruz-Méndez, I. E. Garduño, C. González-Rivera, M. A. Ramírez-Argáez, G. Ascanio, Comparison of the hydrodynamic performance of rotor-injector devices in a water physical model of an aluminum degassing ladle, Chemical Engineering Research and Design 118 (2017) 158 – 169. doi:10.1016/j.cherd.2016.11.031.

[14] D. P. N. Anyalebechi, Techniques for determination of the hydrogen content in aluminium and its alloys—a review, Cast Metals 3 (4) (1990) 182–201. doi:10.1080/09534962.1990.11819039.

[15] A. Sieverts, Absorption of gases by metals, Zeitschrift für Metallkunde 21 (1929) 37–46.

[16] H. Liu, M. Bouchard, L. Zhang, An experimental study of hydrogen solubility in liquid aluminium, Journal of Materials Science 30 (17) (1995) 4309–4315. doi:10.1007/BF00361510.

[17] V. Shmelev, V. Nikolaev, J. H. Lee, C. Yim, Hydrogen production by reaction of aluminum with water, International Journal of Hydrogen Energy 41 (38) (2016) 16664 – 16673. doi:10.1016/j.ijhydene.2016.05.159.

[18] M. Birjukovs, V. Dzelme, A. Jakovics, K. Thomsen, P. Trtik, Phase boundary dynamics of bubble flow in a thick liquid metal layer under an applied magnetic field, Phys. Rev. Fluids 5 (2020) 061601. doi:10.1103/PhysRevFluids.5.061601.

[19] P. A. Davidson, An Introduction to Magnetohydrodynamics, Cambridge Texts in Applied Mathematics, Cambridge University Press, 2001. doi:10.1017/CBO9780511626333.

[20] A. Wilmot-Smith, E. Priest, G. Hornig, Magnetic diffusion and the motion of field lines, Geophys. Astrophys. Fluid Dynamics 99 (04 2005). doi:10.1080/03091920500044808.

[21] D. Berenis, R. Baranovskis, I. Grants, T. Beinerts, A. Bojarevičs, Permanent magnet bottom-stirred swirling flow in coaxial shallow cylindrical containers, Physics of Fluids 33 (5) (2021) 055127. doi:10.1063/5.0047706.

[22] J. Campbell, An overview of the effects of bifilms on the structure and properties of cast alloys, Metallurgical and Materials Transactions B 37 (6) (2006) 857–863.

[23] A. G. Szekely, Degassing molten metals, Google Patents, US Patent 3,227,547 (1966).

[24] G. Gyarmati, G. Fegyverneki, M. Tokár, T. Mende, The Effects of Rotary Degassing Treatments on the Melt Quality of an Al–Si Casting Alloy, International Journal of Metalcasting (2020). doi:10.1007/s40962-020-00428-z.

[25] J. Lazaro-Nebreda, J. B. Patel, Z. Fan, Improved degassing efficiency and mechanical properties of a356 aluminium alloy castings by high shear melt conditioning (hsmc) technology, Journal of Materials Processing Technology 294 (2021) 117146. doi:10.1016/j.jmatprotec.2021.117146.

[26] T. Yamamoto, W. Kato, S. V. Komarov, Y. Ishiwata, Investigation on the Surface Vortex Formation During Mechanical Stirring with an Axial-Flow Impeller Used in an Aluminum Process, Metallurgical and Materials Transactions B 50 (6) (2019) 2547–2556. doi:10.1007/s11663-019-01681-2.

[27] J. Walek, K. Michalek, M. Tkadlečková, M. Saternus, Modelling of technological parameters of aluminium melt refining in the ladle by blowing of inert gas through the rotating impeller, Metals 11 (2) (2021) 1–14, cited By 0. doi:10.3390/met11020284.

[28] E. Riedel, P. Köhler, M. Ahmed, B. Hellmann, I. Horn, S. Scharf, Industrial suitable and digitally recordable application of ultrasound for the enviromentally friendly degassing of aluminium melts before tilt casting, Procedia CIRP 98 (2021) 589–594, the 28th CIRP Conference on Life Cycle Engineering, March 10 – 12, 2021, Jaipur, India. doi:10.1016/j.procir.2021.01.159.

[29] J. Barbosa, H. Puga, Ultrasonic melt treatment of light alloys, International Journal of Metalcasting 13 (1) (2019) 180–189, cited By 6. doi:10.1007/s40962-018-0248-x.

[30] E. Mancilla, W. Cruz-Méndez, M. Ramírez-Argáez, C. González-Rivera, G. Ascanio, Experimental measurements of bubble size distributions in a water model and its influence on the aluminum kinetics degassing, Canadian Journal of Chemical Engineering 97 (S1) (2019) 1729–1740, cited By 3. doi:10.1002/cjce.23432.

[31] C. E. Brennen, Cavitation and bubble dynamics, Cambridge University Press, 2014.

[32] G. Eskin, Cavitation mechanism of ultrasonic melt degassing, Ultrasonics Sonochemistry 2 (2) (1995) S137 – S141. doi:10.1016/1350-4177(95)00020-7.

[33] H. Xu, Q. Han, T. T. Meek, Effects of ultrasonic vibration on degassing of aluminum alloys, Materials Science and Engineering: A 473 (1) (2008) 96 – 104. doi:10.1016/j.msea.2007.04.040.

[34] T. Leong, M. Ashokkumar, S. Kentish, The Growth of Bubbles in an Acoustic Field by Rectified Diffusion, Springer Singapore, Singapore, 2016, Ch. Fundamental Aspects, pp. 69–98. doi:10.1007/978-981-287-278-4_74.

[35] C. Tonry, V. Bojarevics, G. Djambazov, K. Pericleous, Contactless ultrasonic treatment in direct chill casting, JOM: the journal of the Minerals, Metals & Materials Society 72 (10 2020). doi:10.1007/s11837-020-04370-7.

[36] Normal-Mode and Lumped Mass Assessment of Acoustic Degassing of Liquid Metals in an Inductively Heated Cylindrical Furnace, Vol. Volume 6: Fluids and Thermal Systems; Advances for Process Industries, Parts A and B of ASME International Mechanical Engineering Congress and Exposition. doi:10.1115/IMECE2011-65531.

[37] J. M. Zeng, Z. B. Xu, J. He, New process of elimination of hydrogen from melt aluminum, in: Engineering Materials III, Vol. 51 of Advanced Materials Research, Trans Tech Publications Ltd, 2008, pp. 93–98. doi:10.4028/www.scientific.net/AMR.51.93.

[38] H. Xu, X. Jian, T. Meek, Q. Han, Ultrasonic Degassing of Molten Aluminum under Reduced Pressure, John Wiley and Sons, Ltd, 2013, Ch. Melt Quality: Degassing, Filtering, and Analysis, pp. 246–250. doi:10.1002/9781118647783.ch30.

[39] K. Strauss, Chapter 7 - the treatment of aluminium and aluminium alloys, in: K. Strauss (Ed.), Applied Science in the Casting of Metals, Pergamon, 1970, pp. 268 – 270. doi:10.1016/B978-0-08-015711-5.50018-X.

[40] T. Haas, C. Schubert, M. Eickhoff, H. Pfeifer, A review of bubble dynamics in liquid metals, Metals 11 (4) (2021). doi:10.3390/met11040664.

[41] W. Zhao, H. Wang, R. Bai, W. Wei, H. Wang, Bubble characteristics and turbulent dissipation rate in horizontal bubbly pipe flow, AIP Advances 11 (2) (2021) 025125. doi:10.1063/5.0035816.

[42] G. Kocamustafaogullari, W. Huang, J. Razi, Measurement and modeling of average void fraction, bubble size and interfacial area, Nuclear Engineering and Design 148 (2) (1994) 437–453. doi:10.1016/0029-5493(94)90124-4.

[43] S. Arias, R. González-Cinca, X. Ruiz, L. Ramírez-Piscina, J. Casademunt, Characterization of the performance of an injector for the controlled generation of microbubbles, 59th International Astronautical Congress 2008 proceedings (09 2008).

[44] E. Mohseni, J. Jose Kalayathine, S. F. Reinecke, U. Hampel, Dynamics of bubble formation at micro-orifices under constant gas flow conditions, International Journal of Multiphase Flow 132 (2020) 103407. doi:10.1016/j.ijmultiphaseflow.2020.103407.

[45] H. Mirsandi, W. Smit, G. Kong, M. Baltussen, E. Peters, J. Kuipers, Bubble formation from an orifice in liquid cross-flow, Chemical Engineering Journal 386 (2020) 120902. doi:10.1016/j.cej.2019.01.181.

[46] C. Veldhuis, A. Biesheuvel, L. van Wijngaarden, Shape oscillations on bubbles rising in clean and in tap water, Physics of Fluids 20 (4) (2008) 040705. doi:10.1063/1.2911042.

[47] A. Prosperetti, Bubbles, Physics of Fluids 16 (6) (2004) 1852–1865. doi:10.1063/1.1695308.

[48] G. Besagni, F. Inzoli, T. Ziegenhein, Two-phase bubble columns: A comprehensive review, ChemEngineering 2 (2) (2018). doi:10.3390/chemengineering2020013.

[49] N. Kantarci, F. Borak, K. O. Ulgen, Bubble column reactors, Process Biochemistry 40 (7) (2005) 2263–2283. doi:10.1016/j.procbio.2004.10.004.

[50] O. Keplinger, N. Shevchenko, S. Eckert, Validation of x-ray radiography for characterization of gas bubbles in liquid metals, IOP Conference Series: Materials Science and Engineering 228 (2017) 012009. doi:10.1088/1757-899X/228/1/012009.

[51] R. Baranovskis, M. Sarma, M. Ščepanskis, T. Beinerts, A. Gaile, S. Eckert, D. Raebiger, E. Lehmann, K. Thomsen, P. Trtik, Investigation of particle dynamics and solidification in a two-phase system by neutron radiography, Magnetohydrodynamics 56 (2020) 43–50. doi:10.22364/mhd.56.1.4.

[52] T. Wondrak, K. Timmel, C. Bruch, P. Gardin, G. Hackl, H. Lachmund, H. Lüngen, H.-J. Odenthal, S. Eckert, Large-scale test facility for modeling bubble behavior and liquid metal two-phase flows in a steel ladle, Metallurgical and Materials Transactions B (03 2022). doi:10.1007/s11663-022-02481-x.

[53] P. Davidson, Magnetohydrodynamics in material processing, Annual Review of Fluid Mechanics 31 (2003) 273–300. doi:10.1146/annurev.fluid.31.1.273.

[54] J. Zeng, W. Chen, Y. Yang, A. Mclean, A Review of Permanent Magnet Stirring During Metal Solidification, Metallurgical and Materials Transactions B 48 (6) (2017) 3083–3100. doi:10.1007/s11663-017-1077-7.

[55] P. Davidson, High pressure and high flowrate induction pumps with per-manent magnets, I. Bucenieks 39 (2003) 411–417.

[56] T. Beinerts, A. Bojarevičs, R. Baranovskis, M. Milgrāvis, I. Kaldre, Permanent magnet dipole stirrer for aluminium furnaces, IOP Conference Series: Materials Science and Engineering 424 (2018) 012037. doi:10.1088/1757-899x/424/1/012037.

[57] A. Bojarevičs, T. Beinerts, M. Sarma, Y. Gelfgat, Arrays of rotating permanent magnet dipoles for stirring and pumping of liquid metals, Journal for Manufacturing Science and Production 15 (1) (2015) 35–39. doi:doi:10.1515/jmsp-2014-0039.

[58] J. Priede, G. Gerbeth, Oscillatory instability of electromagnetically levitated solid bodies, IEEE Transactions on Magnetics 36 (1) (2000) 354–357. doi:10.1109/20.822546.

[59] R. Chen, Y. Yang, Q. Wang, H. Ding, Y. Su, J. Guo, Dimensionless parameters controlling fluid flow in electromagnetic cold crucible, Journal of Materials Processing Technology 255 (2018) 242–251. doi:https://doi.org/10.1016/j.jmatprotec.2017.12.020.

[60] I. Nikulin, A. Perminov, Mathematical modelling of frequency and force impacts on averaged metal flows in alternating magnetic field, International Journal of Heat and Mass Transfer 128 (2019) 1026–1032. doi:https://doi.org/10.1016/j.ijheatmasstransfer.2018.08.130.

[61] S. Cheng, Z. Wu, Microfluidic electronics, Lab on a chip 12 (2012) 2782–91. doi:10.1039/c2lc21176a.

[62] A. Dinsdale, P. Quested, The viscosity of aluminium and its alloys—a review of data and models: Special section: Proceedings of the 2003 international symposium on liquid metals (guest editors: P. d. lee, a. mitchell, a. jardy, j.-p. bellot), Journal of Materials Science 39 (12 2004). doi:10.1023/B:JMSC.0000048735.50256.96.

[63] R. Brandt, G. Neuer, Electrical resistivity and thermal conductivity of pure aluminum and aluminum alloys up to and above the melting temperature, International Journal of Thermophysics 28 (2007) 1429–1446. doi:10.1007/s10765-006-0144-0.

[64] S. Eckert, A. Cramer, G. Gerbeth, S. Molokov, R. Moreau, K. Moffatt, Velocity Measurement Techniques for Liquid Metal Flows, Springer, 2007, Ch. 17, pp. 275–294. doi:10.1007/978-1-4020-4833-3_17.

[65] C. T. Rueden, J. E. Schindelin, M. C. Hiner, B. E. DeZonia, A. E. Walter, E. T. Arena, K. W. Eliceiri, Imagej2: Imagej for the next generation of scientific image data, BMC Bioinformatics 18 (2017).

[66] D. Abreu-López, A. Amaro-Villeda, F. Acosta-González, C. Gonzalez-Rivera, M. Ramírez-Argáez, Effect of the impeller design on degasification kinetics using the impeller injector technique assisted by mathematical modeling, Metals 7 (04 2017). doi:10.3390/met7040132.

[67] G. Chen, S. He, Numerical simulation of argon–molten steel two-phase flow in an industrial single snorkel refining furnace with bubble expansion, coalescence, and breakup, Journal of Materials Research and Technology 9 (3) (2020) 3318–3329. doi:10.1016/j.jmrt.2020.01.026.

[68] X. Cui, Y. Xue, D. Zhao, S. Wang, F. Guo, Physical modeling of bubble behaviors in molten steel under high pressure, High Temperature Materials and Processes 40 (1) (2021) 471–484. doi:doi:10.1515/htmp-2021-0045.

[69] V.-V. Visuri, T. Vuolio, T. Haas, T. Fabritius, A review of modeling hot metal desulfurization, Steel Research International 91 (2020) 1900454. doi:10.1002/srin.201900454.

[70] S. Schneider, S. Bajohr, F. Graf, T. Kolb, State of the art of hydrogen production via pyrolysis of natural gas, ChemBioEng Reviews 7 (5) (2020) 150–158. doi:10.1002/cben.202000014.

[71] B. J. Leal Pérez, J. A. Medrano Jiménez, R. Bhardwaj, E. Goetheer, M. van Sint Annaland, F. Gallucci, Methane pyrolysis in a molten gallium bubble column reactor for sustainable hydrogen production: Proof of concept and techno-economic assessment, International Journal of Hydrogen Energy 46 (7) (2021) 4917–4935. doi:10.1016/j.ijhydene.2020.11.079.

[72] K. Stewartson, On the flow between two rotating coaxial disks, Mathematical Proceedings of the Cambridge Philosophical Society 49 (2) (1953) 333–341. doi:10.1017/S0305004100028437.

[73] R. Monchaux, M. Berhanu, S. Aumaître, A. Chiffaudel, F. Daviaud, B. Dubrulle, F. Ravelet, S. Fauve, N. Mordant, F. Pétrélis, M. Bourgoin, P. Odier, J.-F. Pinton, N. Plihon, R. Volk, The von kármán sodium experiment: Turbulent dynamical dynamos, Physics of Fluids 21 (3) (2009) 035108. doi:10.1063/1.3085724.

[74] J. Román, A. Figueroa, S. Cuevas, Wake patterns behind a magnetic obstacle in an electrolyte layer, Magnetohydrodynamics 53 (2017) 55–66. doi:10.22364/mhd.53.1.7.

[75] J. Román, K. Uriostegui, W. Guerrero, A. Figueroa, S. Cuevas, Electromagnetically generated vortex streets in a narrow channel, International Journal of Heat and Fluid Flow 84 (2020) 108597. doi:https://doi.org/10.1016/j.ijheatfluidflow.2020.108597.

ACKNOWLEDGMENTS

This work was financially supported by the ERDF project “Electromagnetic technology for aluminum degassing process” with No. 1.1.1.1/18/A/149 and by the University of Latvia Foundation stipend for Ph.D. students in natural sciences. In the final year the work was also backed by the project ”Strengthening of the capacity of doctoral studies at the University of Latvia within the framework of the new doctoral model”, identification No. 8.2.2.0/20/I/006.

I am thankful to my colleagues who directly or indirectly were involved in my endeavors. Firstly, my thesis supervisor Dr. Ilmars Grants who provided excellent help regarding the theoretical aspects of the work. The discussion about physics assisted tremendously with understanding the nuances of the physical processes taking place and helped me structure the thesis. Didzis Berenis developed a multi-physics numerical model of the experimental system used in this work. All of the numerical calculations involving fluid dynamics were performed by him and allowed him to gain insights into things that could not be measured in the system. Experimentally I was helped with video capture by Matīss Kalvānas which was crucial in imaging the surface of GaInSn and aluminum. Mikus Milgrāvis assisted experimentally contributing to many of the 30+ experiments carried out. Dr. Toms Beinerts organized collaboration between laboratory and aluminum industry partners. NTNU’s professor Robert Fritzsch consulted me on aluminum degassing from the industry’s point of view Lastly, I am glad to be helped by my life partner Antra Gaile. She not only supported me emotionally but also dealt with the hardest of LaTeX problems.

NATIONAL
DEVELOPMENT
PLAN 2020

EUROPEAN UNION
European Social
Fund

INVESTING IN YOUR FUTURE

ATTACHMENTS

Derivation of magnitude of electromagnetic forces in metal. we start with Faraday's induction law (6.1)

$$\nabla \times \vec{E} = \frac{\partial \vec{B}}{\partial t} \tag{6.1}$$

Current density is proportional to electric field (6.2)

$$\vec{E} = \frac{\vec{j}}{\sigma} \tag{6.2}$$

Let's introduce harmonic changing magnetic field (6.3)

$$\vec{B} = B_0 Sin(\omega t) \tag{6.3}$$

Time derivative of harmonic magnetic field is following (6.4)

$$\frac{\partial \vec{B}}{\partial t} = \omega B_0 Cos(\omega t) \tag{6.4}$$

Rotor on left side of (6.1) in dimension analysis is simplified to (6.5)

$$\frac{1}{L} \cdot \frac{\vec{j}}{\sigma} = \omega B_0 Cos(\omega t) \tag{6.5}$$

So result current density is (6.6)

$$\bar{j} = \omega \bar{B} L \sigma \tag{6.6}$$

Knowing applied magnetic field and induced current density we can obtain magnitude of time averaged force (6.7)

$$\bar{f}_{EM} = \vec{j} \times \vec{B} \approx \bar{j} \cdot \bar{B} = \sigma\omega \frac{B_0}{\sqrt{2}} L \cdot \frac{B_0}{\sqrt{2}} = \frac{1}{2} \sigma \omega B_0^2 L \cdot \tag{6.7}$$

The ratio for electromagnetic force to surface tension forces does not have a well known dimensionless number. It can be expressed by other dimensionless numbers in a following way (6.8), however, this expression is unnecessarily complicated for describing the system.

$$N_{EMtoLaplace} = \frac{EM}{intertial} \cdot \frac{buoyancy}{tension} \cdot \frac{inertial}{buoyancy} = N_{Stuart} \cdot Eo \cdot Fr^2 \tag{6.8}$$

Principle and limitation of operation of pulsed Ultrasound Doppler velocimetry (UDV) is explained here. Firstly, it is important to highlight the difference between pulsed and regular Doppler ultrasound. The Doppler effect is the change in frequency of an acoustic or electromagnetic wave resulting from a movement of the emitter or receiver relative to each other. The term "Doppler ultrasound velocimetry" implies that the velocity is measured by finding the change of frequency in the received signal, as it is in the case of Laser Doppler velocimetry. In fact, in ultrasonic pulsed Doppler velocimetry, this is never the case since velocities are derived from shifts in positions between pulses, and the Doppler effect plays a minor role. Quoting manufacturer SIGNAL PROCESSING SA: "Many publications, even recent ones, fail to make this distinction, resulting in an erroneous system description and a fallacious interpretation of the influence from various physical effects."

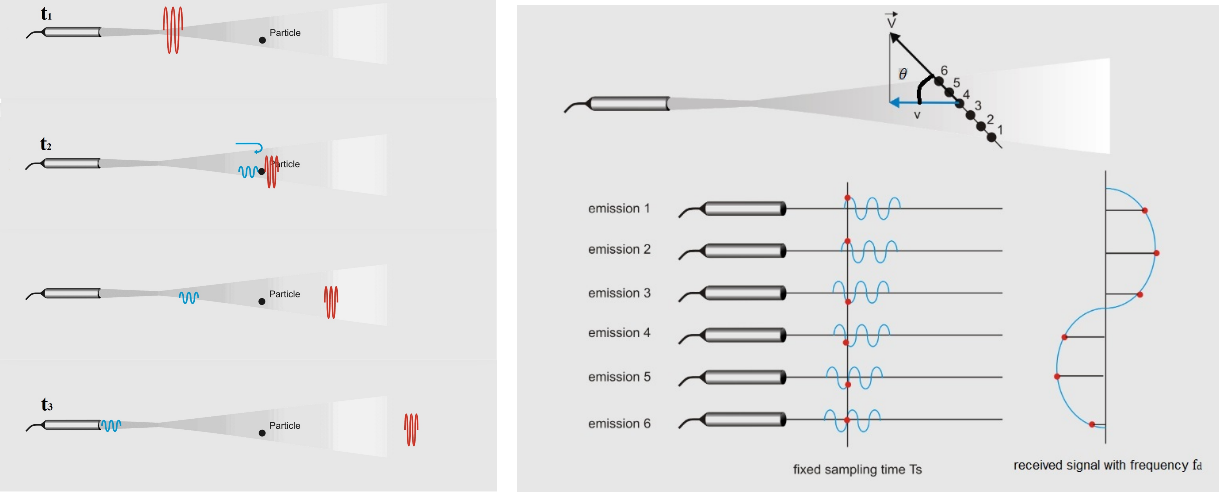

(a) **Probe emitting a single pulse which is reflected of a particle and measured by the transducer in the same probe**

(b) **Reflected signal of a moving particle forms a sinusoidal wave with a new frequency f_D**

Figure 6.3: **Principle of UDV**

In pulsed Doppler ultrasound, instead of emitting continuous ultrasonic waves, an emitter periodically sends a short ultrasonic burst and a receiver continuously collects echoes issued from targets that may be present in the path of the ultrasonic beam (see Fig. 6.3a). By sampling the incoming echoes at the same time relative to the emission of the bursts, the velocity of the particles can be computed. If we assume thet_1 is the time of the emitted burst, t_2 is time of scattering and t_3 is time when echo reaches transducer, and c is sound velocity of acoustic wave, the depth of particle is given with Eq. (6.9):

$$x_{depth} = \frac{c}{2(t_3 - t_1)} \tag{6.9}$$

As stated, in pulsed ultrasonic velocimetry bursts are emitted periodically. Following each emission, the echo signal is sampled at a fixed delay after the emission. If the particle moves between the successive emissions, the sampled values taken at time t_s will change over time. Depending on the shape of the emitted signal, these values may form a sinusoidal signal as shown in Fig. 6.3. The frequency of the received signal is called Doppler frequency and it is a function of the particle's velocity. This is described by the Doppler equation Eq. (6.10):

$$f_D = \frac{2 f_e v \cos\theta}{c} \tag{6.10}$$

where f_e frequency of the emitted burst, f_D is the frequency of received sinusoidal signal and $\cos\theta$ is the angle between transducer and velocity vector. From Eq. (6.10) we can calculate particle flow velocity as in Eq. (6.11):

$$v = \frac{f_D \cdot c}{2 f_e \cos\theta} \tag{6.11}$$

In the real world, there are many particles, and these particles are randomly distributed inside the ultrasonic beam. The echoes issued from each particle are therefore combined together in a random fashion, and give a random echo signal. Hopefully, a high degree of correlation exists between the different emissions. The algorithms to extract the velocity information are based on this correlation.

Pulsed Doppler ultrasound instantaneously offers a complete velocity profile. Unfortunately, as the information is available only periodically, this technique suffers from the Nyquist theorem, meaning that a maximum velocity (6.12) and the maximum measurable depth (6.13) exists for each pulse repetition frequency f_{prf}:

$$v_{max} = \frac{f_{prf} \cdot c}{4 f_e \cos\theta} \tag{6.12}$$

$$x_{max} = \frac{c}{2 f_{prf}} \tag{6.13}$$

Since v_{max} is proportional to f_{pfr} but x_{max} is inversely proportional to it, the pulse repetition frequency f_{prf} has to be carefully chosen in the experiment to balance how deep and how large velocities can be measured.

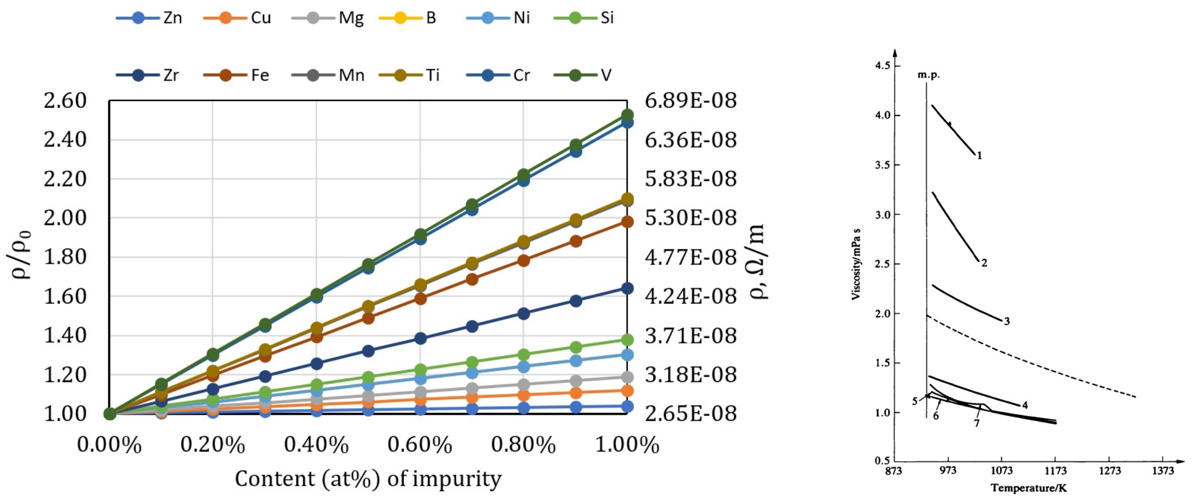

(a) **Resistivity**

(b) **Viscosity [62]**

Figure 6.4: **Aluminum property changes with adding alloying elements.Reference value is pure aluminum. Resistivity change for small concentrations is visualized from [2]**

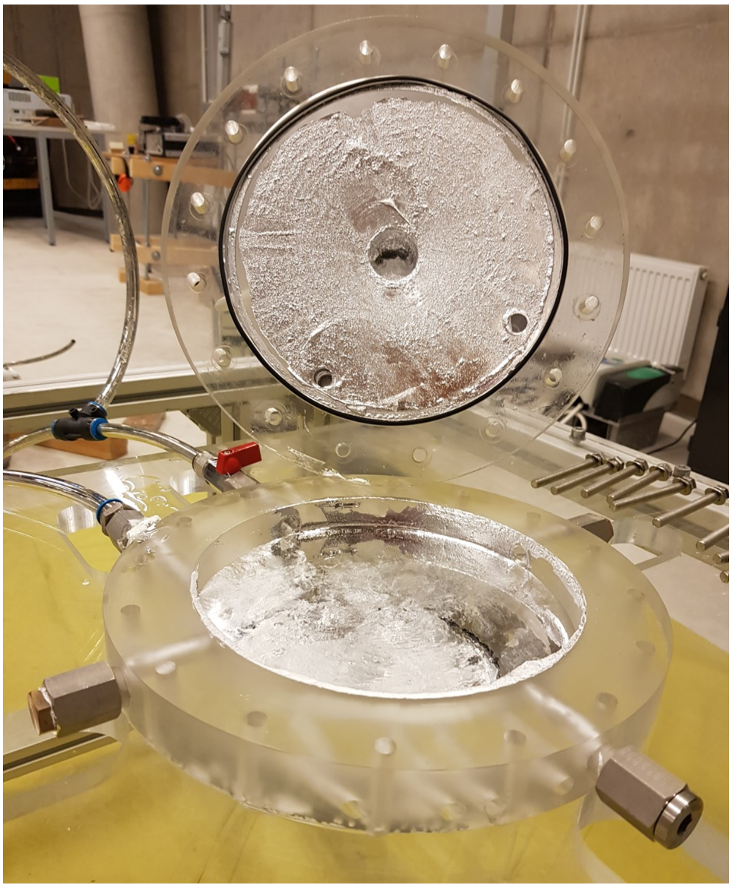

Figure 6.5: **Dismantled cylindrical GaInSn vessel shows oxide layer formed on all walls**

Figure 6.6: **Example of tracking individual bubble for speed and residence time measurements shown in Fig. 5.19; Applied magnetic field frequency is 19.2 Hz which produced average measured bubble velocity of 2.4 m/s**

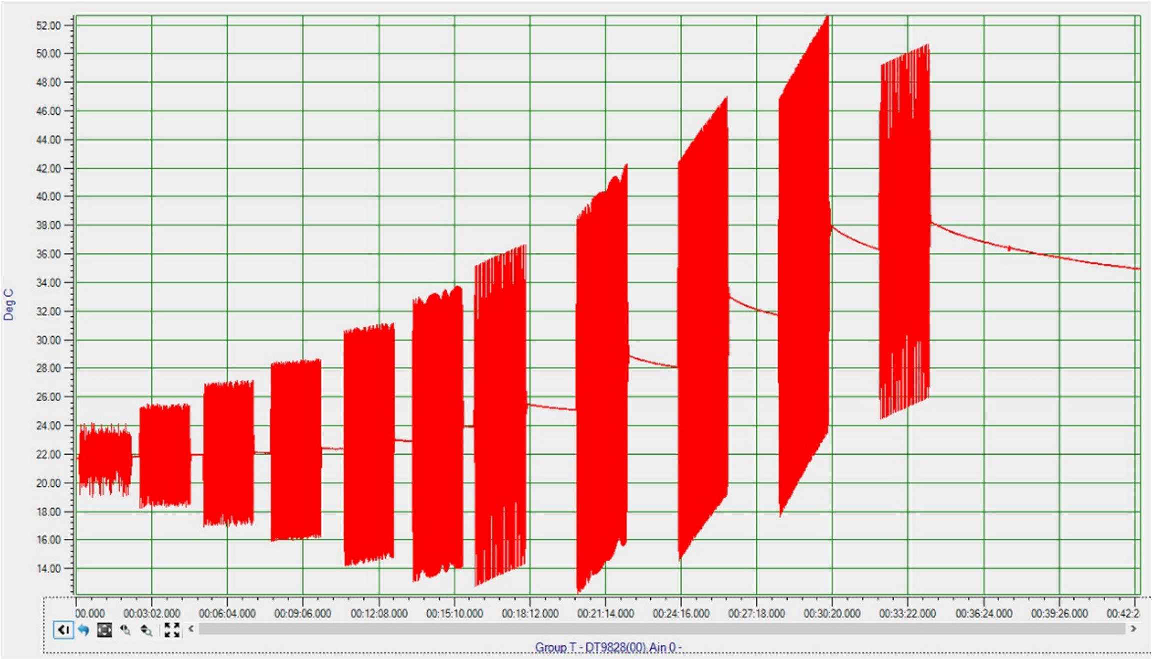

Figure 6.7: **Temperature measurements to calculate power dissipation in metal; Each time magnet rotation is switched on noise is affecting thermocouple readings proportional to applied rotational frequency**

様式−050302改1

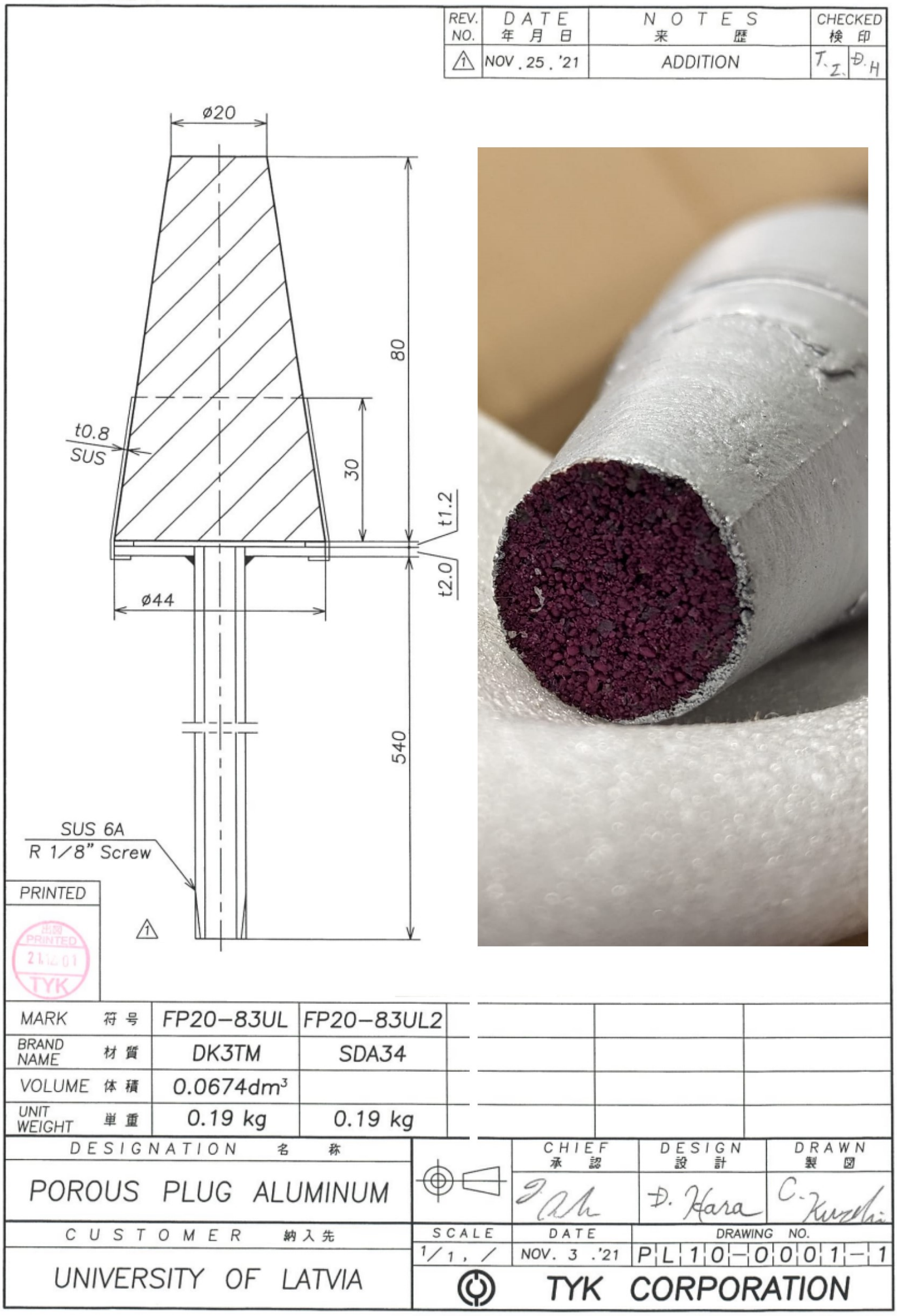

REV. NO.	DATE 年 月 日	NOTES 来 歴	CHECKED 検 印
△	NOV.25.'21	ADDITION	T.I. D.H

PRINTED

出図 PRINTED 21.12.01 TYK

MARK 符号	FP20−83UL	FP20−83UL2
BRAND NAME 材質	DK3TM	SDA34
VOLUME 体積	0.0674dm³	
UNIT WEIGHT 単重	0.19 kg	0.19 kg

DESIGNATION 名称

POROUS PLUG ALUMINUM

CUSTOMER 納入先

UNIVERSITY OF LATVIA

CHIEF 承認	DESIGN 設計	DRAWN 製図
	D. Hara	C.

SCALE	DATE	DRAWING NO.
1/1	NOV. 3 .'21	PL10−0001−1

TYK CORPORATION

Figure 6.8: **Technical drawing of a porous plug and a picture of end of the plug which will be exposed to aluminum; This plug has a flow rate of around** $5 - 10L/min$ **at** $0.1MPa$**. Composition:** $Al_2O_3 - 91.1\%$; $Cr_2O_3 - 1.7\%$; $SiO_2 - 6.7\%$ **and** $ZrO_2 - 3.0\%$, **apparent porosity - 23.8 %**